UNIVERSIDADE DE LISBOA
FACULDADE DE CIÊNCIAS
DEPARTAMENTO DE FÍSICA

Assessment of lesion-induced network connectivity disruption in the human brain: application to a context of pre-surgical planning

Laëticia Henriques

Mestrado Integrado em Engenharia Biomédica e Biofísica
Perfil em Engenharia Clínica e Instrumentação Médica

Dissertação orientada por:
Alexandre Andrade

2020

Acknowledgments

First of all, I would like to thank the Institute of Biophysics and Biomedical Engineering (IBEB), where this dissertation was conducted, for all the support provided during this time.

I would also like to thank my supervisor, Alexandre Andrade, for his guidance, support and availability during the development of this study. I am very thankful for the opportunity of working in his project.

Furthermore, I would like to thank Dr. Martin Lauterbach and Diogo Duarte for their availability and contribution for this study.

I want to express my gratitude for all the collaborators of IBEB for their attentiveness, mainly to my colleagues Silvestre Piedade and Catarina Pelicano for supporting my work and dedicating their time in helping this project to be a success.

To my colleagues Ana Sofia Verde and Neusa Martins who walked with me in this academic journey side by side.

To my hometown friends that are supporting me since I remember. Thank you for understanding my absences in important dates. A special thank to Maria Cruz, Maria Gomes, Sofia Teles and Ana Carvalho for never stop believing in me.

Finally and most important, I want to express my deepest gratitude to my parents and my sister. They are my biggest support. They know how hard I worked for this dissertation, neglecting my family time. I could not done this without you.

Abstract

Neurosurgery has been considered as a treatment or a therapy option for brain lesions with satisfactory outcomes regarding the maximal resection of the lesioned area and the minimal post-surgical neurological dysfunctions by avoiding eloquent areas. For the last two decades, resting-state functional magnetic resonance imaging (rs-fMRI) has emerged as an effective non-invasive neuro-imaging technique that can be used for pre-surgical functional brain mapping at rest. The analysis of these maps can focus on both the local function of specific regions (segregation) and the functional connections between them (integration) for the assessment of lesion-induced changes. The brain network can be characterized resorting to graph theory analysis for the calculation of these segregation and integration properties which is more facilitated on thresholded binarized matrices. These can be obtained by proportional thresholds revealing the top strongest connections that are present in the network.

This study intends to analyse and compare the segregation and integration properties of lesioned and non lesioned hemispheric networks from a group of 7 patients with brain tumors and a cavernous malformation. Moreover, it also aims to evaluate the effect of the proportional thresholds in those properties. By using rs-fMRI and graph theory analysis, the network features of lesioned and non lesioned hemispheres were investigated, over a range between 20%-40% (at intervals of 5%) of proportional thresholds.

The results reflected more integrated and segregated networks as more connections were included in the networks. The lesioned network revealed higher global integration and local processing at the highest density of 40%. However, the lesioned small-world organization was less optimal when comparing to the non lesioned network.

In conclusion, our findings indicated that the lesion-induced perturbations disturbed the functional connectivity of the lesioned hemisphere. Nevertheless, compensatory mechanisms should be accounted for the pre-surgical evaluation of the affected and unaffected brain areas.

Keywords: resting-state functional magnetic resonance imaging; tumor; graph theory; proportional threshold; between-hemispheres network analysis.

Resumo

A remoção cirúrgica de uma lesão cerebral envolve a resseção da maior área lesada sem comprometer o tecido eloquente e não lesado envolvente. Desta forma, pretende-se minimizar disfunções neurológicas após a cirurgia garantindo a melhor qualidade de vida possível. Como tal, há a necessidade de incluir técnicas de imagem auxiliares à cirurgia que permitam fazer um mapeamento da lesão cerebral, não só ao nível anatómico mas principalmente funcional.

Atualmente, existem diversas técnicas de neuro-imagem que atuam de forma não invasiva e que contribuem para o mapeamento funcional do cérebro, num contexto pré-cirúrgico. Destas destaca-se a imagem de ressonância magnética funcional que, tradicionalmente requer que o sujeito execute uma tarefa de modo a extrair as redes neuronais associadas às regiões ativadas pelo desempenho da tarefa. No entanto, o facto desta técnica apenas possibilitar a extração de redes neuronais singulares somente associadas à tarefa em questão bem como sujeitos com lesões poderem ter dificuldades em realizar a tarefa requerida levou a que nas últimas duas décadas tenha emergido uma nova modalidade - a imagem de ressonância magnética funcional de repouso. Esta distingue-se da anterior no sentido do sujeito não executar qualquer tarefa nem ser submetido a qualquer estímulo. Através da aquisição da atividade cerebral espontânea é possível extrair as redes neuronais relacionadas com a atividade neuronal. Desta forma, a imagem de ressonância magnética funcional de repouso não só supera a limitação da eventual dificuldade ou incapacidade de execução de uma tarefa como também faculta a identificação de múltiplas redes neuronais, ao contrário da ressonância funcional baseada numa tarefa requerida.

A extração destas redes neuronais funcionais é conseguida mediante a aplicação de métodos de análise que se focam na localização da função de determinadas regiões cerebrais (segregação) ou na conectividade funcional entre as mesmas (integração). Complementarmente, métodos que englobam tanto a análise da atividade (segregação) como da conectividade (integração) da imagem da ressonância magnética funcional de repouso têm sido combinados com a teoria dos grafos com o objetivo de investigar o cérebro enquanto uma rede neuronal complexa com conexões contínuas e dispersas entre as suas regiões. Ao mesmo tempo também permitem determinar as propriedades da organização funcional cerebral tanto a nível global como local, isto é, em grupos de regiões interligados igualmente denominados de módulos ou comunidades.

Para caracterizar a integração e segregação da rede neuronal diversas medidas topológicas associadas à capacidade da rede neuronal partilhar informação entre diferentes regiões podem ser calculadas. O cálculo destas medidas implica a construção da rede neuronal funcional enquanto um conectoma definido por um dado número de regiões cerebrais, designadas de nodos, e pelas conexões funcionais estabelecidas entre as mesmas. O nível de conectividade funcional entre os nodos, também denominado de correlação funcional, é determinado pela computação da correlação entre as séries temporais de cada par de nodos. Posteriormente, estes dados podem ser organizados numa matriz de conectividade cujas entradas representam os pesos da correlação funcional.

Contudo, o elevado número de conexões entre as regiões cerebrais dificulta a extração de informação

relevante. Neste sentido, a binarização e aplicação de um limiar à matriz de conectividade assegura a redução dessas interações facilitando a determinação das propriedades topológicas da rede neuronal. Limiares que consideram um coeficiente de correlação funcional entre as regiões como o valor limiar para a inclusão das conexões (limiar absoluto) podem ser impostos à matriz. Por outro lado, ao invés de um limite de correlação, também se pode selecionar uma percentagem das conexões mais fortes a serem incluídas na rede (limiar proporcional ou densidade). Estudos anteriores mostram evidências que limitar as redes neuronais por via de um limite de densidade resulta em medidas topológicas mais estáveis, razão pelo qual os limites proporcionais têm sido mais frequentemente aplicados na sua computação. Ainda assim, não existe um consenso relativamente à escolha ideal do valor do limiar que evita resultados incompletos ou falaciosos.

O objetivo deste estudo engloba a análise de redes neuronais relativas aos hemisférios lesados e não lesados para um grupo de sete sujeitos com tumores cerebrais e uma malformação cavernosa. Adicionalmente, para cada hemisfério será calculado um conjunto de medidas de segregação e integração que permite caracterizar a respetiva rede neuronal, seguido de uma comparação entre as mesmas. Estas medidas serão determinadas com base na teoria de grafos aplicação de um conjunto de limiares proporcionais à matriz binarizada, com fundamento nos benefícios explorados acima. Deste modo, em cada rede neuronal, as conexões funcionais entre as suas regiões serão limitadas por um leque de densidades que varia entre 20% e 40%, com intervalos de 5%. Assim, a comparação entre as propriedades hemisféricas será realizada para cada limiar. Além do mais, uma comparação das medidas de grafos entre os diferentes limiares também será conduzida de modo a estudar o efeito dos mesmos na topologia de cada rede neuronal.

Em primeiro lugar, os resultados deste estudo demonstraram que tanto o hemisfério lesado como o hemisfério não lesado estão organizados segundo uma rede de pequeno mundo, equilibrando de forma eficaz o processamento local e a integração global. Contudo, o hemisfério lesado mostrou ter uma organização topológica sub-ótima em comparação com o hemisfério não lesado.

Os resultados da análise das medidas de integração revelaram que a inclusão de mais conexões nas redes lesadas e não lesadas, através do aumento do limiar proporcional, levou a uma diminuição da distância mínima entre duas regiões, sendo essa diminuição maior no hemisfério não lesado. Complementarmente, a eficiência global associada à comunicação entre as regiões também aumentou com a inclusão de mais conexões nos hemisférios. Desta forma pôde concluir-se que a consideração de mais conexões funcionais nas redes neuronais permitiu comunicações intra hemisféricas mais curtas e consequentemente mais eficientes, numa perspetiva global para as redes neuronais. Para além disso, o hemisfério não lesado revelou uma maior integração global para todas as densidades, exceto para a densidade de 40%. Para esta densidade, a reorganização funcional da rede neuronal lesada mostrou ser mais construtiva permitindo uma eficiência global mais elevada.

Ao nível da segregação, os resultados evidenciaram que a escolha de densidades mais elevadas levou a que as redes neuronais fossem mais segregadas. Excluindo as densidades mais elevadas, o nível de conexões locais na rede lesada bem como a sua eficiência de propagação informação local foi menor em comparação com a rede não lesada. Para a densidade de 40%, a transferência de informação local foi mais eficiente no hemisfério lesado. Assim, o hemisfério lesado revelou não só uma maior integração global como também uma especialização local mais eficiente.

Em conclusão, as medidas topológicas calculadas pareceram depender da escolha do limiar proporcional que foi aplicado nas redes neuronais. Para as densidades entre 20%-35%, os resultados mostraram que a lesão localizada no hemisfério lesado conduziu a disrupções na estrutura funcional desse mesmo hemisfério (menor integração e segregação). Porém, na densidade de 40%, a reorganização funcional

pareceu indicar o estabelecimento de mecanismos e conexões compensatórios suficientes para compensar as perturbações causadas pela presença da lesão nesse hemisfério.

De notar que os resultados não mostraram ser totalmente conclusivos quanto ao impacto da lesão na rede não lesada, através de interações funcionais entre os hemisférios.

Assim, os resultados deste estudo sugeriram que as perturbações funcionais induzidas pela lesão afetaram a conectividade funcional entre as regiões do hemisfério onde a mesma estava localizada. Como consequência, a escolha de densidades mais elevadas pareceu clarificar conexões e mecanismos de compensação no hemisfério lesado. Deste modo, estas alterações devem ser tidas em conta para a avaliação pré-cirúrgica das áreas cerebrais afetadas e não afetadas.

Palavras-chave: imagem de ressonância magnética funcional de repouso; tumor; teoria dos grafos; limiares proporcionais; análise entre hemisférios das redes neuronais.

Contents

List of Figures

List of Tables

Acronyms

AAL automated anatomically labeled.

AIS acute ischemic stroke.

ALFF Amplitude of Low Frequency Fluctuations.

ANOVA Analysis of Variance.

BOLD blood oxygenation level dependent.

BRAPH BRain Analysis using graPH theory.

CNS central nervous system.

CSF cerebrospinal fluid.

DCS Direct cortical stimulation.

DICOM Digital Imaging and Communications in Medicine.

DMN default mode network.

DNA deoxyribonucleic acid.

DPABI Data Processing and Analysis for Brain Imaging.

DPARSF Data Processing Assistant for Resting-State fMRI.

EEG electroencephalography.

EPI echo-planar imaging.

ESI Electric source imaging.

FDR false discovery rate.

fMRI functional magnetic resonance Imaging.

FWHM full width at a half maximum.

GM grey matter.

GRETNA GRaph thEoretical Network Analysis.

GUI graphical user interface.

GUIs graphical user interfaces.

HCs healthy controls.

IBEB Institute of Biophysics and Biomedical Engineering.

ICA independent component analysis.

ICs independent components.

LGG low-grade glioma.

MEG magnetoencephalography.

MNET Multimodal brain NETwork Toolbox.

MNI Montreal Neurological Institute.

MRI magnetic resonance imaging.

NIfTI neuro-imaging Informatics Technology Initiative.

PET positron emission tomography.

ReHo Regional Homogeneity.

RF radio frequency.

ROI region of interest.

ROIs regions of interest.

rs-fMRI resting-state fMRI.

SNR signal-to-noise ratio.

SPM Statistical Parametric Mapping.

tb-fMRI task-based fMRI.

TE echo time.

TR repetition time.

US United States.

WM white matter.

WMLs white matter lesions.

WMLs-VaD white matter lesions with vascular dementia.

WMLs-VCIND white matter lesions with non-dementia vascular cognitive impairment.

Chapter 1

Introduction

Brain and other central nervous system (CNS) tumors are associated with a high incidence rate. Indeed, in the United States (US), between 2012 and 2016, more than 400 000 tumor cases involved the brain and other CNS tumors. Of these, 30.2% and 69.8% were respectively of malignance and non-malignance natures. Furthermore, in Europe and only in 2018, around 64 600 cases of malignant tumors were from brain or other CNS regions [1].

Besides tumors, other lesions can be found in the brain tissue, such as vascular malformations. Those consist in congenital lesions related to primitive vascular elements (arterial, capillary, lymphatic or venous) that were incompletely resorbed in an early stage of fetal development. When respecting congenital capillary or venules lesions, the vascular malformations can also be referred as cavernomas or cavernous malformations [2]. Though uncommon, they are the most common cerebral vascular abnormality and account for 10% to 25% of all vascular malformations [3].

Neurosurgery has evolved as a safe technique with the maximal lesion resection improving symptom management, quality of life and overall survival in the mentioned pathologies. Nevertheless, surgical procedures on patients suffering from brain lesions face two main challenges: removing the lesioned area, while respecting neurological function. In this context, the integration of pre-operative and intra-operative brain mapping is an important advance in neurosurgery allowing for the treatment of brain tumors while preserving eloquent areas and minimizing post-operative deficits.

During the last decades, the development of non-invasive neuro-imaging techniques as electric source imaging (ESI), using electroencephalography (EEG), positron emission tomography (PET), magnetoencephalography (MEG) and functional magnetic resonance imaging (fMRI) has improved the brain mapping in a pre-surgical planning, without compromising the patient [4]. In principle, fMRI measurements can be accomplished resorting to different techniques; being the BOLD-fMRI the most frequently used in human brain. Therefore, it enables the identification of the brain functional areas through the detection of local hemodynamic changes in synchrony with the required and performed task. However, task-based fMRI can fail in patients who cannot perform the tasks satisfactorily because of neurological deficits or neurocognitive state. In such cases, an alternative relies on the detection of brain spontaneous activity (< 0.1 Hz) which appears to correspond to specific brain circuits involved in motor control, vision and cognitive integration [5].

From resting-state fMRI data, information involving the activity of functional activated brain regions and the connectivity between them can be extracted through, respectively, segregation and integration techniques [6]. A network model of the brain should incorporate both segregation and integration measures. Therefore, the brain function is described as a consequence of the information exchange between its components. Resorting to graph theory, the brain network is defined as a collection of nodes, rep-

resenting the brain regions, and the connections between pairs of nodes. Local and global organization properties of the brain network can be extracted, in order to investigate both segregation and integration of the network, from weighted or binary brain graphs. While the former retains all the connections between the nodes, the latter merely denotes the presence or absence of connections according to a given threshold. The use of thresholded binary graphs has been attractive because it reduces overwhelming number of connections improving the further analysis of the meaningful information. Moreover, it the seems to facilitate the extraction of the network measures while reducing the computational burden of the graph analysis. Although there is no current consensus on what threshold should be applied, there are evidences that keeping only the strongest connections (proportional thresholds), rather than excluding them based on the selection of a correlation coefficient (absolute thresholds), seems to be improve the network measure stability [7].

Objectives

The aim of the study for this dissertation is to compare the lesioned and non lesioned hemispheric functional networks, using the graph theory method for resting-state fMRI data processing and conclude about the contribution of these findings in the pre-surgical planning. For this purpose, resting-state fMRI data is pre-processed in order to construct the functional connectivity matrices. The entries of those matrices correspond to the weights of the functional connections between the brain regions. Further, they will be thresholded through the application of a range of proportional thresholds as a way to narrow the overwhelming number of connections. The construction of these thresholded binary matrices aims to facilitate the extraction of relevant information. However, the selection of proportional thresholds requires balancing the elimination of weak connections, while avoiding the removal of the strong and the significant ones. The application of different thresholds will also be evaluated. Further conclusions should also contribute to disclose what specific threshold(s) retain(s), as much as possible, the significant information ensuring complete and stable network results.

The investigation of the lesion-induced perturbations in the networks is based on the calculation of topological network measures, including segregation and integration properties. Further, a comparison between the results of lesioned and non lesioned network properties will be performed.

Finally, it will be evidenced the usefulness of the results respecting the resting-state graph theory analysis in a pre-surgical environment.

Dissertation Overview

This section presents a brief description of the topics covered in each chapter in order to provide an enlightened reading.

Chapter 2. Background reviews the background literature related to the work developed in this dissertation. It provides some basic aspects about the brain anatomic structure and its within connections, followed by a brief description of brain lesions. Further, brain mapping methods commonly used for surgical planning are explored, highlighting the functional magnetic resonance imaging and its approach, resting-state fMRI. Besides, techniques for the analysis of the acquired data are described, including the graph theory analysis. Lastly, a contextualization of this study in the line of investigation of previous studies is reported.

Chapter 3. Methods details the steps applied in the current study, undergoing a brief report of the participants, the image acquisition and the data pre-processing protocols, followed by a detailed description of the software available for the implementation of the processing stages, emphasizing BRAPH. For the latter, its functionalities are explained as well as the methodology applied in this study. Moreover, the statistical analysis of the graph theory results obtained using BRAPH is described.

Chapter 4. Results reports the processing results obtained from graph theory analysis when applying different proportional thresholds in both lesioned and non lesioned hemispheres. Furthermore, the corresponding statistical results are reported.

Chapter 5. Discussion discusses the graph theory results of each hemisphere establishing a relationship between them and the thresholds. Furthermore, it compares the lesioned and non lesioned hemispheres. Ultimate analysis regards the comparison of the findings of this study with that of previous studies.

Chapter 6. Conclusion provides the overall conclusions and the limitations of the current study integrated with suggestions for future work.

Chapter 2

Background

This chapter intends to explain the relevance of the study developed in this dissertation and contextualize it with previous investigations.

First, the most significant anatomical brain structures will be explored as well as their divisions and corresponding connections. Once a general view of the brain is exposed, different brain pathologies (including those that the patients enrolled in this study suffer from) will be discussed including the suitable treatment or therapy approaches and, auxiliary techniques to execute them, as accurate as possible. The gold standard, the latest and the most promising methods to record and analyse the brain activity will be matched, highlighting and describing, in detail, the ones that will be used in this study.

Ultimately, a set of investigations resorting to the described methods for data acquisition and their corresponding analysis will be reported to support the line of investigation involving this study.

2.1 Neuroanatomy

The brain is the main structure of the nervous system that is located inside the cranial cavity. It can be subdivided into the cerebrum, the brain stem, and the cerebellum [8]. Unlike the brain stem, cerebrum and cerebellum structures are organized into right and left hemispheres [9]. The brain stem allows the connection of the spinal cord to the cerebrum (Figure 2.1). Posterior to this structure is the cerebellum which consists of two hemispheres joined by a median vermis. Regarding the cerebrum, it is situated in the anterior and middle cranial fossae of the skull, occupying the whole concavity of the vault of the skull. Therefore, the cerebrum is considered the largest part of the brain. In each brain hemisphere there is the cerebral cortex (which consists of six lobes on each side: frontal, parietal, temporal, occipital, insular and limbic), underlying cerebral white matter, and a complex of deep grey matter masses - the basal ganglia. Furthermore, there are fissures and gyri that separate the insula and the lobes from each other. The central sulcus is a prominent landmark that separates the frontal and parietal lobes, being the frontal lobe anterior to it while the parietal lobe occupies the posterior area. Another important fold is the lateral sulcus that connects the frontal and parietal lobes to the temporal one. Furthermore, the insular cortex lies deep within the lateral sulcus. Communicating to the temporal lobe are the hippocampus and amygdala, both parts of the limbic system. Besides, the limbic system also includes the limbic lobe which contains the parahippocampal, cingulate and subcallosal gyri. Lastly, the parieto-occipital sulcus marks the boundary between the parietal and occipital lobes [8].

In Figure 2.1, the principal gyri, sulci and other structures are represented including the ones already mentioned.

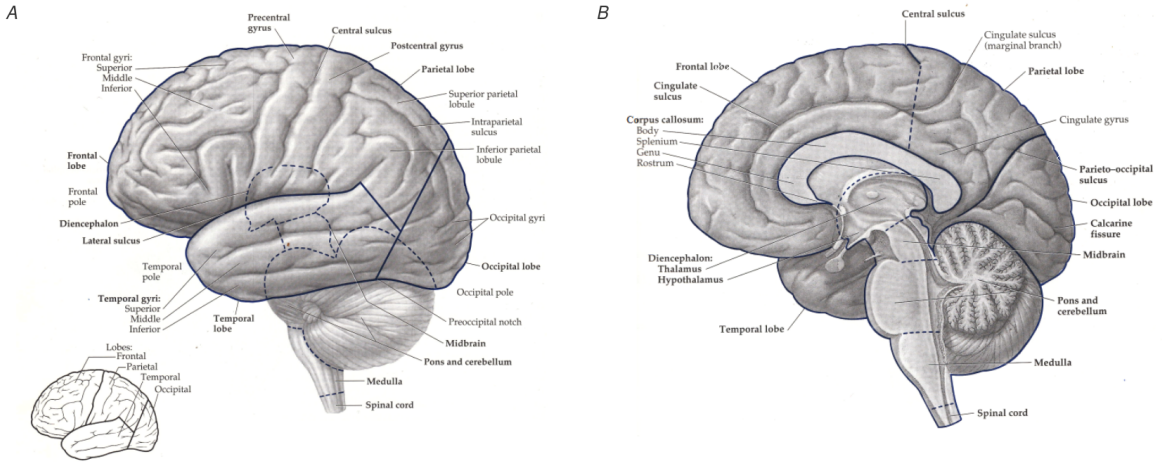

Figure 2.1: ***A***. Lateral surface of the left cerebral hemisphere and brain stem and a portion of the spinal cord. ***B***. Medial surface. Boldface labeling indicates major brain divisions of the central nervous system or lobes of the cerebral cortex. The inset shows the four lobes of the cerebral cortex [10].

This section detailed the most general anatomical structures of the brain and a few connections that establish an anatomical communication between them. This understanding is crucial when exploring different lesions occurring in the brain, as well as their diagnosis and therapy methods. All these information and techniques will be further discussed in Sections 2.2 and 2.3.

2.2 Brain lesions

The brain, as a part of the central nervous system, is composed by individual cells whose internal genetic material (deoxyribonucleic acid – DNA) is responsible for their normal function. If a mutation or an error is developed, then its function is disrupted leading to an abnormal cell. Moreover, the growth, division, and production of more abnormal cells can originate a visible space-occupying tumor [11]. For each space-occupying lesion, inflammatory or vascular disease should be considered before a neoplasm is diagnosed. As one of the most common central nervous system vascular malformations, the cavernomas correspond to cavernous malformations. These lesions on histology characteristically lack mural elements of mature vascular structures and intervening parenchymal neural tissue [12].

The effects of a brain lesion include the abnormal neurovascular coupling, compromising the blood flow circulating in the normal brain tissue. Furthermore, a space-occupying lesion not only affects the areas where it is located but also can disturb the surrounding normal cells by creating pressure on a section of nearby normal brain [11]. Despite cavernomas being more often clinically quiescent, they can also be dynamic lesions that can grow, as well as tumors. This expanding characteristic may reveal a more difficult to remove without injuring the normal brain structures and blood vessels. Considering these brain lesion's consequences, different therapies can be approached: radiation therapies, which resorts to high energy enough to kill the cells; chemotherapy, which relies on the use of drugs to avoid the growth and division of the tumor cells; and neurosurgery that involves a complete or partial resection of the lesion. The selection of the suitable therapy approach or the order of its application depends on the results of diagnosis [12]. Even so, neurosurgery has been a safe solution for a number of patients with

brain lesions with satisfactory outcomes involving the maximal lesion resection improving the symptom management, quality of life and overall survival.

2.3 Surgery planning

In the context of surgery therapy and removal of brain lesions, the goal is to remove the affected zones, with the preservation of the eloquent areas while minimizing post-operative neurological deficits. Even so, some obstacles may compromise the resective surgery, such as when those areas cannot be identified or when it is impossible to remove them because they are located in eloquent cortex. To avoid these situations, there are a number of different anatomical and functional tests that work on the pre- or intra-operative mapping of the extent of the lesion region.

2.3.1 Brain imaging techniques

The process of the surgical removal of a brain lesion requires planning the best methods for maximize the amount of the tumoral mass that is removed while minimizing the risk of causing permanent deficits. The traditional approach is to establish a relationship between eloquent cortex and the lesion's borders. However, a precise localization of these brain areas merely based on anatomical landmarks is hampered by the distortions due to the presence of the lesion.

In response to these challenges, functional mapping in individual patients has become an important procedure for surgical planning. Currently, there are several techniques that can be applied for that purpose. As a gold standard method for functional mapping, the invasive cortical mapping is highlighted. Direct cortical stimulation (DCS) is managed perioperatively while the patient is awake or in a pre-surgical context with implanted subdural grids. Under these conditions, stimulation-induced disruption provides information about the location of eloquent cortex. Nevertheless, the invasive functional mapping leaves little time to analyze the results and discuss the options due to the short time of this acquisition before the resection. Another drawback is the lack of information about deep brain structures, because the subdural grids only record the electrical potential on the brain surface [13]. Further invasive techniques used in neurosurgery include Wada test which has been the traditional standard procedure for pre-surgical testing of language and memory lateralization. The procedure involves the injection of a barbiturate into the internal carotid artery of a hemisphere via a catheter, anesthetizing it. Subsequently, the contralateral hemisphere is examined using language and memory tests. Nevertheless, this procedure reports a neurological complication rate of 1.3%, with 0.5% of which being permanent [14]. Despite being considered gold-standard methods for mapping brain functions, both require the subject to be conscious and cooperative. Furthermore, the invasive nature of the DCS and the Wada test led to the need for non-invasive procedures.

During the last decades, the development of non-invasive neuro-imaging techniques has allowed the improvement of brain mapping in a pre-surgical planning, without compromising the patient. These may include electric source imaging (ESI), resorting to electroencephalography (EEG), positron emission tomography (PET), magnetoencephalography (MEG) and functional magnetic resonance imaging (fMRI). Succinctly, EEG refers to a non-invasive method that records the potentials of the brain electrical activity, over a period of time, attaching electrodes through the subject's scalp. Consequently, the obtained data represents the time-series of scalp potential maps. ESI allows the estimation of the electric sources underlying these maps. So, besides having high temporal resolution, the significant spatial limitations of scalp EEG, and the distortion due to the skull and scalp show the weakness of the EEG technique, when

applied alone [15]. In the last 10-20 years, non-invasive functional neuro-imaging techniques have been developed and improved in their usefulness in the pre-surgical assessment of critical areas. PET relies on the use of radioisotopes that are inhaled or injected into the subject's body. Emissions are measured with a gamma-ray detector system which allow for the construction of functional images. These results provide useful information of the cerebral blood flow or brain metabolism and the parts of the brain that are activated during various tasks. However, PET scanning reveals a lack of detailed resolution constituting a disadvantage of the technique. Regarding MEG, it is a technique that measures extracranial magnetic fields produced by intracellular neuronal currents, with a high temporal resolution. Localization of this activity allows mapping the brain regions involved in specific functions. Unlike EEG, MEG signals are unaffected by tissue defects of the brain and skull bone [16]. However, the sensitivity and therefore the spatial resolution of MEG source imaging are uneven across the brain. The reason encompasses the MEG sensors that are maximally sensitive to signals due to sources tangential to the scalp (sulcal walls and gyral sources located near them), and minimally sensitive to radial sources (troughs of sulci and crests of gyri) [17][18][19].

2.3.2 Magnetic Resonance Imaging

By the 1980s, magnetic resonance imaging (MRI) became clinically prevalent in terms of the structural brain scanning [20]. Nowadays it is probably the most powerful tool for researchers and neurosurgeons today due to the fact that it provides information about brain anatomy as well as information on how the brain functions [21]. It is based on the ability of protons being magnetically excitable to return electromagnetic signals and generate an image.

The human tissue is abundantly composed by hydrogen-containing compounds, notably water. Hydrogen nuclei (i.e., protons) possess particularly favorable magnetic properties due to its rotation like a spin top around their own axes inducing a small directed magnetic field. The strong magnetic field of the MRI machines (B_0) induces the reorientation of the spins from randomly oriented to aligned (parallel) or against (antiparallel) in line with that field, respectively corresponding to lower and higher energy states. Since a slightly larger proportion of spins aligns parallel to the scanner magnetic field, the body gets magnetized. The bulk magnetization due to this excess number of spins is called M_0.

The spins also precess about the axis of the external B_0 field with a frequency depending on its strength which is called the Larmor or resonance frequency (ω_0) and it can be obtained through the Expression 2.1.

$$\omega_0 = \gamma B_0 \tag{2.1}$$

Where γ refers to the gyromagnetic ratio, which is a constant unique to every atom.

The application of a 90° electromagnetic pulse, also called a 90° radio frequency (RF) pulse, with the same frequency as the proton's precession frequency leads to the excitation of the protons, in phase, by absorbing the transmitted energy. The standard spin echo pulse sequence uses a series of 90° pulses separated by a period known as the time repetition (TR). By absorbing the transmitted energy, the spins flip from the parallel to the antiparallel states. The phase precession means that the magnetization vector M_0 rotates towards the xy plane (transverse) which is perpendicular to the static magnetic field B_0. Thus, the magnetic field of the spins adds up to form a new magnetic field M_{xy} in that transverse plane, inducing

a detectable current flow in the receiver coil of the MRI machine, as represented in the Expression 2.2.

$$M_{xy} = M_0 e^{-t/T2} \tag{2.2}$$

However, when the RF transmitter is turned off, the phase precession is not stable: the interactions between the magnetic fields of the protons promote changes in the local magnetic field strengths and hence to different precession frequencies. As a consequence, phase shifts between the precessing spins can occur. This dephasing or transversal relaxation decays initially rapidly but slows down over time following an exponential function with time constant T2. Due to magnetic field inhomogeneities in the static magnetic field arising from imperfections in the magnet or disruptions in the field by paramagnetic or ferromagnetic materials, the spins get out of phase faster than T2, decaying with a shorter time constant T2*. Furthermore, susceptibility agents that are present in the tissues as elements with unpaired electron spins can also accelerate this dephasing process. Since, T2* depends on the homogeneity of the main magnetic field and on the agents that disrupt the local magnetic field environment, it is clear the significant decrease in T2* [22].

The dephasing effect can be reversed by the application of a 180° RF pulse which reverses the order of the spins. Considering its application at time t=0, after t=τ, the spins are out of phase and in t=2τ they are back in phase again producing a large signal denominated the spin echo. Therefore, 2τ is called the echo time (TE).

Besides dephasing, the spins reorient themselves with the direction of the B_0 due to the excited spins slowly returning to the low energy state and consequently realigning with the external magnetic field. This process is called longitudinal relaxation and progresses slower than the dephasing process. The recovery of the longitudinal component M_z follows an exponential function with time constant T1 as indicated in the Expression 2.3.

$$M_z = M_0(1 - e^{-t/T1}) \tag{2.3}$$

The differences in T1, T2 and T2* (along with the proton density variations and blood flow) explain the high contrast in MRI. Understanding this influence requires the association of the molecular motion and size with the intrinsic magnetic inhomogeneities and the molecular vibrational frequencies. As the molecular size increases, its motion is reduced, increasing the intrinsic magnetic inhomogeneities. Then, the magnetic field variations are more readily manifested and the T2 decay is shorter [22].

Moreover, larger and slowly moving molecules exhibit low vibrational frequencies that concentrate in the lowest part of the frequency spectrum. As a result, the energy transfer is less efficient because the precessional frequency of the excited protons does not easily overlap with their vibrational frequencies. Since T1 relaxation depends on the dissipation of the absorbed energy in the surrounding molecular lattice, large molecules exhibit a longer T1 decay [22].

Functional magnetic resonance imaging (fMRI)

In the early 1990s, researchers discovered that the changes in the blood oxygenation could be measured using the MRI technique [20]. Since then, fMRI imaging has been offered as a non-invasive method to measure and localize specific functions of the human brain without the application of radiation. The principle of fMRI for the assessment of the brain function involves the detection of local hemodynamic changes in capillaries and draining veins of functional areas. The most common method of fMRI for this detection is based on the blood oxygenation level dependent (BOLD) effect which relies on the dif-

ferent magnetic properties of oxygenated (diamagnetic) and deoxygenated (paramagnetic) hemoglobin to generate image T2* contrast. Neuronal activity increases local cerebral oxygen consumption, which results in a decrease of oxygenated hemoglobin and in an increase in deoxygenated hemoglobin in that functional area. In response, an increase of regional cerebral blood flow and volume (perfusion) in capillaries and draining veins is enhanced within several seconds compensating the initial decrease. During this oversupply phase (hemodynamic response), the deoxygenated hemoglobin concentration decreases resulting in a more homogeneous local magnetic field. As follows from the description in Subsection 2.3.2, excited spins dephase faster when inhomogeneities are inspected in the magnetic field leading to a shorter T2*. As opposite, the excited spins dephase slower in a more homogeneous local magnetic field resulting in an increase of the T2* and hence in a stronger measured T2*-weighted MRI signal. Thus, the change in the local oxy- and deoxygenated hemoglobin ratio and its associated change in the magnetic field homogeneity act as a marker of neural activity [23]. Thanks to the high spatial resolution and non-invasiveness of the technique, the popularity of fMRI for the study of brain function has greatly increased during the last decades. In task-based fMRI (tb-fMRI), the subjects perform a specific task in order to not only target distinct functions, such as language or motor functions, but also to localize the corresponding brain regions involved in those. Thus, neurosurgeons are enabled to spare eloquent brain tissue in invasive procedures such as tumor or another lesion removal [24]. Thereby, pre-surgical mapping aids in balancing long-term survival by maximizing the extent of lesion's resection while preserving the patient's functional cortex. Nevertheless, the task-based fMRI can fail in patients who cannot perform the tasks satisfactorily because of developmental brain disorders, altered levels of consciousness or brain lesions close to eloquent areas. Furthermore, the task-based mapping of eloquent cortex only allows mapping a limited number of functional areas due to clinical time constraints, making it difficult the mapping of the entire brain network and limiting the parcellation of eloquent cortex.

2.3.3 Resting-state functional magnetic resonance imaging

For the last two decades, resting-state fMRI (rs-fMRI), a task-free approach, has emerged as an effective adjunct to tb-fMRI. Nowadays, its evaluation in pre-surgical mapping of eloquent cortex intends to overcome some of the limitations referred for task-based fMRI. The principle of resting-state fMRI is also based on the BOLD signal fluctuation, as task-based fMRI, although the focus is now on spontaneous BOLD signal alterations [6]. The analysis of this spontaneous activity, acquired while subjects are at rest, revealed synchronous low-frequency ($<$0.1 Hz) fluctuations in the BOLD signal that formed coherent networks of neural activity [15]. Examples of that include the auditory, visual, sensory-motor and default mode networks. The rationale is that brain regions that are intrinsically and functionally connected share similar time-courses and can, therefore, be separated from others. Comparing to task-based fMRI, beyond the absence of a task, the resting-state imaging protocol is typically faster and the collected data serve multiple mapping purposes which proposes a more time-efficient method. Furthermore, in tb-fMRI, the percentage of the BOLD signal increase between two conditions is generally small. As opposite, in the resting-state technique, since the BOLD signal oscillations proper are studied, then the signal-to-noise ratio is higher than task-related signal increases [24].

The focus of this study respects the rs-fMRI data processing, rather than the pre-processing procedures that are previously required for the data analysis. Thus, the rs-fMRI data pre-processing will be briefly described in Part 2.3.3, while a more detailed explanation of the available techniques for the processing analysis will be done in Subsection 2.3.4. Regarding the processing methods, the graph theory analysis will be separately highlighted due to its relevance and application in this study, unlike the other

processing approaches.

Resting-state fMRI data pre-processing

After the BOLD signals acquisition, their analysis must be inferred. Owing to the massive amount of data and the need for a sophisticated analysis, the resting-state fMRI data analysis is challenging. However, to further proceed for this analysis, the resting-state data needs to be primarily pre-processed, mainly through the following steps: realignment, coregistration, slice timing correction, segmentation, normalization, smoothing, nuisance covariates regression and temporal filtering [6].

The realignment respects the correction of the head motion allowing for the movement's effects to be discounted when looking for brain activations. Motion correction operates by selecting one functional volume of a run as a reference to which all other functional volumes are aligned. Most head motion algorithms describe head movements by six parameters, three translation (displacement) and three rotation parameters, which characterize the motion of rigid-bodies. These six parameters are estimated iteratively by analyzing how a source volume should be translated and rotated in order to better align with the reference volume.

Furthermore, a coregistration procedure is desirable. This method focuses on the head motion correction between structural and functional images. Although the structural and the functional images are acquired during the same scanning session, they are often not completely aligned with each other mainly because the subjects move throughout the session. The coregistration procedure by mutual information attempts to maximize the mutual information between the intensity of one image and the intensity of the other [25].

Moreover, the images must be pre-processed in such a way that the resulting data appears as if all slices of a functional volume, which are scanned sequentially in time, were measured at the same time moment. Thus, a slice timing correction is applied to temporally resample all slices within a functional volume so they can be represented at the same time point.

The data for each subject are classified into a number of different tissue types (e.g., grey matter (GM), white matter (WM), cerebrospinal fluid (CSF) and bone). These are defined according to tissue probability maps which determine the prior probability of finding a tissue type at a particular location. Therefore, those maps are used to segment the grey and white matter images and cerebrospinal fluid images from the coregistered structural image. Extra tissue maps can be generated including bone and soft tissue. This procedure corresponds to the segmentation pre-processing step.

Given the observed variance (after realignment) and estimated movements, the rate of the deformation change with movement can be computed. Therefore, each voxel of the deformation field contains the x, y and z mm coordinates of where the deformation space points.

Resorting to the deformation field, the coregistered structural image is transformed to match a template data (normalization of the structural image) and apply the parameters obtained to the functional images. The two most widely used templates are the Talairach and Montreal Neurological Institute (MNI) atlases. While coregistration is performed on data from a single subject, normalization is usually performed on data from multiple subjects [26].

Lastly, the previous normalized images are smoothed to suppress noise and effects due to residual functional and anatomical differences during the inter-subject averaging. Smoothing the images intends to filter out the high-frequency spatial noise and thereby improve the signal-to-noise (SNR) ratio. This process involves the convolution of the image volumes with a Gaussian kernel of a specified width that determines the weights used to include surrounding voxels in the average. In brain imaging, the

bandwidth is usually measured in terms of the full width at the half maximum (FWHM) of Gaussian kernel [26].

Despite the head motion has already been corrected, the procedures for this correction are not usually sufficient to correct for all the signal changes due to the head motion. The most common approach to regress out the head motion artifacts is to add the time series of the six estimated realigned parameters as nuisance regressors in a regression model [25]. Even so, Satterthwaite et al. [27] reported that high-order models seemed to benefit in removing head motion effects such as the Friston 24-parameter model. This model resorts to the six head motion parameters, used in the realignment plus six head motion parameters one time point before and the twelve corresponding squared items [27]. In addition, the cerebrospinal fluid and the white matter signals and the global mean signal should also be removed as nuisance variables to reduce the effects of head motion and non-neuronal BOLD fluctuations, including the respiratory and cardiac cycles [28].

For the analysis of the spontaneous activity revealed at low-frequency fluctuations in the BOLD signals, a temporal filter range between 0.01 and 0.1 Hz is also applied reducing the effect of very low- and high-frequency noise.

As explained above, since the focus of this study involves the processing of resting-state fMRI data, Subsection 2.3.4 will be exclusively dedicated to the explanation of several processing methods.

2.3.4 Resting-state fMRI data processing

Once the pre-processing analysis of the resting state images is complete, the further evaluation of the function of specific brain regions or the functional connectivity between distant brain regions can be proceeded. Analytic approaches can be broadly divided into two types: functional segregation (which focuses on the local function of brain regions and is mainly used for brain mapping) and functional integration (which relies on the functional connectivity between distributed brain areas and assesses the brain as an integrated network). Functional segregation and integration techniques rely on the analysis of rs-fMRI activity and connectivity, respectively [6].

Functional segregation methods

Amplitude of Low Frequency Fluctuations (ALFF) and Regional Homogeneity (ReHo) are methods commonly used in functional segregation analyses. They reflect different aspects of regional neural activity but do not provide information on functional connectivity. Regarding the ALFF method, it measures the total power of the BOLD signal usually within the low-frequency range between 0.01 and 0.1 Hz [6]. The advantage of the ALFF respects the simplicity of the analysis without any underlying hypothesis. ReHo analysis is a voxel-based measure of the similarity between the time-series of a given voxel and its nearest neighbors, as calculated by the Kendall coefficient of concordance of the BOLD time-series. It is usually calculated within a low-frequency range (typically between 0.01 and 0.1 Hz). A higher ReHo value represents higher coherence and centrality of regional brain activity. Areas that overlap in ALFF and ReHo represent regions that are not only active at the same time frequency but are also active in synchrony with neighboring voxels. Both ALFF and ReHo methods do not require any *a priori* definition of the region of interest (ROI), although they can be used to define an ROI for seed-based functional connectivity analysis. The study of functional segregation has gradually receded in favor of the study of functional integration because the brain is more appropriately seen as an integrated network rather than isolated communities of regions [6].

Functional integration methods

Functional integration emphasizes the functional connectivity between distributed brain regions which relates the measurement of the degree of synchrony of the BOLD time-series between them. It is the foundation of information transfer between distant brain areas. For assessing functional integration features, different computational methods are commonly used including independent component analysis (ICA) and graph analysis. The latter resorts to the ROI-based functional connectivity analysis.

The independent component analysis uses multivariate decomposition to separate the BOLD signal into independent functional networks (components) in the form of spatial maps of the z scores derived from the correlation between the time-series of each voxel and the mean time-series of that brain network. The average z score for each network indicates the magnitude of functional connectivity within the network. There are several resting-state networks that emerge from ICA analysis in rs-fMRI studies, including the default mode network, sensory-motor network and executive control network. ICA can be performed without any *a priori* assumptions, except the selection of the number of independent components to identify. Furthermore, it extracts all detectable networks within the subject. Even so, a single network can be broken into sub-networks, depending on the number of independent components specified. Moreover, the fact that the connections between communities or between different brain networks are not shown in ICA constitutes another limitation of the technique [6]. Also, the classification and extraction of independent components (ICs) in patients presents challenges such as the distorted anatomy may hinder the classification of ICs and the functional connectivity could be affected by the pathology itself [24].

The seed-based functional connectivity analysis, also called the ROI-based functional connectivity analysis, finds regions that are correlated with the activity of the seed region. In this method, the cross-correlation is computed between the time-series of the seed and those of the rest of the brain. The coupling of activation between different brain areas indicates that they are involved in the same functional process and thus they can be interpreted as functionally connected. The overall connectivity of the brain using this method can be visualized by a connectivity matrix, showing the strength of all connections between seed regions within the brain [6]. Unlike ICA, this analysis only extracts the regions functionally connected to the ROI. However, and even requiring *a priori* determination of the seeds which can either be hypothesized, based on prior results or derived from ALFF and ReHo calculations, their computation is simple with an intuitive interpretation of the results.

Recently, the brain has emerged as a wide spread communication network where the information is exchanged between its components. The development of this realistic model and the corresponding computation of its properties conduced to the combination of the ROI-based functional connectivity analysis with the graph theory analysis applied to complex brain networks. The graph theoretical techniques is described in Subsection 2.3.5 coupling the construction of the brain network.

2.3.5 Graph theory analysis

Graph theory has been extensively used to examine the properties of complex networks which consist of neural regions (nodes or vertices) and the corresponding functional connections (edges or links), forming the connectome. The graph analysis can be automatically performed without any *a priori* assumptions. However, the results are often not intuitive and may be difficult to interpret. Applying to rs-fMRI, this approach reveals a highly efficient organization of the brain network optimized towards a high level of local and global efficiency, referred to as small-world topology. A network that shows a small-world nature is characterized by attenuated local connections and few distant connections, in

which most nodes are not connected to one another, but they can be reached from every other node through a small number of connections. These few connections facilitate efficient information delivery at low wiring and energy costs [6]. For the connectome analysis, the functional brain network has been revealed to be organized as a small-world and its investigation seems to be attractive to neurosurgeons not only for the principle of mapping brain connectivity but also because it allows the modulation of lesions and plasticity [29]. Those functional networks can be defined as a graph (G) as a function of vertices (V) and edges (E), represented by $G = f(V,E)$ [6]. First, the graph theory analysis requires the definition of the nodes, known as parcellation. Once nodes have been established, the level of functional connectivity between two nodes (E) is defined resorting to the correlation between the time-series of the pairs of nodes. Frequently, the Pearson correlation coefficient, whose relation between two regions is linear, is used. Further, the data are organized into a two-dimensional correlation matrix, where nodes are represented by rows and columns, and edge weights are indicated by the matrix entries, as each entry lies at the intersection of a row and column [15].

Network construction

The correlation matrix can be binarized denoting the presence or absence of the connections. If no binarization is applied, then the obtained graphs are weighted, meaning that they contain information about the connection strengths [30]. With weighted graphs, the edges denote that each node is connected to every other node. The correlation matrix can be characterized as directed and not symmetric if node j is connected to node k without node k needing to be connected to node j. The opposite relates the obligation of node k being connected to node j if node j is connected to node k. Consequently, the matrix is symmetric and undirected with the jth entry of the ith row equal to the measured connectivity between brain region i and j [31]. In order to transform a directed graph into an undirected graph, the connectivity matrix needs to be symmetrized.

However, the weighted graphs revealed to be less computationally efficient, especially in the analysis of large-scale networks such as voxel-based functional connectivity networks. Moreover, the overwhelming number of connections makes it difficult to extract meaningful information. Thus, the use of thresholded binarized graphs has been attractive because it facilitates the calculation of several network measures and reduces the computational burden of analyzing the graph [7].

To obtain a binary graph from a weighted correlation matrix, it is assigned a value of 1 to the edges above a given threshold and 0 to those below it. There are mainly two ways of applying a threshold: (a) by selecting a correlation coefficient as the cut-off value below which all connections are excluded from the analysis - absolute threshold; and (b) by fixing a set percentage of the strongest connections (edges) to all - proportional threshold or edge density. The choice between them becomes significant when comparing different groups of subjects, as it may lead to different results [31]. For group comparisons, using a proportional threshold ensures that the networks in each group have the same number of nodes, or network size, and the same number of edges. This allows for more meaningful comparisons of other network measures that rely on the connections of a node. However, proportional thresholds do not take into account absolute differences in correlation values. Therefore information about overall group differences may be lost. Absolute thresholds retain this information, but may result in networks with different size, or in a network that is connected in one group but disconnected in the other [7]. Moreover, absolute thresholds may be too large for low-average connectivity or too small for high-average connectivity networks, thus eliminating strong and significant connections or overemphasizing weak connections. The application of proportional thresholds has become more common in graph theoretical analyses of human

brain networks [31]. According to Garrison et al. [7], network measures seem to be more stable using proportional rather than absolute thresholds. Furthermore, the instability of network measures at very high or very low thresholds is expected and is related to the calculation of these measures as the graph becomes more or less connected. The current findings demonstrated, however, that network measure instability is not restricted to extreme thresholds, but occurs within reasonable, commonly applied ranges [7].

Network measures

Once the graph of the functional network has been created, its properties can be characterized using a range of graph theory measures with particular interest in the study of network segregation and integration [15]. Thus, different network properties can be computed including the integration metrics of characteristic path length and global efficiency. For the segregation analysis, the clustering coefficient and local efficiency measures can be calculated. Each node of the network can also be characterized in terms of its integration and segregation properties by the calculation of the nodal property of the graph metrics, when applicable. It should be noted that some graph measures exclusively describe the topological parameters of the global network.

Furthermore, the small-world networks should be simultaneously highly segregated and integrated reflecting an optimal balance of functional integration and segregation. However, the small-worldness may also falsely report a small world topology in highly segregated but poorly integrated networks. Consequently, it should not, in general, be regarded as a substitute for individual assessment of integration and segregation properties [30].

Network integration

Network integration measures the connectedness of distinct regions, that is, the ability to combine information for distributed brain regions. Measures of integration are characterized by estimating the ease with which brain regions communicate.

A measure that can be assessed in a graph is the shortest path length, which relates the shortest distance between two nodes. In a binary graph, the distance is measured as the minimum number of edges that need to be crossed to go from node i to node j. The average of the shortest path length between one node and all other nodes of the network is the characteristic path length (L) and it is computed by the Expression 2.4 [31].

$$L = \frac{1}{N(N-1)} \sum_{i \neq j} \min L_{ij} \tag{2.4}$$

Where N is the number of nodes of the network and $\min L_{ij}$ is the minimum number of edges that need to be crossed to go from node i to node j.

A short characteristic path length implies the effective integrity and rapid information propagation between and across the different brain regions. In contrast, a long characteristic path length may reflect disrupted neuronal integration between the regions [32].

Related to the shortest path length is the global efficiency $E_{nodal-glob}$, in the way that shorter path lengths are associated to a more efficient information transfer between the nodes. Due to this inverse relationship, the global efficiency is defined as the inverse of the shortest path length from one node to

any other nodes in the network [31]. It is calculated by the Expression 2.5.

$$E_{nodal-glob}(i) = \frac{1}{N-1} \sum_{i \neq j \in G} \frac{1}{L_{ij}} \tag{2.5}$$

Where L_{ij} is the shortest path length from node i to j and is defined as the sum of the edge weight w_{ij} along this path. N is the number of nodes of the network G.

Global efficiency can be further averaged over all nodes to describe global properties of the brain network. It is nominated as E_g and calculated by the Expression 2.6 [31].

$$E_g(G) = \frac{1}{N} \sum_{i \in G} E_{nodal-glob}(i) \tag{2.6}$$

Where N is the number of nodes of the network G and $E_{nodal-glob}(i)$ is the global efficiency of the node i obtained from the Expression 2.6.

Network segregation

Network segregation relates the ability for specialized processing to occur within densely interconnected groups of brain regions, known as clusters.

A measure that assesses the presence of clusters in a network concerns the clustering coefficient (C_i) and it can be calculated using the Expression 2.7 [31].

$$C_i = \sum_{i \in G}^{N} \frac{\#E_i}{\#V_i(\#V_i - 1)/2} \tag{2.7}$$

Where $\#E_i$ is the number of edges connecting the neighbors of node i and $\#V_i$ is the number of neighbors of node i in the network G.

The clustering coefficient of a node reflects the level of local connectedness of a node and therefore it can range between 0 and 1 ($0 < C_i > 1$). The highest value of 1 indicates that the connections between the nearest neighbors of a node that actually exist respect all the possible connections. The opposite occurs when the clustering coefficient is 0 reflecting no local connections around a node [33].

From the whole network, the clustering coefficient of all nodes can be averaged into the mean clustering coefficient (C) and calculated by the Expression (2.8) [31].

$$C = \frac{1}{N} C_i \tag{2.8}$$

Where N is the number of nodes of the network G and C_i is the clustering coefficient for the node i calculated using the Expression 2.7.

To assess the communication efficiency between a node and its neighbors, the local efficiency $E_{nodal-loc}$ can be calculated resorting to the Expression 2.9 [31].

$$E_{nodal-loc}(i) = E_g(G_i) \tag{2.9}$$

Where $E_g(G_i)$ denotes global efficiency of the sub-graph composed by the nearest neighbors of node i.

High local efficiency indicates that a node is embedded in a richly connected environment. Low local efficiency, by contrast, means that the neighbors of the node are sparsely connected to one another [34]. For local efficiency, its global measure nominated as E_{loc} can be computed using the Expression 2.10 [31].

$$E_{loc}(G) = \frac{1}{N} \sum_{i \in G} E_{nodal-loc}(i) \tag{2.10}$$

Where N is the number of nodes of the network G and $E_{nodal-loc}(i)$ is the local efficiency of the node i obtained through the Expression 2.9.

The local efficiency averaged across all the nodes of a network represents the network's potential for the local information transfer [34]. The nodal global efficiency ($E_{nodal-glob}$) and nodal local efficiency ($E_{nodal-loc}$) measure the capacity of information propagation of the given node with all other nodes in network and their direct neighbors, respectively [35].

Network integration & segregation

The small-worldness (SW) was already introduced as a measure for both the integration and segregation of the network. This derives from its ratio between the mean clustering coefficient (C) and the characteristic path length (L), both normalized by the corresponding values calculated on random graphs, respectively C_{rnd} and L_{rnd} for clustering coefficient and characteristic path length. This calculation is indicated by the Expression 2.11 [31].

$$SW = \frac{\frac{C}{C_{rnd}}}{\frac{L}{L_{rnd}}} = \frac{\gamma}{\lambda} \tag{2.11}$$

Where C_{rnd} and L_{rnd} are, respectively, the clustering coefficient and characteristic path length of a set of random networks. γ and λ are the corresponding normalized clustering coefficient and normalized characteristic path length, respectively.

Taking both concepts of clustering coefficient and characteristic path length into account, the small-world network is characterized as having similarly short paths but significantly higher clustering coefficient. When a network reveals a small-world topology, this indicates an optimal organization for information processing and a balance between local processing and global integration in the brain. It is, then, quantified by a small-worldness higher than 1 ($SW > 1$) [36] [33].

2.4 State of the Art

Recently, resting-state fMRI has been considered as a complement or an alternative to task-based fMRI for brain mapping in the pre-surgical evaluation of the maximal lesioned area that can be resected without injuring eloquent cortex. The evidence of this usefulness has been investigated both qualitatively and quantitatively. Rosazza et al. [5] compared resting-state and task-based fMRI techniques in mapping the motor functions in patients with lesions close to sensory-motor cortex. The extraction of the sensory-motor cortex from the resting-state fMRI data was either achieved by the application of ICA or seed-based analysis. Further comparisons of sensitivity and specificity of rs-fMRI with respect to tb-fMRI were included in the study. The results indicated that the rs-fMRI can localize the sensory-motor

cortex successfully, providing anatomical specificity, in particular with seed-based analysis. They found a partial agreement between the two techniques which reveals that rs-fMRI can work as a supplement of tb-fMRI when patients are unable to perform a task.

Similarly, Branco et al. [24] compared resting-state networks with task-related activity but for language mapping in the brain, in patients with brain tumors and epilepsy. Resting-state networks were extracted only applying the ICA. Their results revealed a good overlap between task-related activity and resting-state language maps, particularly within the language regions of interest (ROIs) suggesting that resting-state protocols may be as suitable as the task-based ones to map the language networks.

In summary, the discovery of low-frequency temporally correlated BOLD signals in spatially distant parts of the brain at rest has provided evidence for the existence of the functional networks within the brain, as the sensory-motor and the language networks. Furthermore, there is a resting-state network called the default mode network (DMN) which has been linked to the spontaneous thought processes or self-oriented mental activity that define the brain's resting state. Therefore, when executing a resting-state fMRI protocol, this network can be extracted [37].

Thus, this successful extraction of resting-state networks justifies the application of the corresponding fMRI technique in patients with lesions that difficult a good performance of the required task. Further, its collected data serve multiple mapping purposes rather than only mapping a specific network related to the task as occurs in tb-fMRI.

Regarding the methods used for this extraction, the previous studies used the ICA or the seed-based analysis. In an attempt to represent the complex brain network more realistically and include the computation of its properties, a combination of a ROI-based functional connectivity analysis with the graph theory analysis has been applied and referred to the connectome analysis. Hart, Price, and Suckling [29] resorted to the analysis of the brain connectome, where nodes are circumscribed brain regions and edges represent the functional connectivity between them, to characterize the network topology and the connectivity alterations in patients with brain tumors. For the computation of the network properties, the functional connectivity matrices were constructed from resting-state fMRI data and further thresholded and binarized resorting to absolute thresholds. Their findings demonstrated that tumors produced a consistent reduction in local and long-distance connectivity both within and between hemispheres. These results proved the feasibility of the graph theoretical analysis to brain mapping in individual patients with brain tumors. Moreover, they calculated the network properties on thresholded binary graphs by applying a threshold based on a correlation coefficient in order to remove the weak connections of the networks. Nevertheless, proportional thresholds could also be applied to construct a thresholded binary matrices allowing a more facilitated calculation of network measures. The fact that there is no consensus on what threshold to use promoted the investigation conducted by Garrison et al. [7]. Their goal was to evaluate the stability of network properties for healthy subjects across both proportional and absolute thresholds. Overall, topological measures were more unstable across absolute than proportional thresholds. This instability was reflected by less smoothly varying shapes regarding distribution of network measures across absolute thresholds.

The favoring of the proportional over the absolute thresholds led to more researchers investigating the network topological differences in lesioned patients over a range of proportional thresholds. Park et al. [38] assessed the functional connectivity in patients with supratentorial brain gliomas with possible alterations of between-hemispheres and long-distance connectivity as well as in the network topology. They applied a graph theory analysis in resting-state fMRI data and compared the lesioned results with that of healthy subjects. The patients showed decreased long-distance between-hemispheres connectivity, when comparing the averaged functional connectivity matrix of patients with that of healthy controls

(HCs). In network analysis, patients had an increase of local efficiency but global efficiency, clustering coefficient, and small-worldness were relatively preserved compared to healthy subjects. The local efficiency increase may act as a compensatory mechanism in lesioned hemisphere for the distant connectivity decrease.

Additionally, the investigation of the network properties, the functional connectivity and their relationships with cognition impairments has been performed in lesioned patients. Furthermore, the change in the network characteristics of the lesioned areas between pre- and post-operation has been evaluated in terms of the impact in the alteration of neuro-cognitive function. Huang et al. [39] combined a study of neuro-cognitive assessment and graph theoretical analysis of resting-state fMRI to detect differences in the whole-brain network before and after tumor resection of frontal lobe low-grade glioma (LGG) and compared both with healthy controls. The functional connectivity matrices were constructed and a binary network analysis was performed over a range of proportional thresholds. They found that topological parameters were significantly different between LGG patients and HCs at the density of 20%. The clustering coefficient and local efficiency were decreased in LGG groups which implied a relatively sparse local connectedness of brain functional networks. The longer shortest path lengths and lower global efficiency in LGG groups suggested that information transfer between brain regions was more difficult in LGG patients. Furthermore, compared with the HCs, the cognitive performance in the two LGG groups were significantly lower than HCs, and the disturbed networks in the LGG were negatively related to worse cognitive scores. Thus, the altered small-world network may be responsible for cognitive dysfunction in frontal lobe LGG patients.

The integration of the connectome analysis and neuro-cognitive performance assessment has been also tested for patients with other brain lesions, besides tumors. Zhu et al. [33] attempted to identify the functional alterations in the organization of brain networks in acute ischemic stroke (AIS) and compared with HCs. From resting-state fMRI, followed by a graph theory analysis, they investigated the topological networks properties of both groups using thresholded correlation matrices over a wide range of density values. In their results, the AIS patients had significantly increased global efficiency and lower shortest path lengths but maintained the local clustering coefficient, in comparison with HCs, which indicated a tendency of the lesioned networks for transforming and propagating information among different brain circuits due to the damages caused by the ischemic stroke. Besides, they found that altered network metrics were correlated with cognitive scores. They associated the disruptions in the topological organization with poor cognitive performance in patients.

Moreover, Wang et al. [40] compared the small-world network attributes between controls and patients with white matter lesions (WMLs), with cognitive impairment. Those patients were further divided into two groups according to their cognitive performance: WMLs with non-dementia vascular cognitive impairment (WMLs-VCIND) and WMLs with vascular dementia (WMLs-VaD). They collected resting-state fMRI data and applied the graph theory for the network analysis. The functional connectivity graphs were constructed and subsequently thresholded based on a range of proportional thresholds for the calculation of network properties. They found that the overall functional connectivity strength was lowest in the WMLs-VaD patients but highest in the normal control group. Furthermore, both WMLs-VCIND and WMLs-VaD groups had lower global efficiency and higher characteristic path length, in comparison with controls, which might suggest a disruption of the information processing between distant brain regions. Thus, these findings provided additional evidence for mechanisms of cognitive impairment in WMLs patients.

The results from the previous studies conducted by Zhu et al. [33] and Wang et al. [40] respecting AIS and WMLs were concordant to the findings involving the investigations recruiting patients with

brain tumors, as the study conducted by Huang et al. [39]. Succinctly, they examined the link between functional network characteristics and cognitive functioning in patients with brain lesions at whole-brain resting-state functional networks, although not explicitly acknowledging the functional contribution of areas in the non lesioned hemisphere.

De Baene, Rutten, and Sitskoorn [34] aimed to examine whether there is an association between cognitive performance and functional network features of the non lesioned hemisphere in patients with glioma. To characterize the network properties, the correlation matrices were constructed from rs-fMRI data and further thresholded by a range of densities. The results suggested that a less segregated organization (lower local efficiency) and a better spread of information over the non lesioned hemisphere through mutually interconnected non lesioned hubs (higher assortativity) were associated with better cognition scores. These findings urge researchers to recognize the functional contribution of non lesioned, undamaged regions and to focus more on the graph metrics of the corresponding network in the search for predictors of cognitive functioning in patients with brain tumor. A critical question arising from their results is whether the differences between patients in the network features reflected lesion-induced functional changes, compensatory mechanisms, individual differences unrelated to the tumor or a combination of these.

In this context, the study in this dissertation intends to proceed the evaluation and comparison of the functional network features for both lesioned and non lesioned hemispheres of a group of patients with brain tumors and another brain lesion (a cavernous malformation). Furthermore, it is also intended to evaluate the effect of thresholding the lesioned and non lesioned networks at different levels of proportional thresholds in binary graphs. This investigation has not been incorporated in previous studies. Following the same directions as the anterior investigations, the functional connectivity matrices will be obtained from the resting-state fMRI data. Then, the thresholded binary graphs were constructed by applying a range of proportional thresholds and the hemispheric-network properties calculated. Moreover, the between-threshold analysis would disclose the effect of the proportional threshold in the topological properties of both lesioned and non lesioned networks. Ultimate conclusions respect the usefulness and relevance of these findings in a pre-surgical environment, mainly when evaluating the lesioned and non lesioned brain areas.

In the last two decades, several studies have been focusing on the investigation of the function of brain regions (segregation) and the functional connectivity between them (integration), in patients with brain lesions, resorting to the resting-state fMRI technique to acquire the brain signals. Furthermore, a graph theory analysis has been applied to calculate both segregation and integration properties of the brain network. Network measures can be evaluated in thresholded binary graphs across absolute (correlation-based) and proportional (density-based) thresholds with a purpose of facilitating their extraction and the further analysis of meaningful information. Thereby, this study aims to analyse and compare the functional network properties of lesioned and non lesioned hemispheres. For this purpose, a graph theory analysis will be performed in the resting-state fMRI data of a group of patients. Moreover, a range of proportional thresholds will be applied in both lesioned and non lesioned thresholded binary graphs to investigate the dependence of the network measures on the threshold. Lastly, it is intended to elucidate about the relevance of these results in a pre-surgical planning.

Chapter 3

Methods

This chapter reports how the current study was conducted, undergoing a description of the software, methodology and analysis options implemented. First of all, demographic information about the recruited participants as well as the parameters for image data acquisition and further pre-processing is described. Once pre-processed, the data was further analysed resorting to the graph theoretical method. For this purpose, several toolboxes can be used. Some of them will be described, including BRAPH. Since this latter software is used in this study for the functional connectivity analysis, a detailed explanation of its functionalities and a step-by-step guidance of its operation will be presented. Lastly, considering the graph measures obtained, different strategies for their statistical analysis will be reported.

3.1 Participants, image acquisition and pre-processing

The research data was provided by Sociedade Portuguesa de Ressonância Magnética/Hospital da Cruz Vermelha. A group of 7 participants, including 4 males and 3 females, were recruited in this study. Patient ages ranged between 27 and 77 years. All of them were previously referred for surgical resection of a brain lesion, either a tumor or a cavernous malformation. Their demographic details can be consulted in Table 3.1. All patients underwent a resting-state fMRI scan using a 3T magnetic resonance system (Philips Intera). The structural images were acquired with a matrix of 256×256, 160 contiguous slices, voxel size of 1.8×1.8×4 mm^3, flip angle of 8°, TR of 11 ms and TE of 4.6 ms. The functional images were obtained with echo-planar imaging (EPI) over a period of 5 min with TR of 2000 ms (2 s) for each three-dimensional volume, resulting in 150 functional volumes. Moreover, the rs-fMRI data were acquired over a matrix of 128×128, a flip angle of 90° and a TE of 23 ms. Besides, the voxel size corresponded to 1.8×1.8×3.5 mm^3. 34 axial slices were acquired individually from bottom to top, in ascending order.

The resting-state fMRI data pre-processing was carried out using Statistical Parametric Mapping (SPM version 12) (developed by members and collaborator of The Wellcome Trust Centre for neuroimaging Institute of Neurology, University College London) and Data Processing Assistant for Resting-State fMRI (DPARSF) (Chao-Gan and Yu-Feng, 2010). DPARSF is a user-friendly tool within Data Processing and Analysis for Brain Imaging (DPABI). In this study, it was used for the removal of the effect of the nuisance covariates, the temporal filtering of the data and the extraction of the ROI time-courses.

The pre-processing was performed individually for each subject. The main pre-processing steps included the realignment, slice timing correction, coregistration, segmentation, normalization, smoothing, nuisance covariates regression and temporal filtering (Figure 3.7) described in detail in Part 2.3.3 of

Background.

Primarily, the DICOM file's were converted to NIfTI formats. This NIfTI format includes the affine coordinate system, which transforms the voxel index *(i,j,k)* to spatial location *(x,y,z)* hence giving accurate information about where the left and right hemispheres are. Functional and structural data were converted independently.

The realignment involved the correction of the head motion in all functional volumes considering an algorithm of six parameters (three for translation and three for rotation) that describes the motion of a rigid body.

Furthermore, a slice timing correction was performed aiming the correction of the differences in image acquisition time between slices. For that purpose, the 34 slices for each one of the 150 functional volumes were selected. The ascending order of their acquisition was indicated by including an array going from 1 to 34. Moreover, the reference slice was also defined (as 17 which is the slice acquired at the halfway of the scan in order to reduce timing corrections).

The following step involved the spatial coregistration which aimed to maximize the mutual information between structural and functional images.

Further, a segmentation was applied mainly to separate GM, WM and CSF in anatomical images. Moreover, a deformation field containing the coordinates where the deformation space occurred was also obtained which will be applied for the normalization of the images.

Then, the image data were normalized to the standard MNI space and resampled to $3\times3\times3$ mm^3 which was the voxel size that best fitted the data of this study.

Subsequently, the images were smoothed with an $6\times6\times6$ mm^3 FWHM Gaussian kernel to minimize spatial noise and hence increase the SNR. This choice of was based on the match between the shape and the size of the signal change which should at least be two or three times the voxel dimension.

After smoothing, the effect of the nuisance covariates was removed using the DPARSF software. The Friston 24-parameter model was used to regress out head motion artefacts from the realigned data. The global mean signals, the WM and the CSF signals were also removed to reduce the effects of head motion and non-neural BOLD fluctuations. The residual time-series were band-filtered within a frequency range of 0.01-0.1 Hz to remove the very low- and high-frequency noise.

Lastly, the ROI time-series of the data were extracted, for two automated anatomically labeled (AAL) atlases each of 45 hemispheric-brain regions using the same software (Figure 3.7). The selection of these atlases involved the fact that the this study aimed to compare the lesioned and non lesioned hemispheres for a group of patients, as it will be described in Section 3.3. It should be noted that these regions respected the cerebral regions (Table 3.2). Thus, the individual ROI time-courses encompasses an array of 150 functional volumes across 45 hemispheric-brain regions.

Patient	**Gender**	**Age**	**Pathology**	**Lesion location**
Patient 1	M	59	Tumor	Left frontal lobe
Patient 2	M	50	Tumor	Left paramarginal gyrus
Patient 3	F	27	Cavernous malformation	Left temporal lobe
Patient 4	M	77	Tumor	Left parietal lobe
Patient 5	M	54	Tumor	Left frontal lobe
Patient 6	F	52	Tumor	Left fronto-basal lobule
Patient 7	F	66	Tumor	Left temporal lobe

Table 3.1: Patients' demographic information. M and F respectively mean male and female genders. Age is indicated in years.

3.2 Processing – graph theory analysis

Network analysis was performed in MatLab (The MathWorks Inc., MA, USA version R2016b) and implemented by BRain Analysis using graPH theory (BRAPH 1.0.0) (Mijalkov, Kakarei, Pereira, Westman and Volpe, 2017). However, there are other toolboxes that can also be used for the study of the brain connectivity including the Brain Connectivity Toolbox, GraphVar, GRETNA (GRaph thEoreTical Network Analysis) and MNET (Multimodal brain NETwork Toolbox). These will be briefly described in Subsection 3.2.1.

3.2.1 Brain connectivity toolboxes

The Brain Connectivity Toolbox is a MatLab toolbox for complex-network analysis of structural and functional brain connectivity data sets. In spite of not including a graphical user interface (GUI), its codebase is widely used by brain-imaging researchers to develop GUI or software capable of showing and visualizing the brain network and other results from the graph theory analysis. It has been ported to be, included in, or modified in the following projects: GraphVar, GRETNA, MNET and BRAPH [30].

GraphVar is a GUI-based toolbox for graph theoretical analysis of brain connectivity including the construction, characterization and visualization of the network, statistical analysis on network topological measures and interactive exploration of the results such as plotting group differences and correlations. For the construction of graph networks, the negative weights of the functional connections between brain regions may be transformed into their absolute values, be substituted by zero or left unchanged. Moreover, GraphVar allows the selection of thresholding methods including the application of absolute and proportional thresholds in the networks. Regardless the choice of connectivity correlation and threshold type, both undirected weighted or binary graphs can be created. Further, the connectivity matrix can be obtained and several global and nodal graph metrics calculated. However, it is not an intuitive software which constitutes a disadvantage for this study [41].

A more user-friendly GUI software is GRETNA that allows the resting-state fMRI data pre-processing followed by the construction of the connectivity matrices. In network analysis, it is possible to convert these connectivity matrices into undirected graph networks according to the pre-assigned parameters of the network type (binary or weighted). The connectivity correlation can also be considered as: (1) positive being the network composed by only positive correlations; (2) absolute where the network is composed by the positive correlations and the absolute value of the negative correlations; and (3) negative which relates to a network composed of only absolute negative correlations. Furthermore, GRETNA offers the selection of the threshold type (absolute connectivity strength or density) and range for the construction of the brain graphs. Finally, it allows the calculation of graph-based global and nodal network metrics and the corresponding comparison. A major disadvantage of this software is the exclusion of the network visualization. Additionally, there are few options for the network measures [42].

Unlike GRETNA, the automated network analysis toolbox of MNET allows the network visualization. This toolbox was also developed from Brain Connectivity Toolbox and offers functions for the resting-state fMRI pre-processing, involving the removal of physiological noise, motion effect and the temporal band-pass filtering. The functional connectivity can be analyzed through functional segregation and integration methods such as ALFF and seed-based correlation analysis, respectively. Beyond that, a graph theoretical analysis may also be applied for the network analysis and a correlation matrix created. Nevertheless, only undirected weighted and binary graphs can be obtained. Those can be positive retaining only the positive correlations, negative whose correlation coefficients are set into their corresponding absolute values or both which indicates that the network is composed by positive correlations and the

absolute values of the negative correlations. Besides, there is merely the thresholding method of density available and few nodal and global graph measures can be computed which also constitutes limitations of the MNET. Even so, it allows the visualization of the network, in a two (three) dimensional space as well as the adjacency matrix. Furthermore, the graph measures can be also visualized either in a three-dimensional view or a boxplot. Ultimately, MNET provides various statistical analyses of the results [43].

3.2.2 BRAPH software

Considering all the drawbacks of the software described in the previous Subsection 3.2.1, a new software was developed. BRAPH performs the graph theoretical analysis of the brain connectome with a graphical user interface, carrying out all the steps for the network construction, calculation of the network properties, statistical analysis and visualization of the results.

There is the possibility to obtain undirected binary and weighted brain connectivity graphs starting from data acquired using various neuro-imaging modalities, including EEG, PET, MRI and fMRI.

The graphical user interfaces (GUIs) package of the software provides a streamlined way to carry out graph theory analyses based on a series of GUIs, as displayed in Figure 3.1: (a) the GUI Brain Atlas which allows the selection and edition of the brain atlas; (b) the GUI Cohort which enables the definition of the cohort of subjects by uploading the corresponding data; and (c) the GUI Graph Analysis which builds the connectivity matrices by selecting the type of graph (weighted and binary) [31], connectivity negative correlation (substituted by zero or by their absolute values or left unchanged) and thresholding method (correlation- or density-based thresholds) [36]. Moreover, BRAPH permits the calculation and statistical comparison of both global and nodal network measures as well as visualizing the results.

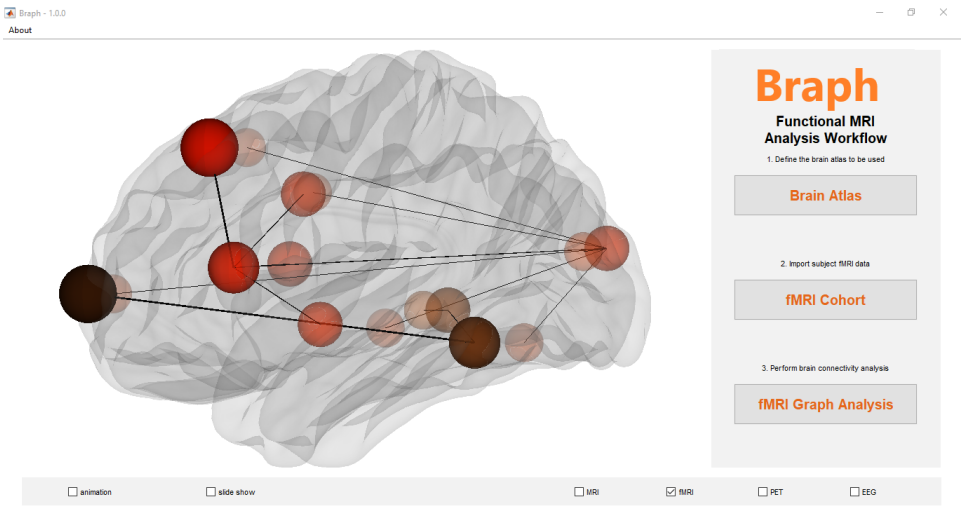

Figure 3.1: Initial GUI that appears when BRAPH is launched. From this GUI, it is possible to choose the neuro-imaging modality (EEG, PET, MRI or fMRI) and to launch the software from the different stages of the workflow: brain atlas, cohort and graph analysis.

Comparing to the other toolboxes, BRAPH is an user-friendly software that, despite not incorporating the resting-state fMRI data pre-processing, it allows the processing of the data using the graph theoretical analysis. It also enables the network visualization. Thereby, it seemed to be a suitable software to be applied in this study. In this context, the BRAPH available functionalities from the definition of an atlas to the computation and visualization of the small-world network properties will be further described.

Defining the nodes

The nodes of the brain network can be defined using different templates including the Desikan, AAL, Craddock and Destrieux atlases. If desirable, the user may also upload a different atlas from an external file or create an entirely new one in the GUI Brain Atlas. Regardless the options, the atlas file should contain the names and labels of the brain regions as well as their spatial coordinates *(x,y,z)* in order to project them onto a three-dimensional surface and create a visual representation of the brain network (Figure 3.2) [31].

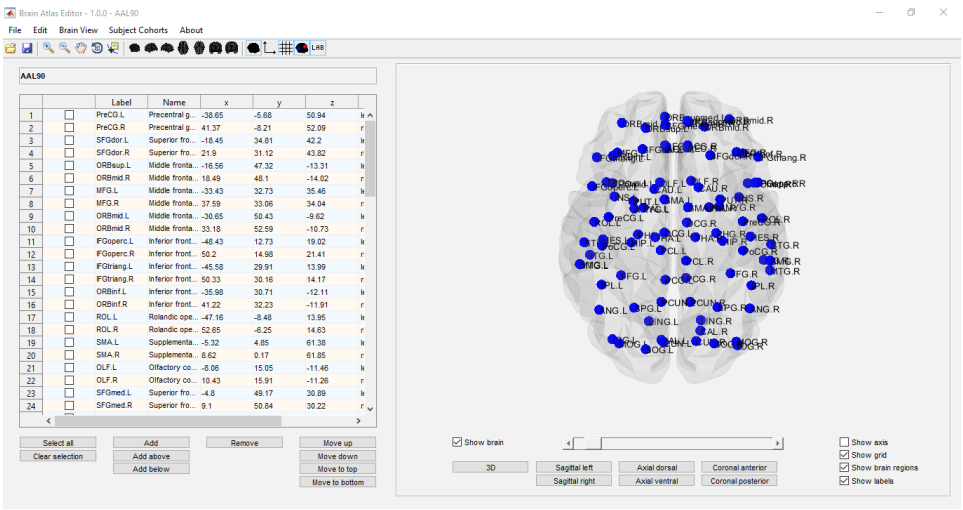

Figure 3.2: GUIBrainAtlas window. It is seen the AAL atlas with 90 cortical and subcortical brain regions.

Then, the subject or the group of subjects data (ROI time-series) are uploaded in the GUI Cohort, as it is shown in Figure 3.3.

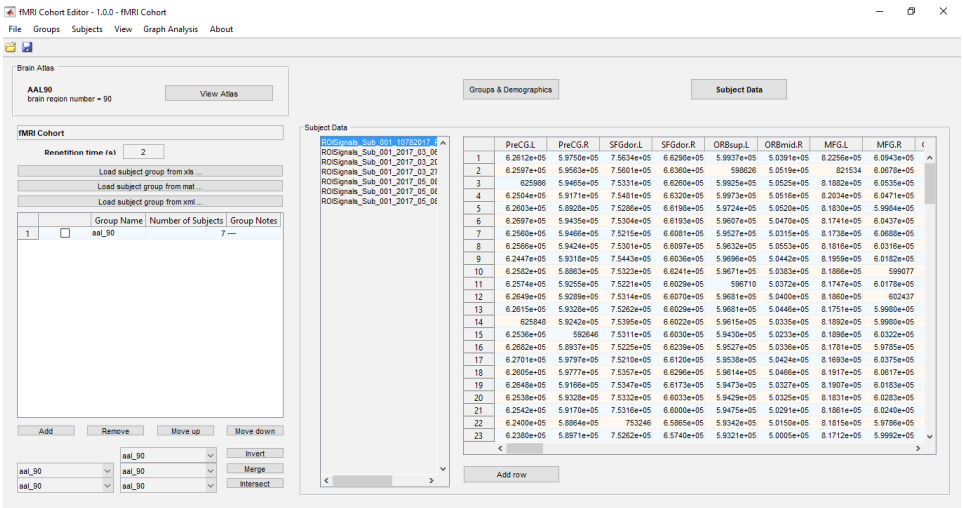

Figure 3.3: GUI fMRI Cohort window. The ROI time-series of a group of 7 patients, in respect to the AAL atlas of 90 brain regions.

Defining the edges

Once the nodes were defined and the ROI time-series uploaded, the edges can be calculated in GUI Graph Analysis as the statistical correlation between the values of all pairs of brain regions. Different

types of correlations may be selected including the Pearson, Spearman, Kendall rank correlation coefficients or (Pearson or Spearman) partial correlation coefficients. Succinctly, the Pearson coefficient assumes the data to be normally distributed and it measures the linear relation between two brain regions. A correlation of 1 denotes a perfect positive linear relation while values of -1 mean a perfect negative linear correlation. The Spearman and Kendall rank correlations are non parametric tests, being the former the non parametric version of Pearson coefficient. It is also possible to select either Pearson or Spearman partial correlation coefficients that establish relationships between two sets of data after removing the influence of one or more variables [31].

Network construction

The following step regards the construction of the correlation matrix involving all possible connections between the regions within each individual subject. The presence and strength of the connections between the labeled brain regions provided by the parcellation template is, then, described in a connectivity matrix. The functional connectivity matrix can be either directed and not symmetric or undirected and symmetric, as explained in Part 2.3.5 of Background. Even though the direct graph measures are not currently used in the analyses performed by BRAPH, they are already available in the *Graph* package and ready to the used in future versions of the software [31]. Furthermore, all self-connections of the functional connectivity matrix can be eliminated from the analysis by setting the diagonal entries to zero. The negative correlations, on one hand, can be included as their absolute or unaltered values. On the other hand, they can be substituted by zero which exclude them from the connectivity matrix [36].

The BRAPH software only requires the selection of these parameters to automatically display the functional connectivity matrices. Their representation can be subject-individual or if applicable as a mean of all subject-individual connectivity matrices resulting in a group correlation matrix (Figure 3.4).

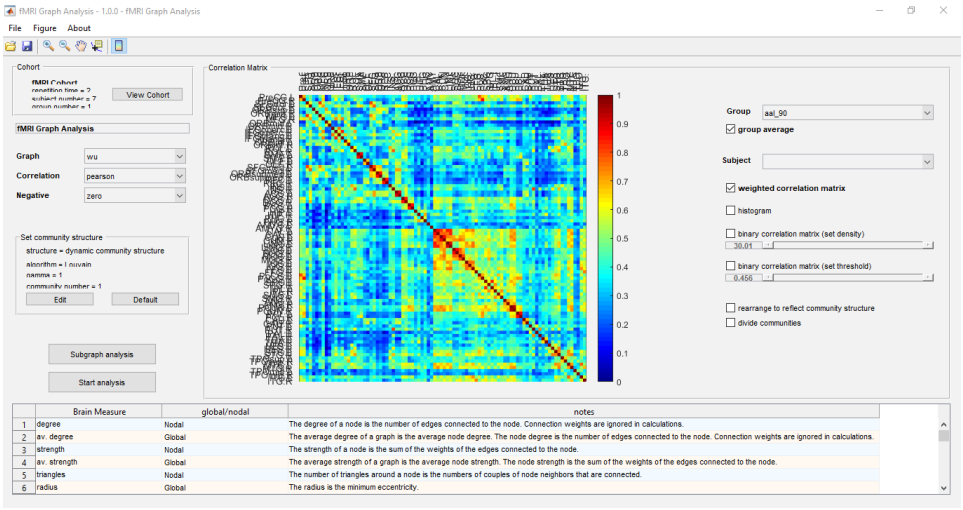

Figure 3.4: GUI fMRI Graph Analysis window. The connectivity matrix as a mean of the connectivity matrices of a group of 7 subjects. In the right side, there is a scale of the correlation coefficients between the processed time-series of the brain regions, represented by colors. Moreover, individual representations of the connectivity matrices can also be chosen. In the left side, the options to select the type of graph (weighted undirected (wu)), correlation (pearson), conversion of the negative values (zero) and the community structure (set as default) are indicated.

Thresholded binarized adjacency matrices can be constructed where the edges can be either 0 (absence of connection) or 1 (presence of connection). The thresholding methods rely on absolute or proportional thresholds. Analogous to the weighted connectivity matrices, the binary matrices can be either

directed or undirected; nevertheless, the current version of BRAPH only allows the use of binary undirected graphs.

The selection of the threshold is intuitive and enables an automatic display of the undirected binary thresholded matrices (Figure 3.5).

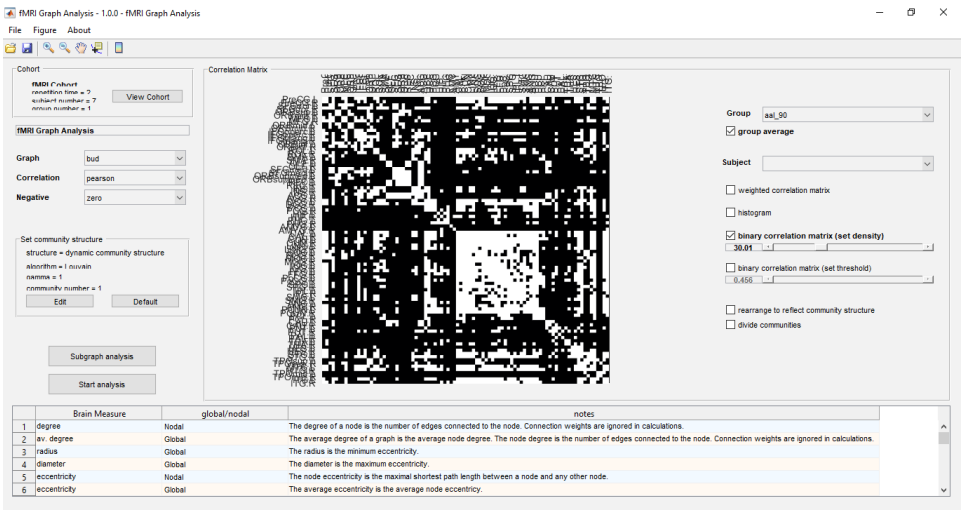

Figure 3.5: GUI fMRI Graph Analysis window. The binary matrix as a mean for the group of 7 subjects. In the right side, individual representations of binary matrices can be chosen. Below, the two options to threshold these binary matrices involve the absolute or proportional (density) thresholds. The displayed binary matrix was thresholded by a density of 30%. The white and black entries respectively indicate the presence and absence of a connection between the two brain regions. In the left side, the options to select the type of graph (binary undirected density (bud)), correlation (pearson), conversion of the negative values (zero) and the community structure (set as default) are indicated.

Network properties

Besides the construction of the networks, the GUI Graph Analysis also allows for the calculation of the topological network properties. The BRAPH includes a wide list of graph measures that can be calculated including the ones explored in Subsection 2.3.5 of Background. Furthermore, BRAPH provides the option for the comparison of those network properties with random graphs or between two (previously selected) groups by permutation tests. The networks measures and the comparison results can further be represented in a graphic (Figures 3.6a and 3.6b) and a brain-view representation (Figure 3.6d); however, this latter is only possible for the nodal measures. The functional connections between the brain regions can also be displayed and associated with the nodal measures in the brain-view. These connections can also be thresholded in the same way as the thresholding methods for binary graphs (Figure 3.6c).

(a) **Global measures**

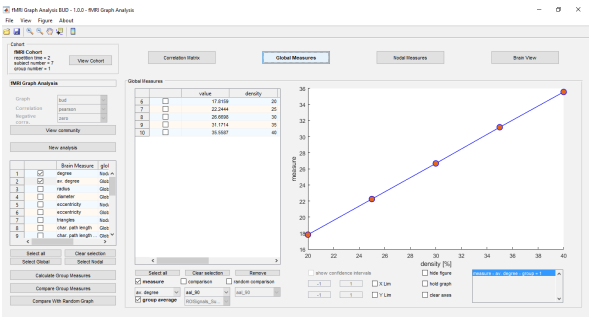

(b) **Nodal measures**

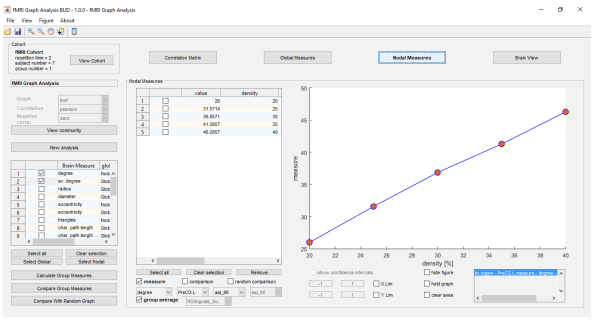

(c) **Brain view - graph**

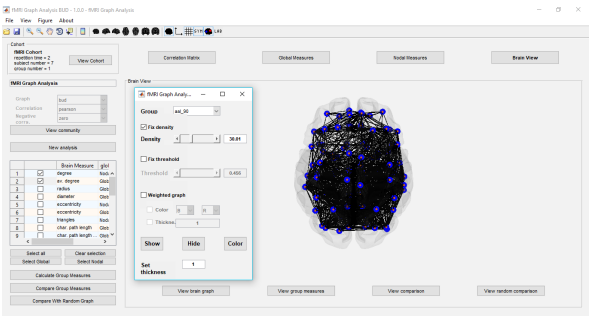

(d) **Brain view - nodal measures**

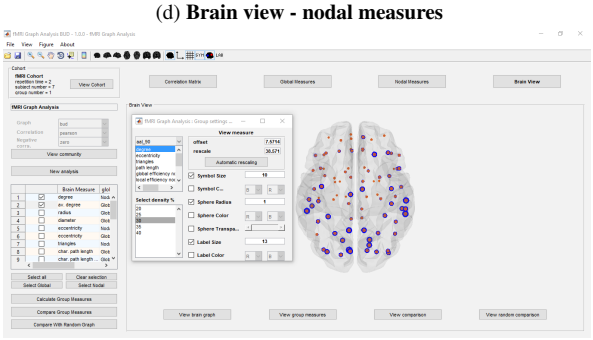

Figure 3.6: Graphic and brain-view representations of global and nodal graph theory measure of degree in GUI Graph Analysis, calculated for a group of 7 patients: (a) global degree; (b) nodal degree; (c) brain-view of the graph whose functional connections were thresholded at density of 30%; and (d) brain-view of the nodal degree calculated at density of 30%.

3.3 Methodology

In this study, the goal is to compare the lesioned and non lesioned hemispheres from the resting-state fMRI data acquired for a group of 7 patients with tumors and a cavernous malformation. Graph theory analysis was applied, resorting to the functionalities of BRAPH described in the previous Subsection 3.2.2, in order to calculate the topological measures for each network corresponding to the lesioned and non lesioned hemispheres.

As explained in Section 3.1, the first step of this analysis was to pre-process the resting-state fMRI data using the SPM12 and DPARSF software and applying the following procedures: realignment, slice timing correction, coregistration, segmentation, normalization, smoothing, nuisance signals removal and temporal filtering. Moreover, the ROI time-courses were extracted for each of the AAL 45 hemispheric-brain regions (Figure 3.7).

Further, the functional connectivity matrices for each network were obtained in BRAPH. Thereunto, the selection of an atlas were required. The nodes were defined using the AAL template images of 90 ROIs of the cerebral cortex (Table 3.2). However, since the aim is to evaluate the lesioned and non lesioned hemispheres, those 90 regions of the whole cerebral cortex were equally divided into two sides corresponding to the left and right hemispheres with respectively 45 hemispheric regions. Thus, in GUI Brain Atlas, two brain atlases were uploaded.

Once the atlas were defined, two groups were created according to the lesion's location of the 7 subjects: the hemisphere where the lesion is located and the contralateral one. Therefore, the ROI time-courses of all patients respecting the hemisphere where the lesion was identified were set in the same group named as the lesioned group. The remaining ROI time-courses, that correspond to the time series of the regions located in the hemisphere without a lesion, formed the non lesioned group. Further, each group was uploaded in the GUI Cohort.

The undirected weighted connectivity matrices could then be computed, for each hemisphere in the GUI Graph Analysis. Considering the distribution of the data as normal, the selection of the Pearson correlation coefficient was valid and suitable. Furthermore, the self-connections were removed and the negative correlations were considered as zero. Since the goal of this study was to perform between-groups comparisons, the option for a group average of the individual connectivity matrices was selected leading to the representation of two connectivity matrices respectively corresponding to lesioned and non lesioned groups. Besides, thresholded binarized matrices were obtained by applying a range of proportional thresholds. A large range of proportional thresholds have been applied, from 5%-40%, depending its choice on the ongoing research [44]. In this study, proportional thresholds from 20% to 40% with increments of 5% were applied in the both lesioned and non lesioned binary undirected matrices. As for the previous functional connectivity matrices, the five thresholded binary matrices were represented as a group average corresponding to the lesioned and non lesioned groups.

For each thresholded lesioned and non lesioned networks, their topological parameters were computed through the calculation of the graph metrics described in Part 2.3.5 of Background (Figure 3.7). Consequently, while the integration property of the network can be concluded according to the measures of characteristic path length and global efficiency, the segregation is inferred through the clustering coefficient and local efficiency metrics. Accounting for both integration and segregation characteristics, the small-world property of both networks was determined through the calculation of the small-worldness.

In Section 3.4 the statistical analysis for these graph measures that was proceeded is reported with a purpose of disclosing the significant differences between hemispheres and the dependence of the small-world topological properties on the applied threshold (Figure 3.7).

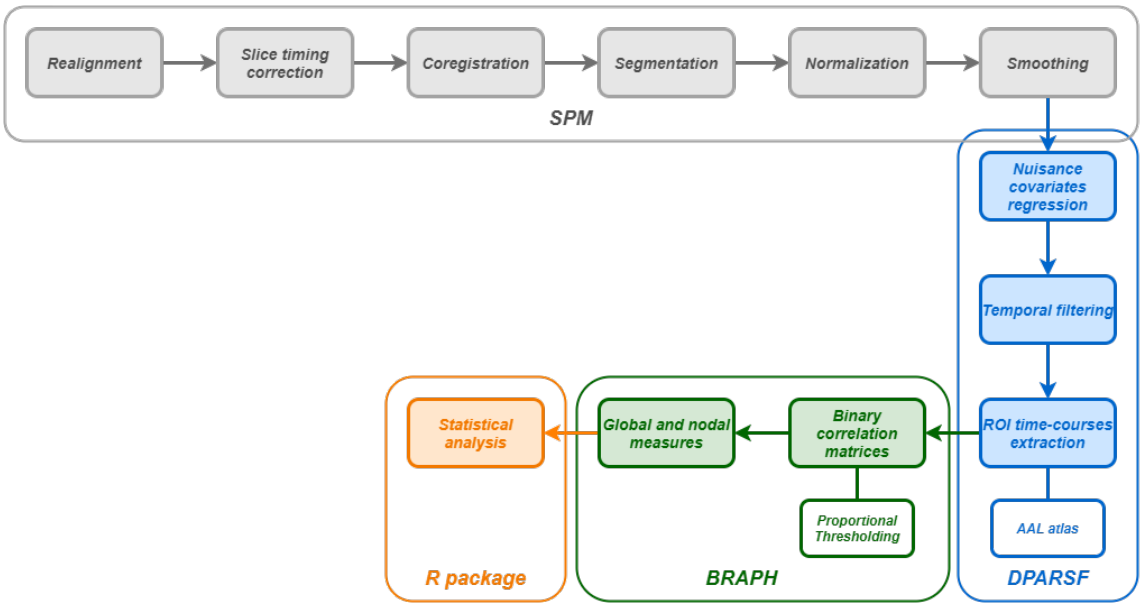

Figure 3.7: Methods for the resting-state fMRI data analysis. Grey and blue boxes correspond to the pre-processing of the data using, respectively, the mentioned steps in SPM and DPARSF software. The green box represents the graph theory analysis with BRAPH; and the orange box the statistical analysis of the BRAPH extracted results. The white box outlined in blue indicates the extraction of ROI time-courses resorting to the modified AAL atlas. The white box outlined in green signifies that the binary correlation matrices were thresholded by proportional thresholds.

Location	Regions	Abbreviations
Frontal	Superior frontal gyrus, dorsolateral	SFGdor
	Superior frontal gyrus, orbital	ORBsup
	Middle frontal gyrus	MFG
	Middle frontal gyrus, orbital	ORBmid
	Inferior frontal gyrus, opercular	IFGoperc
	Inferior frontal gyrus, triangular	IFGtriang
	Inferior frontal gyrus, orbital	ORBinf
	Superior frontal gyrus, medial	SFGmed
	Superior frontal gyrus, medial orbital	ORBsupmed
	Gyrus rectus	REC
	Anterior cingulate gyrus	ACG
Parietal-(pre)motor	Precentral gyrus	PreCG
	Supplementary motor area	SMA
	Median- and para-cingulate gyrus	DCG
	Posterior cingulate gyrus	PCG
	Postcentral gyrus	PoCG
	Superior parietal gyrus	SPG
	Inferior parietal gyrus	IPL
	Supramarginal gyrus	SMG
	Angular gyrus	ANG
	Precuneus	PCUN
	Paracentral lobule	PCL
Temporal	Insula	INS
	Rolandic operculum	ROL
	Heschl gyrus	HES
	Superior temporal gyrus	STG
	Middle temporal gyrus	MTG
	Inferior temporal gyrus	ITG
Medial temporal	Hippocampus	HIP
	Parahippocampal gyrus	PHG
	Amygdala	AMYG
	Superior temporal gyrus, temporal pole	TPOsup
	Middle temporal gyrus, temporal pole	TPOmid
Subcortical	Olfactory cortex	OLF
	Caudaute nucleus	CAU
	Lenticular nucleus, putamen	PUT
	Lenticular nucleus, pallidum	PAL
	Thalamus	THA
Occipital	Calcarine fissure and surrounding cortex	CAL
	Cuneus	CUN
	Lingual gyrus	LING
	Superior occipital gyrus	SOG
	Middle occipital gyrus	MOG
	Inferior occipital gyrus	IOG
	Fusiform gyrus	FFG

Table 3.2: Cortical and subcortical regions defined by the AAL atlas.

3.4 Statistical analysis

The statistical analysis of the graph metrics calculated for both lesioned and non lesioned networks thresholded at different levels aimed to compare the topological networks properties of both hemispheres and establish a relationship between them and the selected threshold. The BRAPH merely allows the computation of a comparison between the two uploaded groups which precludes its use for the between-threshold comparison. In this context, the statistical analysis of this study was performed with the R statistical package (R version 3.6.1.) (developed by members of the R Development Core Team).

The purpose was to compare the differences in the graph measures between the five proportional thresholds as well as the lesioned and non lesioned hemispheres. Since the data of both lesioned and non lesioned hemispheres regarded the same patients, the comparison between thresholds and hemispheres resorted on tests that compare paired groups. Their suitable selection required testing the normality nature of the data distribution. The Shapiro's-Wilk test is the most widely recommended test because it provides the better power being for medium or small samples ($n \leq 50$) [45]. Therefore, this test was applied before the between- threshold and hemispheres comparisons. The output of the Shapiro's-Wilk test revealed the normality nature of the data distribution if the obtained P value was higher than 0.05*. On the other hand, for P value lower than or equal to 0.05 the distribution of the data was considered as significantly different from the normal distribution.

Once the normality was tested, different statistical tests could be applied in order to compare the global and nodal graph metrics obtained when the lesioned and non lesioned networks were thresholded at different densities, as it is explained in Subsections 3.4.1 and 3.4.2.

3.4.1 Comparison of graph metrics between proportional thresholds, for each hemisphere

The graph measures were computed for lesioned and non lesioned networks thresholded at a range of proportional thresholds from 20% to 40%, at steps of 5%. For the between-threshold comparison, the lesioned and non lesioned groups, containing the data of network measures calculated for each threshold, were analysed.

Testing the normality nature of the data involved the evaluation of whether the distribution of the data from pairs of densities followed a normal distribution. The assumption of no outliers was considered due to the fact that the small number of subjects that participated in this study could make the between-threshold comparison unfeasible.

Considering the normality results and the previous assumption, if the distribution of the data was not significantly different from a normal distribution, the two-sample paired t test could be applied testing whether there were statistical differences in graph metrics between the pairs of thresholds in terms of their mean values. This selection was suitable due to the single evaluation of two samples (pairs of densities). Nevertheless, if the normality distribution of the data was not verified, different tests were required such as the Wilcoxon matched pairs test (Figure 3.8). Succinctly, this non normal test can be understood as a test for median differences, unlike the previous normal test [46].

*The significance level as 5% was considered in this statistical analysis.

3.4.2 Comparison of graph metrics between lesioned and non lesioned hemispheres, for each proportional threshold

For the between-hemispheres comparison, five groups corresponding to the five proportional thresholds were analysed comprising the graph measures calculated for both lesioned and non lesioned networks.

The selection of the suitable comparison test was accomplished through the evaluation of the normality nature of the data distribution from lesioned and non lesioned groups. For the distributions that were not significantly different from a normal distribution, the two-sample paired *t* test could be used because only two samples (lesioned and non lesioned networks) were being compared. This application was also feasible due to the assumption of no outliers in the groups [47]. In contrary, the Wilcoxon matched pairs test was applied when the normal distribution of the data was not verified (Figure 3.8). The application of the Wilcoxon matched pairs test compared the median values, rather than the mean values as the two-sample paired *t* test, as described in the previous Subsection 3.4.1.

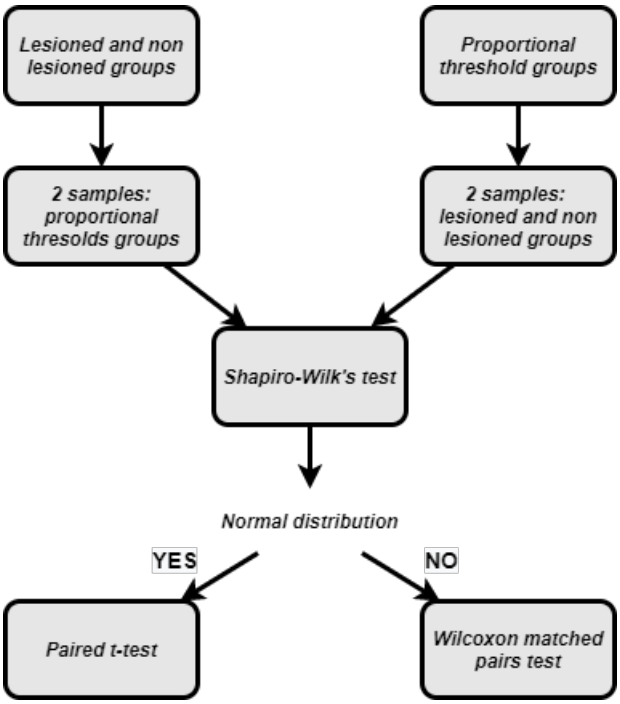

Figure 3.8: Processes of the statistical analysis for the between- proportional threshold and hemispheres comparisons.

Chapter 4

Results

This chapter aims to exhibit the results from the processing analysis (graph theoretical analysis) and the corresponding statistical outcomes. In the processing stage, the results respecting the global graph measures can be easily reported. In contrary, due to the large amount of nodal data (45 hemispheric brain regions), the nodal results will be shown in Appendix A. Furthermore, the code developed in the R statistical package to perform the statistical analysis will be displayed in Appendix B.

4.1 Graph theory analysis

The resting-state fMRI data acquired were pre-processed as detailed explained in Subsection 3.1 of Methods. The Figure 4.1 shows the most significant pre-processing analysis steps and outcomes, for patient 1. The extracted ROI time-courses were processed, using BRAPH and according to the methodology described in Section 3.3 of Methods.

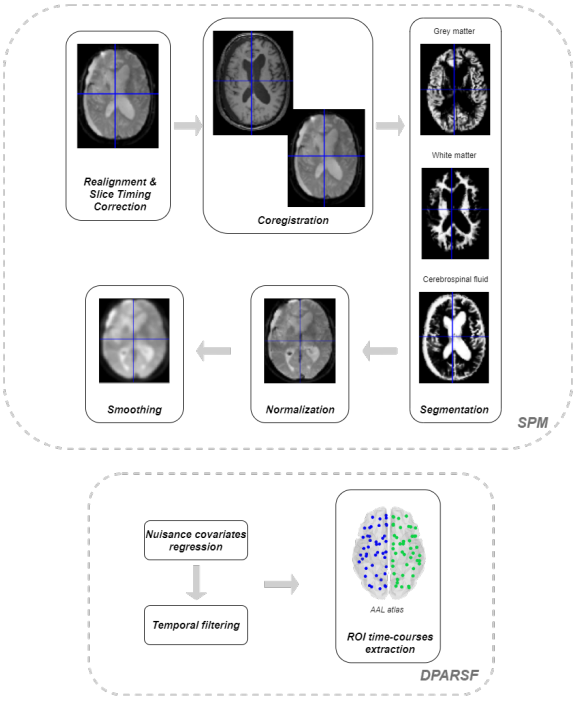

Figure 4.1: Overview of the resting-state fMRI pre-processing analytic strategy. First, functional images were realigned, slice timing corrected, coregistered, segmented, normalized and smoothed using the SPM12 software. Then, using the DPARSF program, a regression of the nuisance covariates and a temporal filtering of 0.01-0.1 Hz was employed in the data. Lastly, the residual ROI time-courses were extracted for the AAL atlas of 45 hemispheric-brain regions.

4.1.1 Construction of thresholded binary correlation matrices

The graph theory analysis involved the construction of the functional connectivity matrices of the lesioned and non lesioned networks, followed by the computation of their topological properties. The Figures 4.2a and 4.2b represent the weighted connectivity matrices of lesioned and non lesioned networks, respectively.

(a) **Lesioned**

(b) **Non lesioned**

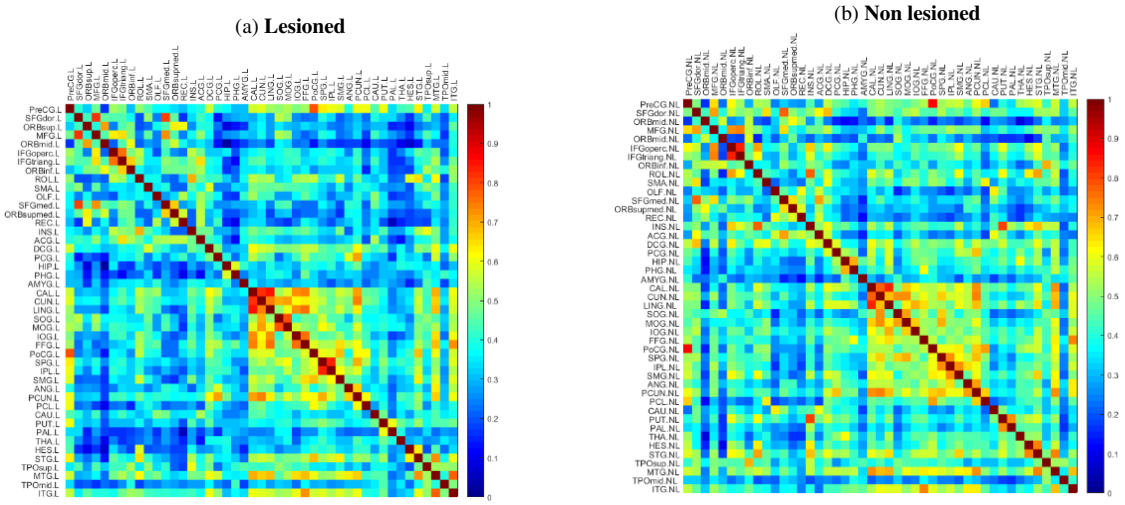

Figure 4.2: Functional connectivity matrices for lesioned (left) and non lesioned (right) hemispheres, averaged for the group of 7 patients. A scale of the correlation coefficients between the processed time-series in all 45 hemispheric-brain regions, represented by colors, is located on the right side of each matrix.

Further, the thresholded binary undirected matrices were constructed through the application of a range of proportional thresholds between 20% and 40%, with increments of 5%. The obtained thresholded binary matrices for both lesioned and non lesioned hemispheres are displayed in Figures 4.3 and 4.4.

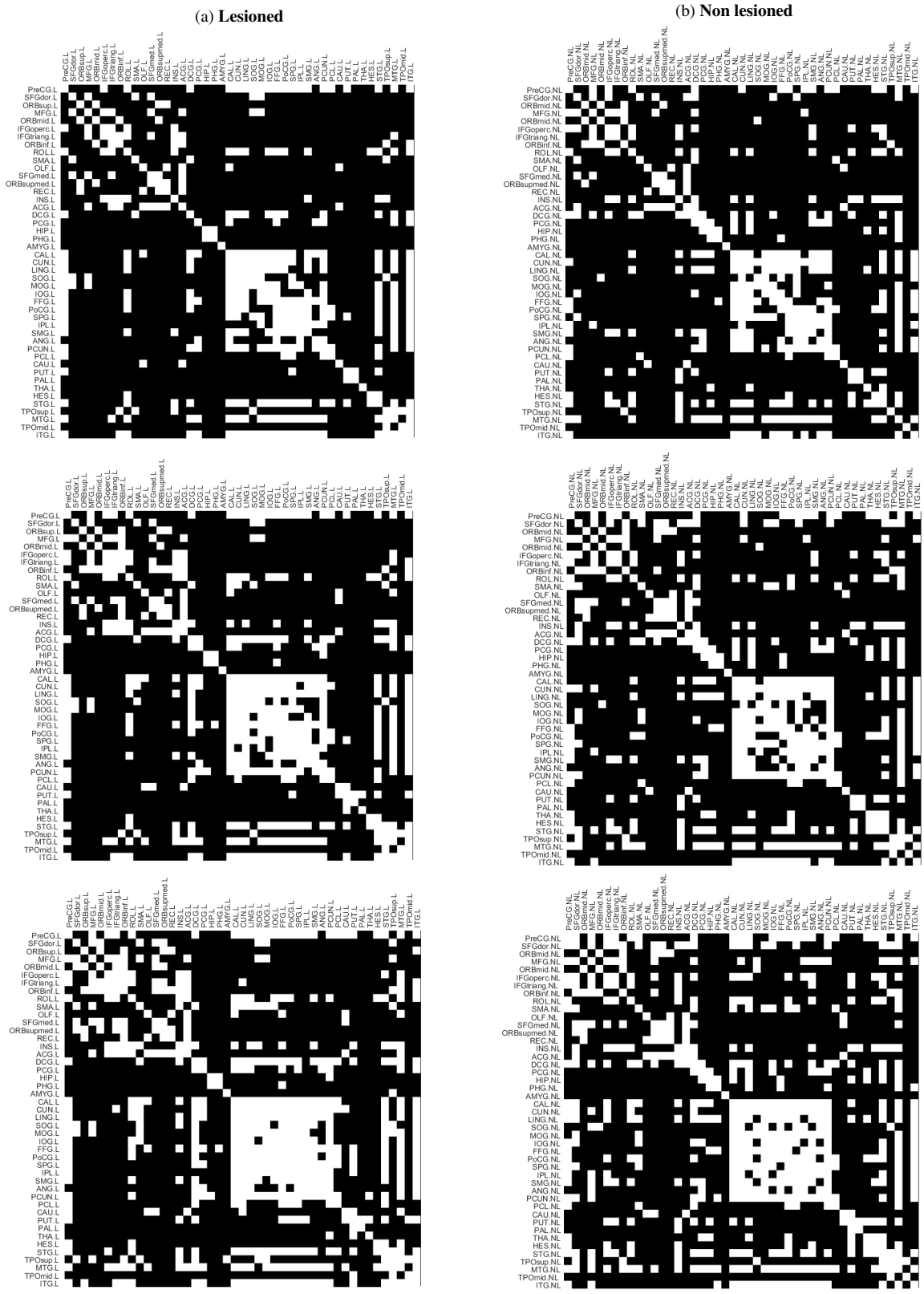

Figure 4.3: Binarized undirected matrices thresholded at densities of of 20%, 25% and 30%. The functional connectivity matrices for lesioned and non lesioned hemispheric groups were thresholded by density values of 20% (top), 25% (middle) and 30% (bottom) to construct thesholded binary undirected matrices for, respectively, lesioned (left) and non lesioned (right) hemispheres. The white and black entries represent, respectively the presence and absence of a correlation between the 45 labeled hemispheric-brain regions.

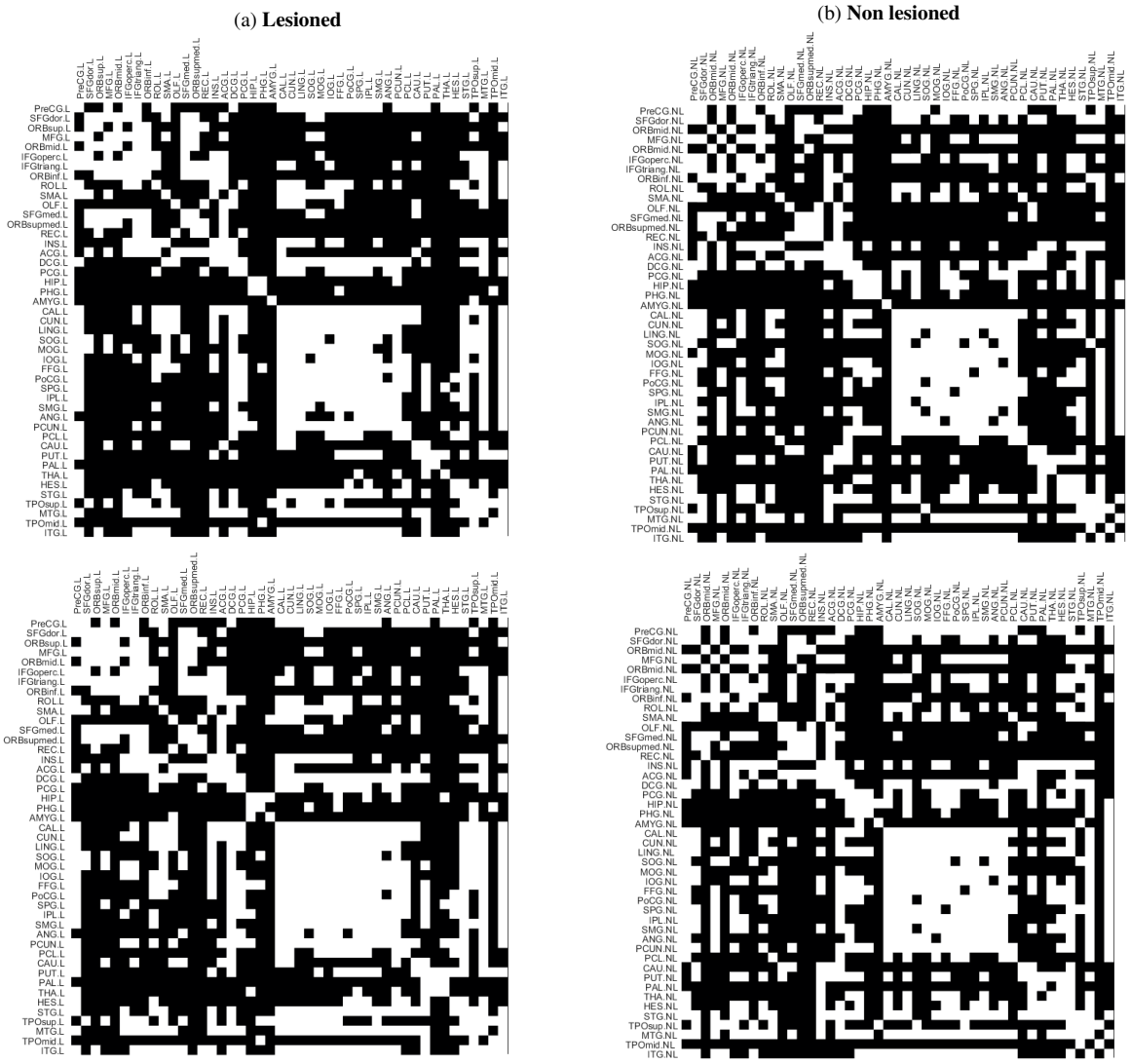

Figure 4.4: Binarized undirected matrices thresholded at densities of 35% and 40%. The functional connectivity matrices for lesioned and non lesioned hemispheric groups were thresholded by density values of 35% (top) and 40% (bottom) to construct thesholded binary undirected matrices for, respectively, lesioned (left) and non lesioned (right) hemispheres. The white and black entries represent, respectively the presence and absence of a correlation between the 45 labeled hemispheric-brain regions.

4.1.2 Calculation of graph metrics

From the computation of the thresholded binary matrices of both lesioned and non lesioned networks, several nodal and global graph metrics of integration and segregation network properties were calculated. The integration and segregation metrics were described in Part 2.3.5 of Background. The mean and median values of the global measures are respectively summarized in Tables 4.1 and 4.2. In contrast, the nodal metrics are displayed in Appendix A. The mean and median nodal global efficiency are respectively shown in Tables A.1 and A.2, while the mean and median values of the nodal clustering coefficient are shown in Tables A.3 and A.4, respectively. Furthermore, the mean nodal measures of global efficiency and clustering coefficient were represented for each one of the 45 hemispheric regions in a brain distribution, using the BrainView functionality of GUI Graph Analysis. These representations are displayed in Figures A.1 and A.2 for the nodal global efficiency and in Figures A.3 and A.4 for the nodal clustering coefficient.

Since the statistical comparisons of the graph measures between lesioned and non lesioned hemi-

spheres, for each threshold and between the different thresholds, for each hemisphere were computed in R statistical package, this software was ended up used for global representations. In Figure 4.5 the global metrics are represented according to their mean values indicated in Table 4.1.

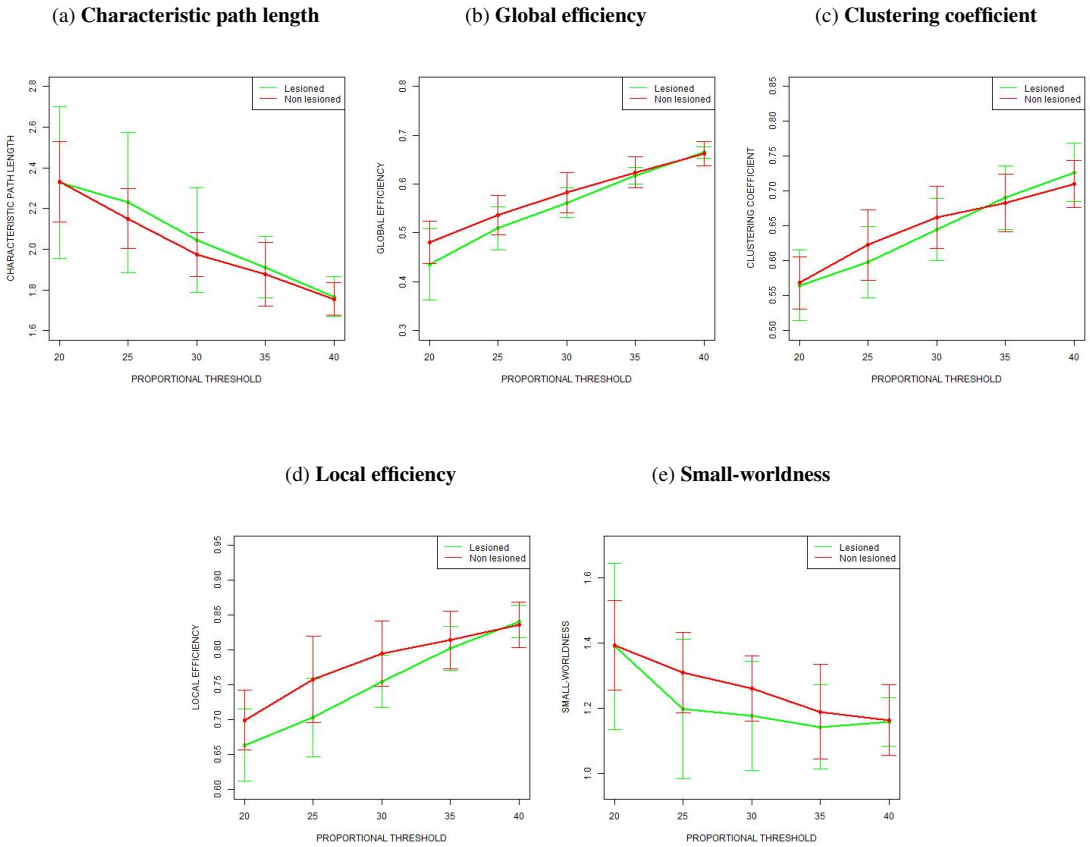

Figure 4.5: Global network properties obtained for lesioned (green line) and non lesioned (red line) networks at each proportional threshold in the range of 20%-40% with increments of 5% and their standard deviation including the (a) characteristic path length, (b) global efficiency, (c) clustering coefficient, (d) local efficiency and (e) small-worldness. Data are represented as mean values. The vertical bars indicate the standard deviation across subjects for the lesioned (green) and non lesioned (red) networks.

Hemispheres	Metrics	Proportional threshold				
		20%	**25%**	**30%**	**35%**	**40%**
Lesioned	L	2.328±0.373	2.229±0.345	2.044±0.256	1.912±0.150	1.766±0.099
	E_g	0.436±0.073	0.510±0.044	0.562±0.030	0.617±0.017	0.665±0.011
	C	0.565±0.050	0.598±0.051	0.645±0.045	0.691±0.046	0.727±0.042
	E_{loc}	0.664±0.052	0.703±0.056	0.755±0.038	0.803±0.031	0.841±0.023
	SW	1.390±0.256	1.198±0.214	1.176±0.167	1.142±0.129	1.157±0.075
Non lesioned	L	2.332±0.199	2.150±0.148	1.975±0.108	1.877±0.158	1.755±0.079
	E_g	0.480±0.044	0.536±0.040	0.582±0.041	0.624±0.031	0.662±0.025
	C	0.569±0.038	0.623±0.050	0.662±0.045	0.683±0.041	0.710±0.034
	E_{loc}	0.700±0.043	0.758±0.062	0.795±0.047	0.815±0.042	0.836±0.032
	SW	1.392±0.138	1.310±0.123	1.261±0.101	1.189±0.145	1.163±0.108

Table 4.1: Mean values of the global metrics, including the characteristic path length (L), global efficiency (E_g), clustering coefficient (C), local efficiency (E_{loc}) and small-worldness (SW) metrics obtained for both lesioned and non lesioned hemispheres whose networks were thresholded at a range of proportional threshold from 20% to 40% with increments of 5%. Data are presented as mean±standard deviation.

Hemispheres	Metrics	Proportional threshold				
		20%	**25%**	**30%**	**35%**	**40%**
Lesioned	L	2.317	2.090	1.937	1.880	1.751
	E_g	0.467	0.527	0.574	0.621	0.665
	C	0.574	0.591	0.653	0.684	0.730
	E_{loc}	0.644	0.683	0.747	0.800	0.843
	SW	1.422	1.263	1.222	1.147	1.189
Non lesioned	L	2.314	2.136	1.943	1.815	1.720
	E_g	0.486	0.542	0.586	0.629	0.666
	C	0.590	0.622	0.681	0.685	0.703
	E_{loc}	0.715	0.761	0.801	0.830	0.841
	SW	1.396	1.322	1.280	1.226	1.209

Table 4.2: Median values of the global metrics, including the characteristic path length (L), global efficiency (E_g), clustering coefficient (C), local efficiency (E_{loc}) and small-worldness (SW) metrics obtained for both lesioned and non lesioned hemispheres whose networks were thresholded at a range of proportional threshold from 20% to 40% with increments of 5%.

4.2 Statistical analysis

This section aims to display the results from the statistical analysis of the graph metrics reported in the previous Section 4.1.2, for both lesioned and non lesioned networks. As for the nodal graph metrics, the nodal statistical results are presented in Appendix A, while the global ones are shown in this section.

The normality nature of the results was tested according to the further comparisons as explored in Subsections 3.4.1 and 3.4.2 of Methods.

4.2.1 Comparison of graph metrics between proportional thresholds, for each hemisphere

The results from the normality testing are shown in Table 4.3. For the nodal metrics, the normality results for the nodal global efficiency are shown in Tables A.5 and A.6, respectively for lesioned and non lesioned hemispheres. Moreover, Tables A.9 and A.10 correspond to the results from the normality testing for the nodal clustering coefficient, respectively for the lesioned and non lesioned hemispheres. These nodal results are shown in Subsection A.2.1 of Appendix A.

Hemispheres	Metrics	Proportional threshold			
		20%-25%	**25%-30%**	**30%-35%**	**35%-40%**
Lesioned	L	6.318E-04*	0.480	0.873	0.997
	E_g	0.088	0.147	0.264	0.826
	C	0.560	0.069	0.893	0.512
	E_{loc}	0.688	0.242	0.839	0.072
	SW	6.415E-04*	0.381	0.241	0.009*
Non lesioned	L	0.138	0.679	0.006*	0.427
	E_g	0.933	0.002*	0.005*	0.383
	C	0.178	0.969	0.927	0.007*
	E_{loc}	0.347	0.698	0.133	0.023*
	SW	0.469	0.681	0.032*	0.475

Table 4.3: Results from the normality tests for the between-threshold comparison of the global metrics, for lesioned and non lesioned hemispheres, including the characteristic path length (L), global efficiency (E_g), clustering coefficient (C), local efficiency (E_{loc}) and small-worldness (SW). The values refer to the P value obtained from the application of Shapiro-Wilk's test. * indicates P value < 0.05 which represents statistical significance.

Depending on the normality results, different statistical tests were applied. The options involved the two-sample paired *t* test or the Wilcoxon matched pairs test, as explained in Subsection 3.4.1 of Methods. The selection of the suitable test as well as the results from this between-threshold comparison is indicated in Table 4.4, for the global results. The results of the nodal global efficiency for lesioned and non lesioned hemispheres are respectively displayed in Tables A.7 and A.8. In addition, the results of nodal clustering coefficient are shown in Tables A.11 and A.12 also for the lesioned and non lesioned hemispheres, respectively.

		Proportional threshold							
		20%-25%		**25%-30%**		**30%-35%**		**35%-40%**	
Hemispheres	**Metrics**	**Test**	***p***	**Test**	***p***	**Test**	***p***	**Test**	***p***
Lesioned	L	W	0.527	t	0.010*	t	0.384	t	0.010*
	E_g	t	0.002*	t	2.200E-04*	t	2.280E-04*	t	1.500E-04*
	C	t	0.003*	t	0.005*	t	0.004*	t	5.500E-04*
	E_{loc}	t	0.004*	t	0.007*	t	0.004*	t	0.002*
	SW	W	0.340	t	0.650	t	0.470	t	0.650
Non lesioned	L	t	0.004*	t	0.001*	W	0.068	t	0.028*
	E_g	t	6.400E-06*	W	1.500E-06*	W	2.000E-04*	t	1.200E-05*
	C	t	0.002*	t	0.007*	t	0.003*	W	0.006*
	E_{loc}	W	5.900E-05*	t	0.005*	t	5.900E-05*	W	2.500E-05*
	SW	t	0.150	t	0.212	W	0.037*	t	0.453

Table 4.4: Results from the comparison of global metrics between the proportional thresholds of 20%-25%, 25%-30%, 30%-35% and 35%-40%, for lesioned and non lesioned hemispheres, including the characteristic path length (L), global efficiency (E_g), clustering coefficient (C), local efficiency (E_{loc}) and small-worldness (SW) metrics. *p* refer to the *P* value obtained from the application of two-sample paired *t* test and Wilcoxon matched pairs test, respectively represented as *t* and *W*. * indicates *P* value < 0.05 which represents statistical significance.

4.2.2 Comparison of graph metrics between lesioned and non lesioned hemispheres, for each proportional threshold

As described in Subsection 3.4.2 of Methods, the comparison between hemispheres also resorted on either Wilcoxon matched pairs or two-sample paired *t* tests, for both global and nodal measures. The criteria for this selection was based on the results of the normality test. Those are shown in Table 4.5 for the global metrics, while the nodal results from the normality testing are displayed in Tables A.13 and A.15 respectively for global efficiency and clustering coefficient, in Subsection of A.2.2 of Appendix A.

	Proportional threshold				
Metrics	**20%**	**25%**	**30%**	**35%**	**40%**
L	0.907	0.485	0.488	0.504	0.727
E_g	0.839	0.915	0.208	0.031*	0.096
C	0.892	0.458	0.136	0.620	0.604
E_{loc}	0.402	0.660	0.451	0.023*	0.149
SW	0.319	0.750	0.967	0.666	0.605

Table 4.5: Results from the normality test for the between-hemispheres comparison of the global metrics, including the characteristic path length (L), global efficiency (E_g), clustering coefficient (C), local efficiency (E_{loc}) and small-worldness (SW), for the proportional thresholds of 20%, 25%, 30%, 35% and 40%. The values refer to the *P* value obtained from the application of Shapiro-Wilk's test. * indicates *P* value < 0.05 which represents statistical significance.

Furthermore, Table 4.6 shows the suitable test to be applied for the between-hemispheres comparison of the global network measures according to the previous results from Table 4.5. Concerning the nodal measures, the results are expressed in Table A.14, for the global efficiency, while for the clustering coefficient, they are presented in Table A.16.

	Proportional threshold									
	20%		**25%**		**30%**		**35%**		**40%**	
Metrics	**Test**	***p***	**Test**	***p***	**Test**	***p***	**Test**	***p***	**Test**	***p***
L	t	0.983	t	0.600	t	0.688	t	0.938	t	0.820
E_g	t	0.158	t	0.230	t	0.260	W	0.569	t	0.748
C	t	0.871	t	0.429	t	0.327	t	0.626	t	0.205
E_{loc}	t	0.297	t	0.195	t	0.137	W	0.585	t	0.760
SW	t	0.986	t	0.327	t	0.290	t	0.507	t	0.914

Table 4.6: Results from the comparison of global metrics between lesioned and non lesioned hemispheres, for each proportional threshold, from 20% to 40% with increments of 5%, including the characteristic path length (L), global efficiency (E_g), clustering coefficient (C), local efficiency (E_{loc}) and small-worldness (SW) metrics. p refer to the P value obtained from the application of Wilcoxon matched pairs or two-sample paired t tests, respectively represented as W and t.

Chapter 5

Discussion

This section intends to analyse the results of both global and nodal graph measures and establish a relationship between them, the proportional thresholds and the hemispheric location of the lesion. Furthermore, this chapter aims to compare the results of this study to the findings from previous studies concluding about the relevance of them in a pre-surgical environment.

5.1 Comparison of graph metrics between proportional thresholds, for each hemisphere

In this section, it is intended to discuss the influence of thresholding both lesioned and non lesioned networks in the topological network properties at different levels. As expected the increase of the threshold promoted more connections to presented in both lesioned and non lesioned networks (Figures 4.3 and 4.4). Both networks will be characterized in terms of their integration through the analysis of the characteristic path length and global efficiency metrics. On the other hand, the clustering coefficient and local efficiency network graph measures will be examined in order to describe the segregation properties of the network. Lastly, the small-world topology of the networks will be discussed and associated to the previous findings of the integration and segregation of the networks.

5.1.1 Characteristic path length

From the statistical tests of between-threshold differences distinct results were obtained. For the lesioned hemisphere, the normality test for the pair of densities of 20%-25% indicated that the distribution of the data was significantly different from the normal distribution (p = 6.318E-04). Thus, the Wilcoxon matched pairs test was applied for the comparison of the characteristic path length between those densities. This comparison resorted on the characteristic path length median values (Table 4.3). For, the remaining pairs of densities, the normality nature of the corresponding data was verified: 25%-30% (p = 0.480), 30%-35% (p = 0.873) and 35%-40% (p = 0.997). Further comparison between these thresholded were based on the mean values due to the application of the two-sample t test. Concerning the non lesioned hemisphere, only the data distribution evaluated for the densities of 30% and 35% significantly differ from the normal distribution (p = 0.006). Consequently, the Wilcoxon matched pairs test was applied for the further comparison of the characteristic path length between these thresholds. As opposite, the distribution of the data for the remaining pairs of densities followed a normal distribution: 20%-25% (p = 0.138), 25%-30% (p = 0.679) and 35%-40% (p = 0.427). The further between-threshold

comparisons respecting these pairs of densities resorted on the two-sample *t* test and hence evaluated the differences in the mean values.

The corresponding results were shown in Table 4.4. For the lesioned hemisphere, significant differences in the mean characteristic path length were found between the densities of 25%-30% ($p = 0.010$) and 35%-40% ($p = 0.010$). For the other pairs of densities, no significant differences in the median and mean values were inspected respectively between the densities of 20%-25% ($p = 0.527$) and 30%-35% ($p = 0.384$). For the non lesioned hemisphere, the comparison results obtained revealed significant differences in the mean values between densities of 20%-25% ($p = 0.004$), 25%-30% ($p = 0.001$) and 35%-40% ($p = 0.028$). The differences in the median characteristic path length between densities of 30%-35% were not considered as statistical significant ($p = 0.068$).

From the median and mean values, respectively indicated in Tables 4.2 and 4.1, it is noteworthy that the characteristic path length of both lesioned and non lesioned hemispheres decreased as more connections were included in the networks. These results proposed a higher global integration as more connections were considered which suggested that the communication between brain regions was more facilitated. Thus, the number of edges that needed to be crossed from one node to another seemed to decrease resulting in shorter path lengths.

5.1.2 Global efficiency

The statistical results expressed in Table 4.3 revealed that the distribution of the global efficiency for the different pairs of densities followed a normal distribution, for lesioned hemisphere: ($p = 0.080$), 25%-30% ($p = 0.147$), 30%-35% ($p = 0.264$) and 35%-40% ($p = 0.826$). As a result, the two-sample paired *t* test was applied for the between-threshold comparisons. The corresponding results were shown in Table 4.4 and expressed whether the differences in the mean global efficiency values between densities were considered as statistical significant. Significant differences were found between densities of 20%-25% ($p = 0.002$), 25%-30% ($p = 2.200\text{E-}04$), 30%-35% ($p = 2.280\text{E-}04$) and 35%-40% ($p = 1.500\text{E-}04$), in lesioned hemisphere. Analogous results were obtained for the non lesioned between-threshold comparison: 20%-25% ($p = 6.400\text{E-}06$), 25%-30% ($p = 1.500\text{E-}06$), 30%-35% ($p = 2.000\text{E-}04$) and 35%-40% ($p = 1.200\text{E-}05$). However, the results for the pairs of densities of 25%-30% and 30%-35% reflected significant differences in the median values due to the normality results: $p = 0.002$ and 0.005, respectively. For the remaining pairs of densities the normality nature of their distribution was verified: 20%-25% ($p = 0.933$) and 35%-40% ($p = 0.383$). Consequently, the two-sample paired *t* test was applied revealing differences in the mean values.

As the threshold applied in the network increased, the global efficiency of lesioned and non lesioned networks increased as well (Table 4.1). This increase seemed to be associated to the shorter path lengths between two regions that were obtained and discussed in Subsection 5.1.1. As the number of edges that need to be crossed to connect one region to another decreases, it is expected that the efficiency in the information transfer between them increases. Thus, these findings were concordant to the previous discussion of characteristic path length.

The nodal efficiency is an index for reflecting the role of nodes in the information processing. In this context, a comparison of the nodal global efficiency between thresholds was also performed, following the same directions as for the between-threshold comparison of the global efficiency.

These nodal results were shown in Tables A.7 and A.8, respectively for the lesioned and non lesioned hemispheres. Significant differences in the global efficiency were found for all regions except for the PHG (parahippocampal gyrus) node between densities of 20%-25%, in the lesioned hemisphere. For

the between-threshold comparison regarding the pairs of densities of 25%-30%, 30%-35% and 35%-40%, all nodes exhibited significant differences. Concerning the non lesioned hemisphere, significant differences were found in all regions between all the densities, except for the TPOmid (middle temporal gyrus, temporal pole) node.

These results indicated significant differences in respect to the nodal global efficiency means or medians, according to the normality results obtained for each region (Tables A.5 and A.6, respectively for lesioned and non lesioned hemispheres). Therefore, inspecting the nodal mean and median values of the global efficiency respectively presented in Tables A.1 and A.2, conclusions on whether the functional reorganization of the networks significantly increased the efficiency in the information transfer involving these nodes could be inferred. The results showed that these nodal global efficiency significant differences corresponded to an increase from one density to another. As more connections were included in the networks, the efficiency in the information transfer significantly increased in scattered areas of the networks demonstrating their constructive functional reorganization. Thereby, these nodes seemed to significantly contributed for the significant increase in the global information processing of the networks (Tables 4.1 and 4.2).

5.1.3 Clustering coefficient

From Table 4.3, the lesioned normality results indicated that the distribution of the clustering coefficient data followed a normal distribution for all pairs of densities: 20%-25% (p = 0.560), 25%-30% (p = 0.069), 30%-35% (p = 0.893) and 35%-40% (p = 0.512). Analogously, the normality nature of the non lesioned distribution was proved for the following pairs of densities: 20%-25% (p = 0.178), 25%-30% (p = 0.969) and 30%-35% (p = 0.927). Opposite results were obtained for the pair of densities 35%-40% (p = 0.007).

As a consequence, the between-threshold differences were computed using different tests according to these results. These results were shown in Table 4.4 and indicated significant differences in the mean clustering coefficient were found between all densities: 20%-25% (p = 0.003), 25%-30% (p = 0.005), 30%-35% (p = 0.004) and 35%-40% (p = 5.500E-04), for the lesioned hemisphere. Analogous findings were inspected for the non lesioned hemisphere: 20%-25% (p = 0.002), 25%-30% (p = 0.007), 30%-35% (p = 0.003) and 35%-40% (p = 0.006). However, it should be noted that this latter result reflected significant differences in the median values between densities of 35% and 40%, unlike the other results.

Observing Tables 4.1 and 4.2, it was evident that the mean and median clustering coefficient values for lesioned and non lesioned hemispheres increased across the different thresholds. This demonstrated that as more connections were included in both networks, a more concentrated clustering of local connections and stronger local information processing capacity of the networks was verified.

For the nodal clustering coefficient, the results of the between-threshold comparison for the lesioned and non lesioned hemispheres can be found in Tables A.11 and A.12, respectively. Even so, the significant results are summarized in Tables 5.1 and 5.2, respectively for lesioned and non lesioned hemispheres.

Location	Regions	Lesioned hemisphere			
		20%-25%	**25%-30%**	**30%-35%**	**35%-40%**
Frontal	ORBinf	-	-	9.600E-06*	-
Parietal-(pre)motor	SPG	0.009*	-	-	-
Temporal	STG	-	-	-	0.025*
Medial temporal	HIP	-	1.200E-04*	-	-
	TPOsup	-	0.038*	-	-
Subcortical	OLF	-	0.026*	-	-
Occipital	CAL	-	0.009*	0.028*	0.028*

Table 5.1: Regions where significant differences in clustering coefficient were found between densities of 20%-25%, 25%-30%, 30%-35% and 35%-40%, for the lesioned hemisphere, as well as their corresponding location in the hemisphere. The values refer to the P values obtained using the two-sample paired t test or Wilcoxon matched pairs test. * indicates P value < 0.05 which represents statistical significance. Regions names were omitted but they were indicated in Table 3.2 in Methods.

Location	Regions	Non lesioned hemisphere			
		20%-25%	**25%-30%**	**30%-35%**	**35%-40%**
Frontal	MFG	-	0.006*	-	0.006*
Parietal-(pre)motor	PreCG	0.002*	-	-	-
	SMG	-	-	-	0.031*
	PoCG	-	-	0.010*	-
	PCL	0.027*	-	-	-
Medial temporal	TPOsup	-	1.100E-04*	-	0.045*
Occipital	LING	0.012*	-	-	-

Table 5.2: Regions where significant differences in clustering coefficient were found between densities of 20%-25%, 25%-30%, 30%-35% and 35%-40%, for the non lesioned hemisphere, as well as their corresponding location in the hemisphere. The values refer to the P values obtained using the two-sample paired t test or Wilcoxon matched pairs test. * indicates P value < 0.05 which represents statistical significance. Regions names were omitted but they were indicated in Table 3.2 in Methods.

The results displayed in Tables 5.1 and 5.2 indicated the regions where significant between-densities differences in the clustering coefficient were found, respectively for lesioned and non lesioned hemispheres. Furthermore, the analysis of their corresponding clustering coefficient values elucidated about the significant contribution of these nodal results in the significant increases of both lesioned and non lesioned global clustering coefficient. Different statistical tests were applied for this nodal between-threshold comparison, depending on the nodal normality results expressed in Tables A.9 and A.10, respectively for lesioned and non lesioned hemispheres. Therefore, both mean and median clustering coefficient values were analysed (Tables A.3 and A.4, respectively). The relevant values for the regions whose significant differences between densities were found in the hemispheres are resumed in Table 5.3.

Hemisphere	Regions	Proportional threshold				
		20%	**25%**	**30%**	**35%**	**40%**
Lesioned	ORBinf	-	-	0.658	0.698	-
	SPG	0.666±0.118	0.731±0.124	-	-	-
	STG	-	-	-	0.665±0.140	0.698±0.145
	HIP	-	0.362±0.257	0.550±0.150	-	-
	TPOsup	-	0.596±0.103	0.637±0.109	-	-
	OLF	-	0.689	0.867	-	-
	CAL	-	0.621±0.158	0.670±0.165	0.698	0.721±0.140
		-	-	0.674	0.693±0.152	-
Non lesioned	MFG	-	0.565±0.067	0.639±0.069	0.644±0.106	0.678±0.108
	PreCG	0.522±0.114	0.577±0.120	-	-	-
	SMG	-	-	-	0.737±0.100	0.768±0.096
	PoCG	-	-	0.632±0.105	0.678±0.116	-
	PCL	0.564	0.644	-	-	-
	TPOsup	-	0.468	0.571	0.574±0.111	0.641±0.091
	LING	0.533±0.085	0.575±0.096	-	-	-

Table 5.3: Median or mean clustering coefficient for the regions where significant differences in clustering coefficient were found between densities of 20%-25%, 25%-30%, 30%-35% and 35%-40%, for both lesioned and non lesioned hemispheres. The mean values are presented as mean±standard deviation. Regions names were omitted but they were indicated in Table 3.2 in Methods.

It is noteworthy that the significant differences in clustering coefficient for the nodes indicated in Tables 5.1 and 5.2, respectively for lesioned and non lesioned hemispheres reflected significant increases of the clustering coefficient between densities (Table 5.3). It seemed that the nodal results significantly contributed for the significant increase of the clustering coefficient, as more connections were included in both networks.

The clustering coefficient results are usually integrated with those for local efficiency to assess how efficient is a communication between the first neighbors of a node and the corresponding network's potential for the local information transfer. In this context, Subsection 5.1.4 will discuss the local efficiency results obtained in this study.

5.1.4 Local efficiency

The results organized in Table 4.3 showed that the distribution of the local efficiency data followed a normal distribution considering all pairs of densities in the lesioned hemisphere: 20%-25% (p = 0.688), 25%-30% (p = 0.242), 30%-35% (p = 0.839) and 35%-40% (p = 0.072). Analogous results were obtained for the non lesioned hemisphere, except at the pair of densities 35%-40% (p = 0.023): 20%-25% (p = 0.347), 25%-30% (p = 0.698) and 30%-35% (p = 0.133).

Consequently, the between-threshold comparison resorted on the mean local efficiency for the lesioned and non lesioned hemispheres, excluding the comparison between densities of 35% and 40% in the non lesioned hemisphere. For this latter, differences in terms of the median values were investigated. The results were shown in Table 4.4. For the lesioned hemisphere significant differences in local efficiency between all densities were found: 20%-25% (p = 0.004), 25%-30% (p = 0.007), 30%-35% (p = 0.004) and 35%-40% (p = 0.002). Analogous results were obtained for the non lesioned hemisphere: 20%-25% (p = 5.900E-05), 25%-30% (p = 0.005), 30%-35% (p = 5.900E-05) and 35%-40% (p = 2.500E-05).

The inclusion of more connections in the networks resulted in a significant increase of the efficiency in the information transfer between the nearest neighbors of the nodes. This indicated a greater local pro-

cessing in the networks (Tables 4.1 and 4.2, respectively for mean and median values). In summary, the local efficiency results were consistent to the significant increases inspected for the clustering coefficient and discussed in the previous Subsection 5.1.3.

5.1.5 Small-worldness

Regarding the lesioned hemisphere, no significant differences in the small-worldness were found between densities of: 20%-25% (p = 0.340), 25%-30% (p = 0.650), 30%-35% (p = 0.470) and 35%-40% (p = 0.650) (Table 4.4). Analogous results were obtained for the non lesioned hemisphere: 20%-25% (p = 0.150), 25%-30% (p = 0.212) and 35%-40% (p = 0.453) (Table 4.4). However, from densities of 30% to 35%, the small-worldness of the non lesioned hemisphere significantly decreased (p = 0.037). The comparison between the densities of 20%-25% and 35%-40% in the lesioned hemisphere resorted on the median values of the small-worldness (p = 6.415E-04 and 0.009, respectively). For the other pairs of densities, between-threshold comparison was based on the mean values: 25%-30% (p = 0.381) and 30%-35% (p = 0.241) (Table 4.3). For the non lesioned hemisphere, the normality nature of the small-worldness distribution involving the densities of 30% and 35% was not verified (p = 0.032). As a result, the corresponding comparisons resorted on the median values of the small-worldness. Opposite results were obtained for the remaining densities: 20%-25% (p = 0.469), 25%-30% (p = 0.681) and 35%-40% (p = 0.475) (Table 4.3). These latter results indicated that the further comparisons were based on the mean values.

The mean and median small-wordness of both lesioned and non lesioned networks decreased across densities, except for the lesioned network from densities of 35% to 40% (Tables 4.1 and 4.2, respectively). This decrease suggested that, despite the maintenance of the small-world topology (values > 1), the balance between the local processing and the global integration decreased. Considering the previous results, as more connections were included in the networks, the global integration of the networks increased promoting an increase of the communication and information transfer between distributed regions. Furthermore, the segregation of the networks increased as well reflecting the improvement of the local processing. However, with the inclusion of more connections, the networks demonstrated a lower ability for balancing their increase of both local processing and global integration.

At density of 40%, the increase in the small-worldness inspected for the lesioned network proposed an improvement of balance between the local specialization and the global integration. The lesioned network revealed a constructive reorganization in terms of its small-world property though less optimal than that of the non lesioned network.

5.2 Comparison of graph metrics between lesioned and non lesioned hemispheres, for each proportional threshold

In this section, it is intended to compare the lesioned and non lesioned hemispheres in respect to their topological properties, inducing the impact of the presence of a lesion and their short- and long-distance as well as between-hemispheres influence, when thresholding the networks at different density values.

The lesion may had induced disturbances in the hemisphere where it was located not only in its vicinity but also in distant regions which could had been reflected in a decrease in the functional connectivity between distributed regions. Furthermore, through between-hemispheres functional interactions, the non lesioned hemisphere may also had been disturbed by the lesion. Despite not discarding this disturbance

in the non lesioned hemisphere, the lesion-induced disturbances within the lesioned hemisphere seemed to promote a (greater) decrease of the functional connectivity between regions (Figure 3.4).

For the between-hemispheres comparison, the integration properties of the networks will be analysed through the characteristic path length and global efficiency metrics, while the clustering coefficient and local efficiency will be discussed for the characterization of the networks' segregation. Moreover, the small-worldness of both networks will be inferred and discussed integrating the results of the integration and segregation network's properties.

5.2.1 Characteristic path length

Resorting to Table 4.5, the normality results demonstrated that the distribution of the characteristic path length data followed a normal distribution for all densities: 20% ($p = 0.907$), 25% ($p = 0.485$), 30% ($p = 0.488$), 35% ($p = 0.504$) and 40% ($p = 0.727$). Consequently, the two-sample paired t test was applied in these densities and the mean values of lesioned and non lesioned hemispheres were compared. The results of this between-hemispheres comparison were shown in Table 4.6. For all densities, no significant differences between hemispheres were obtained: 20% ($p = 0.983$), 25% ($p = 0.600$), 30% ($p = 0.688$), 35% ($p = 0.938$) and 40% ($p = 0.820$). Observing Table 4.1, the mean lesioned value at density of 20% was lower, while the opposite was verified at the remaining densities. Despite not significantly, the lower characteristic path length at density of 20% revealed that the lesioned network was characterized by shorter path lengths in comparison to the non lesioned hemisphere. The inclusion of more connections in the networks reversed these results. The significant decrease between densities of 20% and 25% merely inspected in the non lesioned hemisphere may had been related to reversal inspected at density of 25%. The lower non lesioned mean values for the other densities indicated shorter path lengths which would imply a greater effective integrity and a more rapid information propagation between and across different regions.

In Subsection 5.2.2, the global efficiency results will be detailed and conclusions involving these characteristic path length results will be induced clarifying the differences in the global integration between hemispheres.

5.2.2 Global efficiency

The normal distribution of the global efficiency was verified at all densities, except at density of 35%: 20% ($p = 0.839$), 25% ($p = 0.915$), 30% ($p = 0.208$), 35% ($p = 0.031$) and 40% ($p = 0.096$) (Table 4.5). As a result, the two-sample paired t test was applied to compare the lesioned and non lesioned hemispheres in respect to their mean values at densities of 20%, 25%, 30% and 40%, while for the between-hemispheres comparison at density of 35% the Wilcoxon matched pairs test was used. This test was performed in terms of the median global efficiency values. Inspecting the results in Table 4.6, no significant differences in global efficiency between both hemispheres were obtained, for all thresholds: 20% ($p = 0.158$), 25% ($p = 0.230$), 30% ($p = 0.260$), 35% ($p = 0.569$) and 40% ($p = 0.748$). The median global efficiency at density of 35% was lower in the lesioned hemisphere (Table 4.2). From the mean values displayed in Table 4.1, the lesioned global efficiency values were lower at all densities, except at density of 40%. The lower mean global efficiency of the lesioned network at density of 20% was not consistent with the mean characteristic path length whose results indicated shorter path lengths in the lesioned network. As a consequence, the efficiency in the information transfer should had been higher in the lesioned network. Furthermore, the higher global efficiency inspected in lesioned network at density of 40% would imply shorter path lengths and a more rapid information transfer between distributed regions. This result was

also not concordant to the characteristic path length at density of 40%. Considering the lesion-induced disturbances within the lesioned hemisphere, compensatory paths seemed to be created improving the efficiency in the information transfer between the regions in the lesioned hemisphere. The functional reorganization of the lesioned network at 40% promoted these conclusions. For the remaining densities, the shorter path lengths in non lesioned network indicated a more efficient information transfer, including the lower median global efficiency of the lesioned network at density of 35%.

As explained in Part 2.3.5 of Background, in spite of the proportional thresholds seeming to promote more stable network measures, their instability at reasonable ranges was also expected. The unconformity of the previous results may had also derived from the small number of subjects who participated in this study that could had exaggerated or minimized the differences between lesioned and non lesioned networks.

In summary, the selection of a highest density (40%) seemed to enlighten the plasticity occurred in the lesioned hemisphere in terms of the global integration.

For the nodal analysis, the results from the between-hemispheres comparison were indicated in Table A.14. Even so, the regions where significant differences in the global efficiency were found between lesioned and non lesioned hemispheres are summarized in Table 5.4.

		Proportional threshold			
Location	**Regions**	**20%**	**25%**	**30%**	**35%**
Frontal	SFGmed	-	0.016*	0.047*	-
Parietal-(pre)motor	SMG	0.013*	-	-	-
Temporal	HES	0.040*	-	-	-
	STG	-	-	0.040*	-
Subcortical	PAL	0.014*	-	-	-
	THA	0.047*	0.047*	-	0.037*

Table 5.4: Regions where significant differences in global efficiency were found between hemispheres, for the densities of 20%, 25%, 30% and 35%, as well as their corresponding location in the hemisphere. The values refer to the *P* values obtained using the paired *t* test or Wilcoxon matched pairs test. * indicates *P* value < 0.05 which represents statistical significance. Regions names were omitted but they were indicated in Table 3.2 in Methods.

These results were obtained through the application of either two-sample paired *t* test or Wilcoxon matched pairs test whose selection depended on the normality results shown in Table A.13. Furthermore, for the regions where two-sample paired *t* tests were applied, the comparison between hemispheres resorted on the mean values, while the application of the Wilcoxon matched pairs tests used the median global efficiency values of both lesioned and non lesioned hemispheres to compare them.

The further evaluation of the mean and median global efficiency values, respectively indicated in Tables A.1 and A.2 intended to explain whether the significant differences referred to significantly lower or higher nodal global efficiency in the lesioned network. These values are summarized in Table 5.5.

Hemisphere	Regions	Proportional threshold			
		20%	**25%**	**30%**	**35%**
Lesioned	SFGmed	-	0.527	0.552	-
	SMG	0.489±0.054	-	-	-
	HES	0.311±0.160	-	-	-
	STG	-	-	0.644±0.074	-
	PAL	0.247±0.127	-	-	-
	THA	0.220±0.215	0.262±0.250	-	0.499±0.108
Non lesioned	SFGmed	-	0.538	0.598	-
	SMG	0.562±0.045	-	-	-
	HES	0.498±0.101	-	-	-
	STG	-	-	0.711±0.061	-
	PAL	0.375±0.086	-	-	-
	THA	0.468±0.067	0.521±0.085	-	0.620±0.088

Table 5.5: Median or mean nodal global efficiency for the regions where significant differences in global efficiency were found between hemispheres, for the densities of 20%, 25%, 30% and 35%. The mean values are presented as mean±standard deviation. Regions names were omitted but they were indicated in Table 3.2 in Methods.

The significant between-hemispheres differences inspected in those nodes referred to significant higher global efficiency values in non lesioned hemisphere. Besides, it was evident the higher mean (Table 4.1) and median (Table 4.2) global efficiency of the non lesioned hemisphere for the densities of 20%, 25%, 30% and 35%. Therefore, these nodal results seemed to significantly contribute for the corresponding global efficiency increase of the non lesioned network.

Despite not discarding the lesion-induced disturbances reaching the non lesioned hemisphere, the perturbations caused by the lesion seemed to conduce to a (greater) decrease in the information transfer between those regions and the other nodes in the hemisphere where the lesion was located. In addition, the significant lower global efficiency of frontal, parietal-(pre)motor and temporal regions in lesioned hemisphere may had been associated to the presence of the lesions located in these areas.

5.2.3 Clustering coefficient

The results from Table 4.5 demonstrated that the clustering coefficient distribution was not significantly different from the normal distribution, for all the evaluated densities: 20% (p = 0.892), 25% (p = 0.458), 30% (p = 0.136), 35% (p = 0.620) and 40% (p = 0.604). As a result, the two-sample paired t test could be applied to perform the between-hemispheres comparison at all densities in terms of their mean values. The results showed no significant between-hemispheres differences, for all thresholds: 20% (p = 0.871), 25% (p = 0.429), 30% (p = 0.327), 35% (p = 0.626) and 40% (p = 0.205) (Table 4.6).

Inspecting the mean clustering coefficient in Table 4.1, the lesioned values were lower, for all densities, except at 35% and 40%. These higher lesioned results indicated that the inclusion of more connections allowed for a higher concentration of local connections at densities of 35% and 40%. Therefore, it was expected that the lesioned network had a higher potential for the local information transfer. The functional reorganization of the lesioned network at densities of 35% and 40% suggested local compensatory mechanisms that seemed to had been created with a purpose of compensating the decrease of distant functional connectivity caused by the lesion-induced perturbations within the lesioned hemisphere.

The calculation of the differences in nodal clustering coefficient between lesioned and non lesioned hemispheres enabled the determination of which nodes were important for the local information processing. The results from this comparison were shown in Table A.16 and are summarized in Table 5.6.

Location	Regions	Proportional threshold			
		20%	**25%**	**30%**	**35%**
Frontal	ORBmid	-	0.040*	-	-
	ORBinf	-	-	-	0.047*
Parietal-(pre)motor	ANG	0.026*	-	-	0.005*
Medial temporal	HIP	0.012*	0.005*	-	-
Subcortical	CAU	-	-	0.016*	-
	THA	0.036*	0.016*	-	-

Table 5.6: Regions where significant differences in clustering coefficient were found between lesioned and non lesioned hemispheres, for densities of 20%, 25%, 30% and 35%, as well as their corresponding location in the hemisphere. The values refer to the P value obtained from the application of paired t test or Wilcoxon matched pairs test. * indicates P value < 0.05 which represents statistical significance. Regions names are omitted but referred in Table 3.2 in Methods.

These results indicated that the local processing involving the same nodes significantly differ according to their location (lesioned or non lesioned hemispheres). Regarding this comparison, paired t tests were used for all the previously mentioned nodes, except for the subcortical region of CAU (caudate nucleus) node. The reason regarded the fact that the distribution of the clustering coefficient respecting the lesioned and non lesioned data of the CAU node did not follow a normal distribution (Table A.15), unlike the other nodes. Thus, the comparison between both hemispheres was based on the median clustering coefficient values for this subcortical node. The other significant nodal results reflected differences in the mean values. The mean and median clustering coefficient values can be found in Tables A.3 and A.4, respectively. Nevertheless, the values for the regions where significant between-hemispheres differences in clustering coefficient were found are shown in Table 5.7.

Hemisphere	Regions	Proportional threshold			
		20%	**25%**	**30%**	**35%**
Lesioned	ORBmid	-	0.407±0.350	-	-
	ORBinf	-	-	-	0.728±0.157
	ANG	0.877±0.121	-	-	0.801±0.076
	HIP	0.297±0.224	0.362±0.257	-	-
	CAU	-	-	0.667	-
	THA	0.210±0.360	0.277±0.353	-	-
Non lesioned	ORBmid	-	0.753±0.196	-	-
	ORBinf	-	-	-	0.572±0.076
	ANG	0.624±0.165	-	-	0.719±0.092
	HIP	0.606±0.153	0.632±0.167	-	-
	CAU	-	-	0.800	-
	THA	0.619±0.308	0.751±0.176	-	-

Table 5.7: Median or mean clustering coefficient values for the regions where significant differences between lesioned and non lesioned hemispheres were found, for densities of 20%, 25%, 30% and 35%. Regions names are omitted but referred in Table 3.2 in Methods.

The functional reorganization of the lesioned network at densities of 20% and 35% allowed for a significantly higher level of local connectedness of the ANG (angular gyrus) node in comparison to the non lesioned network (Table 5.7). This result suggested that more local information was shared involving this node in the lesioned network. Furthermore, the significant higher lesioned clustering coefficient of the ANG node at density of 35% seemed to significantly contribute for the higher lesioned global clustering coefficient. Analogous results and conclusions could be inferred for the clustering coefficient of the ORBinf (inferior frontal gyrus, orbital) node.

For the other nodes, the lesion seemed to (greater) compromise their clustering coefficient in the hemisphere where it was located being lower comparing to the results of the non lesioned hemisphere. As a result, they seemed to significantly contribute for the respective higher mean and median global clustering coefficient of the non lesioned hemisphere at densities of 20%, 25% and 30%.

The association of the clustering coefficient results to the local efficiency intends to explain the efficiency of communication between the first neighbors of a node. The local efficiency results will be discussed in Subsection 5.2.4 and a relationship to the clustering coefficient conclusions will be established.

5.2.4 Local efficiency

From the results expressed in Table 4.5, the local efficiency distribution did not follow a normal distribution merely at the density of 35% (p = 0.023): 20% (p = 0.402), 25% (p = 0.660), 30% (p = 0.451) and 40% (p = 0.149). Consequently, the hemispheres were compared in terms of their mean values for all the densities through the application of the two-sample paired t test, except for the density of 35% whose comparison was conduced by the Wilcoxon matched pairs test. Therefore, the between-hemispheres comparison at density of 35% resorted on the median local efficiency values. The results revealed no statistical significant differences between lesioned and non lesioned hemispheres, for each threshold: 20% (p = 0.297), 25% (p = 0.195), 30% (p = 0.137), 35% (p = 0.585) and 40% (p = 0.760) (Table 4.6).

Inspecting the corresponding mean and median local efficiency values respectively displayed in Tables 4.1 and 4.2, it could be seen that the non lesioned values were higher at all densities, except at the density of 40%. These results meant that information transfer through the neighbors of a node seemed to be more efficient in the non lesioned network. The fact that the non lesioned network was more locally interconnected led to a higher efficiency in the local information transfer (until density of 35%). At density of 35%, the lesioned network revealed to be more locally interconnected; however it was not more locally efficient. At density of 40%, the lesioned values increased enough to exceed the non lesioned local efficiency which indicated that the connections included when thresholding the lesioned network at 40% allowed for the neighbors of a node being more densely interconnected. This enabled a more efficient communication between them, and hence, a higher global local efficiency. The results at the highest density (40%) were in accordance to the corresponding clustering coefficient findings and conclusions.

The small number of subjects that were considered in this study might had been associated to the inconsistencies observed at density of 35%.

So, thresholding the lesioned network at higher densities, mainly at density of 40%, enabled to inspect the plasticity that could had been occurred in the lesioned hemisphere promoting the establishment of local compensatory mechanisms.

5.2.5 Small-worldness

From the results reported in Table 4.5, the distribution in respect to the lesioned and non lesioned small-worldness was not significantly different from the normal distribution at all densities: 20% (p = 0.319), 25% (p = 0.750), 30% (p = 0.967), 35% (p = 0.666) and 40% (p = 0.605).

Therefore, the two-sample paired t test was applied for the between-hemispheres comparison at all thresholds, resulting in comparisons in terms of the mean small-worldness. The results were shown in

Table 4.6 and indicated no significant between-hemispheres differences for all the proportional thresholds: 20% ($p = 0.986$), 25% ($p = 0.327$), 30% ($p = 0.290$), 35% ($p = 0.507$) and 40% ($p = 0.914$).

Despite not significantly, the mean small-worldness was lower in the lesioned hemisphere, for all the densities (Table 4.1). These results suggested a greater balance of the local processing and global integration of the non lesioned network. The functional reorganization of the lesioned network was not more constructive when analysing its ability to balance the global integration and local processing and comparing it to the non lesioned network. Therefore, the lesion-induced disturbances seemed to (greater) disturb the hemisphere where the lesion was located. However, the functional reorganization of the lesioned network at density of 40% proposed a plasticity occurring in the lesioned network regarding the global and local connectednesses. Moreover, an improvement of the lesioned network in balancing the global integration and the local specialization was inspected.

5.3 Comparison to previous studies

In this section, a comparison between the results of this study and the findings from previous studies will be discussed. The following investigations resorted to the graph theoretical analysis to compute and compare the small-world properties between whole-brain lesioned group of patients and healthy controls (HCs). Of these, a study conducted by Wang et al. [40], recruited patients with white matter lesions (WMLs).

The characteristic path length of both lesioned and healthy groups decreased across densities in the studies conducted by Huang et al. [39] and Wang et al. [40]. This indicated that the inclusion of more connections promoted a decrease in the minimum number of edges that need to be crossed to connected one region to another, regardless the presence of a lesion. Similarly, the distribution of the characteristic path length obtained in this study for both lesioned and non lesioned hemispheres also decreased across densities. Huang et al. [39] and Wang et al. [40] also found longer path lengths in the lesioned networks and demonstrated that the long-distance information integration was reduced in lesioned groups. An explanation for these results involved the decreased distant functional connectivity caused by the lesion which also reduced the capacity for the information transmission. The results obtained in this study also revealed longer path lengths in the lesioned network, except at density of 20%. Quantitatively, the lesioned and non lesioned results were more concordant to the results obtained by Huang et al. [39] that were lower in comparison to the results from the study conducted by Wang et al. [40].

The distribution of the non lesioned characteristic path length across densities was concordant to the distributions of both lesioned and healthy groups which precluded to disclose whether the lesion-induced disturbances reached the non lesioned hemisphere affecting the characteristic path length as it did for the lesioned hemisphere.

From the studies conducted by Huang et al. [39], Park et al. [38] and Wang et al. [40], the global efficiency increased as more connections were included in both lesioned and healthy networks. This indicated that the information transfer between brain regions was more facilitated as more connections were included. The global efficiency of both lesioned and non lesioned hemispheres across densities, obtained in this study, increased as well.

The results obtained from Huang et al. [39] revealed a lower global efficiency in the lesioned groups, from density of 20%. Park et al. [38] demonstrated a conserved global efficiency of the lesioned network. Besides, Wang et al. [40] obtained a lower global efficiency of the lesioned groups which was concordant to their longer path lengths. The results from this study were in accordance to the results from the studies conducted by Huang et al. [39] and Wang et al. [40], until density of 40% where the lesioned global

efficiency was higher. Quantitatively, both lesioned and non lesioned global efficiency results were concordant to the results from the previous studies; however, for the highest densities the higher results were more similar to the findings of Park et al. [38].

The distribution of the non lesioned global efficiency across the different thresholds was concordant to the distributions of both lesioned and healthy groups excluding the possibility for conclusions about the lesion-induced disturbances reaching the non lesioned hemisphere and affecting its global efficiency. This inference was expected due to the association of global efficiency to the characteristic path length.

The studies conducted by Huang et al. [39] and Park et al. [38] obtained an increase of the clustering coefficient as more connections were included in both lesioned and healthy networks. The opposite was inspected for the clustering coefficient results acquired by Wang et al. [40] (decreased across densities). They disclosed that the lesioned networks were less locally interconnected being the local information processing capacity weaker. The clustering coefficient distribution of lesioned and non lesioned hemispheres, obtained in this study, was concordant to the findings of Huang et al. [39] and Park et al. [38]. Huang et al. [39] found that the patients group exhibited lower clustering coefficient values than HCs, for all densities, while the clustering coefficient was preserved in the study conducted by Park et al. [38]. Despite that, a slightly higher clustering coefficient of the lesioned group was inspected, for the lower densities. The lesioned and non lesioned clustering coefficient from this study were in concordance to the results obtained by Huang et al. [39], until density of 35%. From density of 35%, the lesioned network seemed to exhibit a stronger local processing capacity. Quantitatively, the non lesioned results were accordant to the clustering coefficient of the healthy group while for the lesioned hemisphere, the clustering coefficient was higher than the results of the lesioned group. The results of this study were also concordant to the results from the study conducted by Park et al. [38]; however their increased was lower.

The distribution of the non lesioned clustering coefficient across densities was in accordance to the distributions of both lesioned and healthy groups for the results obtained by Huang et al. [39] and Park et al. [38] precluding conclusions on whether the lesion-induced disturbances reached the non lesioned hemisphere affecting the clustering coefficient as it occurred for the lesioned hemisphere. The distribution of the clustering coefficient for the non lesioned hemisphere was not concordant to either the distribution of clustering coefficient for lesioned or healthy groups from the study conducted by Wang et al. [40]. Thereby, no further information about the disturbances caused by the lesion reaching the non lesioned hemisphere and affecting the clustering coefficient findings could be inferred.

From the nodal results obtained by Huang et al. [39] alterations of clustering coefficient in preoperative LGG at density of 20% included the OLF (olfactory cortex), HES (Heschl's gyrus), and CAL (calcarine fissure and surrounding cortex) regions, respectively located in subcortical, temporal and occipital brain areas. The nodes where significant differences in the clustering coefficient between lesioned and non lesioned hemispheres were found at density of 20% involved the ANG, HIP (hippocampus) and THA regions which are respectively located in parietal-(pre)motor, medial temporal and subcortical areas. The difference in the nodal results may be related to the differences in the lesions' location in the brain. Their lesions were merely located in the frontal lobe while the lesions of the patients analysed in this study involved other regions and pathologies.

The local efficiency increased for both lesioned and healthy groups of the study conducted by Huang et al. [39] and Park et al. [38], as more connections were included in the networks. These results were consistent to the corresponding clustering coefficient results revealing a denser local connectedness of the brain functional networks as the density increased. Wang et al. [40] obtained a decrease in the local efficiency across densities, for both lesioned and healthy groups. Therefore, the local functional

reorganization of networks was not constructive leading to a sparse local connectedness and hence a decrease in the efficiency of local information transfer. The lesioned and non lesioned results from this study were concordant to the local efficiency increase across thresholds inspected by Huang et al. [39] and Park et al. [38]. Furthermore, they were all quantitatively concordant.

Huang et al. [39] found that the local efficiency was lower for the lesioned groups which was in accordance to the clustering coefficient results. Moreover, Park et al. [38] inspected that the lesioned local efficiency was preserved for all densities, except for 16%, 18% and 24% where the lesioned values were significantly higher than that of HCs. The results from this study were concordant to the results obtained by Huang et al. [39] until density of 40%. At this highest density, the local efficiency of the lesioned hemisphere was concordant to the results for the lesioned group from the study conducted by Park et al. [38] (higher local efficiency).

The distribution of the non lesioned local efficiency across the proportional thresholds was accordant to the distributions of both lesioned and healthy groups for the results obtained by Huang et al. [39] and Park et al. [38] which precluded to conclude about the lesion-induced disturbances had reached the non lesioned hemisphere affecting its local efficiency. The distribution of the local efficiency for the non lesioned hemisphere was not concordant to either the distribution of local efficiency for lesioned or healthy groups from the study conducted by Wang et al. [40]. Thus, further conclusions relating the influence of the lesion in the local efficiency of the non lesioned hemisphere could not be inferred.

In the studies conducted by Huang et al. [39], Park et al. [38] and Wang et al. [40], as more connections were included in both healthy and lesioned networks, the small-worldness decreased. This showed that the networks tended to be more random. However, an increase of the local processing of the networks was suggested to maintain the small-world property. It should be noted that the results from the study conducted by Wang et al. [40] indicated a decrease of the small-worldness as more connections were included but the small-worldness did not tended to be preserved. The small-worldness distribution of both lesioned and non lesioned hemispheres, obtained in this study, was concordant to the previous findings of the small-worldness preservation. However, Huang et al. [39] found a higher small-property of LGG groups which showed the changes in the overall organization of the lesioned networks compared to HCs. Quantitatively, both lesioned and non lesioned small-worldness results from this study were concordant to the small-worldness of HCs. Park et al. [38] also demonstrated a conserved small-world topology of the lesioned group comparing to HCs. Even so, the small-worldness of both lesioned and healthy groups was higher than the results obtained in this study, for lesioned and non lesioned hemispheres. Wang et al. [40] obtained a decreased small-world property in the lesioned groups. Quantitatively, the results of lesioned and non lesioned hemispheres were in accordance to the results of healthy and lesioned groups.

The distribution of the non lesioned small-worldness across densities was concordant to the distributions of both lesioned and healthy groups. Then, it was not possible to disclose whether the lesion-induced perturbations disturbed the non lesioned small-worldness as it seemed to affect it in the lesioned hemisphere.

In conclusion, the results from this study seemed to be consistent and concordant to the previous studies, being the major differences involving the higher global and local efficiencies of the lesioned network as well as the increase of the lesioned small-worldness at density of 40%. Explanations for these differences may include differences in the investigation's protocol and pathologies of the patients.

Chapter 6

Conclusion

Although the lesion hemispheric location was unilateral, both hemispheres could be affected by the lesion, through short- and long-distance within the lesioned hemisphere. Furthermore, between-hemispheres functional interactions reaching the non lesioned hemisphere might had been associated to lesion-induced disturbances in this hemisphere.

In this perspective, the lesioned and non lesioned hemispheres were analysed in terms of their integration and segregation topological properties to conclude about the lesion's influence in both hemispheres. Furthermore, the effect of thresholding in those network properties was also evaluated.

For the integration analysis, it was demonstrated that as more connections were included in the networks, the path lengths between regions tended to be shorter. This suggested an increase of the global integration indicating that the communication between distributed regions seem to be more facilitated. The global efficiency results corroborated these findings (increased as more connections were included). Moreover, almost all nodes seemed to significantly contributed for this increase due to the significant differences that were inspected between all pairs of densities.

The functional reorganization of the networks revealed to be more efficient in the non lesioned hemisphere at all densities, except at the highest density of 40%, which would imply a greater effective integrity and a more rapid information propagation between and across different regions. This result was concordant to the shorter path lengths of the non lesioned network at all densities, except at the lowest density of 20%. At the density of 40%, the lesioned network seemed to be more globally integrated.

The analysis of the segregation for both lesioned and non lesioned networks involved the clustering coefficient and local efficiency findings that respectively measured the level of local combination (connectedness) and propagation (efficiency) of the information. The between-threshold results of these graph measures showed that as more connections were considered in the networks, the level of local connectedness increased inducing a greater local information processing. The lesioned clustering coefficient values were lower until density of 30% (inclusive) suggesting a lower potential for the local information transfer. These results were concordant to the lower local efficiency for the lesioned network. From density of 35%, the clustering coefficient of the lesioned network was higher; however, the local efficiency results indicated a lower efficiency in the local information transfer. At density of 40%, the lesioned local efficiency increased enough to exceed the non lesioned results which proposed a higher local specialization in the lesioned network.

These results showed that the lesioned network may had compensated the lesion-induced perturbations within this hemisphere through the establishment of compensatory paths and local mechanisms. Even so, this conclusion could merely be deduced with the functional reorganization occurred when the lesioned network was thresholded at density of 40%.

Further, this study demonstrated that both lesioned and non lesioned networks revealed a small-world topological organization which enlighten the networks' ability for specialized processing to occur within densely interconnected modules and to combine information for distributed brain regions. However, as more connections were included in the networks, their ability to balance the global integration and the local processing decreased. At density of 40%, the lesioned network reflected a constructive reorganization for the local processing and global integration. Despite the compensatory mechanisms, the lesioned network exhibited a less optimal small-world organization which suggested a lower capacity in balancing the local information processing in respect to the global integration.

Inconsistencies were found at densities of 20% and 40%, for the integration results. The segregation results were only inconsistent at density of 35%. As explained in Part 2.3.5 of Background, despite the proportional thresholds seeming to improve the network stability, the instability of network measures within reasonable proportional thresholds was expected. Furthermore, it should be noted that the outliers of the data were not excluded from these analyses due to the small number of subjects. Thus, these results may also be caused by the small number of subjects who participated in this study that could had exaggerated or minimized the differences between lesioned and non lesioned networks and between thresholds. The inconsistent results obtained through the comparison of the mean values were expected due to their higher susceptibility for the outliers. Besides, the fact that the nodal results corresponded to regions that were scattered over different brain-hemispheric locations may had been a consequence from the variability of the pathologies within the group of patients: brain tumors, with different locations in the hemisphere, and a case of a cavernous malformation.

In summary, the results seemed to be sensitive to the choice of threshold. Although instabilities had been inspected in the results of this study, the selection of reasonable ranges of proportional thresholds is proposed. Therefore, it would allow for more stable networks highlighting the robustness of the results.

The lesioned hemisphere showed a lower integration and segregation than the non lesioned hemisphere, when excluding the analysis at the higher thresholds. This reflected that indeed the lesion-induced alterations affected the functional connectivity within the hemisphere where the lesion is located. At density of 40%, the functional reorganization of the lesioned network was constructive suggesting that the lesion-induced perturbation within this hemisphere were compensated through compensatory paths and local mechanisms. The functional between-hemispheres interactions could also had disturb the non lesioned hemisphere. However, from the results of this study no clear conclusion could be inferred. In addition, the comparison to previous investigations that recruited patients with lesions and healthy subjects precluded in inferring the lesion's impact in the non lesioned hemisphere.

In future studies it might be interesting to compute more additional graph measures such as the nodal degree to conclude, more accurately, about the nodal effect of including more connections (thresholding) and the integration characteristics of the networks. For the segregation conclusions, the nodal local efficiency can be also computed upgrading and consolidating the findings of the local efficiency.

The concordance between the results of this study and the findings from previous studies that went further and performed a neuro-cognitive analysis opens up for a future study of the functional cognitive performance integrating data and the results of this study. This will allow the evaluation of whether and which brain lesioned and non lesioned areas are affected by the lesion and the level of this disturbance in terms of cognitive functioning. Furthermore, a further comparison involving the non lesioned hemisphere of patients and healthy subjects might be useful to disclose the impact of the lesion in the non lesioned network. Additionally, in the current study, it was investigated and compared the lesioned and non lesioned graph metrics prior to surgery. Future studies may also focus on the establishment of an association between the topological parameters of the networks after the lesion resection and at long

term, and further include a link to the cognitive performance.

Bibliography

[1] J Ferlay et al. “Cancer incidence and mortality patterns in Europe: Estimates for 40 countries and 25 major cancers in 2018”. In: *European Journal of Cancer* 103 (2018), pp. 356–387.

[2] Raul Mattassi, Dirk A Loose, and Massimo Vaghi. *Hemangiomas and vascular malformations: an atlas of diagnosis and treatment*. springer, 2015.

[3] Nikolaos Mouchtouris et al. “Management of cerebral cavernous malformations: from diagnosis to treatment”. In: *The Scientific World Journal* 2015 (2015).

[4] Giannantonio Spena et al. “Preoperative and intraoperative brain mapping for the resection of eloquent-area tumors. A prospective analysis of methodology, correlation, and usefulness based on clinical outcomes”. In: *Acta neurochirurgica* 152.11 (2010), pp. 1835–1846.

[5] Cristina Rosazza et al. “Preoperative mapping of the sensorimotor cortex: comparative assessment of task-based and resting-state FMRI”. In: *PLoS One* 9.6 (2014).

[6] Han Lv et al. “Resting-state functional MRI: everything that nonexperts have always wanted to know”. In: *American Journal of Neuroradiology* 39.8 (2018), pp. 1390–1399.

[7] Kathleen A Garrison et al. “The (in) stability of functional brain network measures across thresholds”. In: *Neuroimage* 118 (2015), pp. 651–661.

[8] Richard S Snell. *Clinical neuroanatomy*. Lippincott Williams & Wilkins, 2010.

[9] Stephen G Waxman. *Clinical neuroanatomy*. McGraw Hill, 2010.

[10] John Harry Martin, Michael E Leonard, and Howard Radzyner. *Neuroanatomy: text and atlas*. Elsevier New York, 1989.

[11] Virginia Stark-Vance and Mary Louise Dubay. *100 Questions & answers about brain tumors*. Jones & Bartlett Learning, 2010.

[12] Kevin Y Wang, Oluwatoyin R Idowu, and Doris DM Lin. “Radiology and imaging for cavernous malformations”. In: *Handbook of clinical neurology*. Vol. 143. Elsevier, 2017, pp. 249–266.

[13] Hesheng Liu et al. “Task-free presurgical mapping using functional magnetic resonance imaging intrinsic activity”. In: *Journal of neurosurgery* 111.4 (2009), pp. 746–754.

[14] Stefan Klöppel and Christian Büchel. “Alternatives to the Wada test: a critical view of functional magnetic resonance imaging in preoperative use”. In: *Current Opinion in Neurology* 18.4 (2005), pp. 418–423.

[15] Michael G Hart et al. “Graph theory analysis of complex brain networks: new concepts in brain mapping applied to neurosurgery”. In: *Journal of neurosurgery* 124.6 (2016), pp. 1665–1678.

[16] Elizabeth W Pang and OC Snead Iii. “From structure to circuits: the contribution of MEG connectivity studies to functional neurosurgery”. In: *Frontiers in neuroanatomy* 10 (2016), p. 67.

[17] Sylvain Baillet. "Magnetoencephalography for brain electrophysiology and imaging". In: *Nature neuroscience* 20.3 (2017), p. 327.

[18] Andrei Irimia, John Darrell Van Horn, and Eric Halgren. "Source cancellation profiles of electroencephalography and magnetoencephalography". In: *Neuroimage* 59.3 (2012), pp. 2464–2474.

[19] A Hillebrand and GR Barnes. "A quantitative assessment of the sensitivity of whole-head MEG to activity in the adult human cortex". In: *Neuroimage* 16.3 (2002), pp. 638–650.

[20] Scott A Huettel, Allen W Song, Gregory McCarthy, et al. *Functional magnetic resonance imaging*. Vol. 1. Sinauer Associates Sunderland, MA, 2004.

[21] Marie T Banich and Rebecca J Compton. *Cognitive neuroscience*. Cambridge University Press, 2018.

[22] Jerrold T Bushberg et al. *The essential physics of medical imaging*. Lippincott Williams & Wilkins, 2003.

[23] Christoph Stippich. *Clinical functional MRI: presurgical functional neuroimaging*. Springer, 2015.

[24] Paulo Branco et al. "Resting-state functional magnetic resonance imaging for language preoperative planning". In: *Frontiers in human neuroscience* 10 (2016), p. 11.

[25] César Caballero-Gaudes and Richard C Reynolds. "Methods for cleaning the BOLD fMRI signal". In: *Neuroimage* 154 (2017), pp. 128–149.

[26] John Ashburner et al. "SPM12 manual". In: *Wellcome Trust Centre for Neuroimaging, London, UK* (2014), p. 2464.

[27] Theodore D Satterthwaite et al. "An improved framework for confound regression and filtering for control of motion artifact in the preprocessing of resting-state functional connectivity data". In: *Neuroimage* 64 (2013), pp. 240–256.

[28] Yan Chao-Gan and Zang Yu-Feng. "DPARSF: a MATLAB toolbox for "pipeline" data analysis of resting-state fMRI". In: *Frontiers in systems neuroscience* 4 (2010).

[29] Michael G Hart, Stephen J Price, and John Suckling. "Connectome analysis for pre-operative brain mapping in neurosurgery". In: *British journal of neurosurgery* 30.5 (2016), pp. 506–517.

[30] Mikail Rubinov and Olaf Sporns. "Complex network measures of brain connectivity: uses and interpretations". In: *Neuroimage* 52.3 (2010), pp. 1059–1069.

[31] Mite Mijalkov et al. "BRAPH: a graph theory software for the analysis of brain connectivity". In: *PloS one* 12.8 (2017).

[32] Yongqiang Yu et al. "Small-world brain network and dynamic functional distribution in patients with subcortical vascular cognitive impairment". In: *PloS one* 10.7 (2015).

[33] Yifei Zhu et al. "Disrupted brain connectivity networks in acute ischemic stroke patients". In: *Brain imaging and behavior* 11.2 (2017), pp. 444–453.

[34] Wouter De Baene, Geert-Jan M Rutten, and Margriet M Sitskoorn. "Cognitive functioning in glioma patients is related to functional connectivity measures of the non-tumoural hemisphere". In: *European Journal of Neuroscience* 50.12 (2019), pp. 3921–3933.

[35] Linqiong Sang et al. "Progressively disrupted brain functional connectivity network in subcortical ischemic vascular cognitive impairment patients". In: *Frontiers in neurology* 9 (2018), p. 94.

[36] Mite Mijalkov et al. *BRAPH 1.0.0*. Braph.org, 2016.

[37] Ben J Harrison et al. “Consistency and functional specialization in the default mode brain network”. In: *Proceedings of the National Academy of Sciences* 105.28 (2008), pp. 9781–9786.

[38] Ji Eun Park et al. “Alteration of long-distance functional connectivity and network topology in patients with supratentorial gliomas”. In: *Neuroradiology* 58.3 (2016), pp. 311–320.

[39] Qingling Huang et al. “Disturbed small-world networks and neurocognitive function in frontal lobe low-grade glioma patients”. In: *PLoS One* 9.4 (2014).

[40] Jinfang Wang et al. “The role of disturbed small-world networks in patients with white matter lesions and cognitive impairment revealed by resting state function magnetic resonance images (rs-fMRI)”. In: *Medical science monitor: international medical journal of experimental and clinical research* 25 (2019), p. 341.

[41] JD Kruschwitz et al. “GraphVar: a user-friendly toolbox for comprehensive graph analyses of functional brain connectivity”. In: *Journal of neuroscience methods* 245 (2015), pp. 107–115.

[42] Jinhui Wang et al. “GRETNA: a graph theoretical network analysis toolbox for imaging connectomics”. In: *Frontiers in human neuroscience* 9 (2015), p. 386.

[43] Misun Yoon and Hae-Jeong Park. “Multimodal brain NETwork analysis Toolbox (MNET) *Software User’s Manual Version 1.1*”. In: (2013).

[44] Alex Fornito, Andrew Zalesky, and Edward T Bullmore. “Network scaling effects in graph analytic studies of human resting-state FMRI data”. In: *Frontiers in systems neuroscience* 4 (2010), p. 22.

[45] JP Verma and Abdel-Salam G Abdel-Salam. *Testing statistical assumptions in research*. John Wiley & Sons, 2019, p. 67.

[46] Thomas W MacFarland and Jan M Yates. “Wilcoxon matched-pairs signed-ranks test”. In: *Introduction to Nonparametric statistics for the biological sciences using R*. Springer, 2016, pp. 133–175.

[47] Henry Hsu and Peter A Lachenbruch. “Paired t test”. In: *Encyclopedia of Biostatistics* 6 (2005).

Appendix A

Nodal results

This appendix intends to present the nodal graph theory results and represent them in the corresponding hemispheric-brain view for both lesioned and non lesioned networks, when thresholding them at a range of proportional thresholds from 20% to 40% with increments of 5%. It also aims to exhibit their corresponding nodal statistical results.

A.1 Graph Theory Analysis

In this section the nodal results from graph theory analysis will be exploit, including the mean and median values for both the global efficiency and clustering coefficient graph measures. Further, their mean values will be represented in a sagittal brain-view for both networks thresholded at each proportional threshold.

	Proportional threshold									
	20%		25%		30%		35%		40%	
Regions	**Lesioned**	**Non lesioned**	**Lesioned**	**Non lesioned**	**Lesioned**	**Non lesioned**	**Lesioned**	**Non lesioned**	**Lesioned**	**Non lesioned**
PreCG	0.539±0.102	0.539±0.096	0.598±0.098	0.603±0.084	0.658±0.078	0.646±0.090	0.704±0.069	0.682±0.082	0.740±0.079	0.718±0.077
SFGdor	0.386±0.227	0.574±0.070	0.452±0.218	0.621±0.075	0.484±0.231	0.660±0.080	0.573±0.152	0.719±0.082	0.615±0.152	0.752±0.089
ORBsup	0.387±0.208	0.353±0.193	0.436±0.235	0.394±0.213	0.471±0.255	0.424±0.227	0.557±0.158	0.453±0.236	0.579±0.154	0.482±0.244
MFG	0.403±0.260	0.539±0.073	0.519±0.160	0.586±0.079	0.563±0.154	0.631±0.068	0.610±0.133	0.668±0.058	0.660±0.115	0.701±0.056
ORBmid	0.335±0.201	0.392±0.098	0.383±0.201	0.436±0.113	0.431±0.214	0.476±0.115	0.465±0.224	0.522±0.102	0.505±0.239	0.557±0.101
IFGoperc	0.434±0.140	0.529±0.072	0.509±0.100	0.582±0.066	0.569±0.082	0.633±0.053	0.620±0.078	0.674±0.048	0.652±0.083	0.709±0.058
IFGtriang	0.469±0.129	0.489±0.103	0.554±0.111	0.532±0.104	0.607±0.101	0.568±0.099	0.650±0.084	0.607±0.103	0.702±0.082	0.651±0.099
ORBinf	0.391±0.218	0.459±0.144	0.485±0.160	0.507±0.137	0.537±0.174	0.555±0.147	0.594±0.161	0.617±0.097	0.656±0.113	0.666±0.087
ROL	0.487±0.114	0.526±0.083	0.550±0.084	0.584±0.079	0.602±0.083	0.623±0.075	0.635±0.096	0.664±0.068	0.695±0.087	0.710±0.056
SMA	0.430±0.152	0.480±0.097	0.502±0.124	0.536±0.095	0.556±0.112	0.584±0.086	0.614±0.129	0.618±0.082	0.664±0.118	0.664±0.084
OLF	0.310±0.235	0.370±0.190	0.353±0.268	0.446±0.112	0.444±0.230	0.488±0.124	0.489±0.248	0.530±0.125	0.608±0.115	0.565±0.111
SFGmed	0.366±0.225	0.502±0.064	0.440±0.211	0.558±0.079	0.478±0.230	0.602±0.073	0.580±0.110	0.630±0.071	0.628±0.093	0.660±0.078
ORBsupmed	0.357±0.157	0.378±0.194	0.454±0.095	0.438±0.142	0.518±0.074	0.503±0.141	0.557±0.078	0.542±0.132	0.607±0.088	0.586±0.113
REC	0.397±0.111	0.398±0.098	0.466±0.129	0.434±0.108	0.502±0.142	0.493±0.093	0.541±0.134	0.536±0.104	0.577±0.133	0.566±0.098
INS	0.433±0.209	0.553±0.080	0.538±0.114	0.602±0.076	0.590±0.107	0.641±0.067	0.653±0.091	0.685±0.062	0.700±0.079	0.719±0.072
ACG	0.439±0.215	0.483±0.087	0.548±0.134	0.513±0.089	0.587±0.122	0.556±0.088	0.630±0.105	0.603±0.098	0.674±0.085	0.636±0.107
DCG	0.457±0.224	0.532±0.242	0.593±0.097	0.643±0.101	0.652±0.083	0.687±0.107	0.710±0.086	0.726±0.102	0.769±0.085	0.756±0.096
PCG	0.456±0.078	0.465±0.210	0.530±0.083	0.517±0.234	0.569±0.085	0.612±0.098	0.617±0.078	0.664±0.092	0.648±0.075	0.696±0.074
HIP	0.340±0.197	0.488±0.042	0.438±0.141	0.551±0.046	0.497±0.105	0.596±0.038	0.557±0.113	0.641±0.035	0.595±0.103	0.686±0.036
PHG	0.316±0.183	0.452±0.091	0.400±0.109	0.501±0.103	0.470±0.110	0.545±0.107	0.509±0.118	0.586±0.109	0.574±0.117	0.633±0.103
AMYG	0.326±0.216	0.357±0.165	0.391±0.214	0.405±0.187	0.434±0.223	0.437±0.204	0.481±0.235	0.507±0.111	0.527±0.249	0.554±0.109
CAL	0.610±0.050	0.624±0.043	0.685±0.043	0.672±0.044	0.722±0.047	0.711±0.037	0.761±0.047	0.756±0.030	0.786±0.039	0.794±0.023
CUN	0.558±0.070	0.563±0.069	0.637±0.021	0.616±0.053	0.693±0.030	0.655±0.062	0.746±0.034	0.701±0.059	0.788±0.030	0.740±0.055
LING	0.565±0.128	0.641±0.058	0.625±0.106	0.694±0.061	0.682±0.081	0.739±0.053	0.731±0.063	0.770±0.044	0.772±0.069	0.796±0.039
SOG	0.483±0.205	0.527±0.129	0.582±0.160	0.567±0.119	0.628±0.146	0.611±0.136	0.681±0.129	0.651±0.132	0.709±0.119	0.688±0.126
MOG	0.502±0.213	0.548±0.087	0.567±0.180	0.606±0.072	0.621±0.183	0.651±0.085	0.700±0.118	0.687±0.071	0.749±0.108	0.719±0.073
IOG	0.533±0.073	0.563±0.054	0.610±0.051	0.620±0.052	0.639±0.051	0.663±0.055	0.681±0.050	0.700±0.050	0.720±0.049	0.730±0.045
FFG	0.595±0.051	0.586±0.082	0.651±0.040	0.639±0.077	0.695±0.034	0.686±0.068	0.748±0.043	0.728±0.077	0.778±0.037	0.769±0.092
PoCG	0.461±0.208	0.534±0.084	0.574±0.104	0.587±0.075	0.617±0.105	0.649±0.076	0.668±0.084	0.688±0.073	0.699±0.079	0.719±0.072
SPG	0.540±0.109	0.548±0.073	0.599±0.112	0.589±0.068	0.639±0.112	0.640±0.064	0.686±0.096	0.679±0.072	0.722±0.108	0.712±0.070
IPL	0.508±0.098	0.510±0.068	0.578±0.075	0.584±0.067	0.630±0.059	0.635±0.059	0.669±0.077	0.667±0.064	0.706±0.080	0.703±0.069
SMG	0.489±0.054	0.562±0.045	0.566±0.065	0.627±0.045	0.624±0.058	0.666±0.059	0.669±0.059	0.704±0.066	0.720±0.053	0.740±0.049
ANG	0.452±0.064	0.541±0.093	0.508±0.071	0.592±0.087	0.562±0.069	0.631±0.101	0.601±0.084	0.676±0.096	0.648±0.080	0.712±0.092
PCUN	0.562±0.094	0.588±0.055	0.630±0.086	0.650±0.047	0.679±0.072	0.696±0.045	0.733±0.062	0.734±0.039	0.772±0.048	0.769±0.019
PCL	0.378±0.191	0.441±0.139	0.440±0.220	0.521±0.117	0.532±0.132	0.566±0.126	0.582±0.118	0.594±0.133	0.629±0.124	0.630±0.132
CAU	0.323±0.240	0.385±0.209	0.379±0.265	0.498±0.132	0.481±0.244	0.537±0.132	0.526±0.265	0.575±0.146	0.623±0.147	0.620±0.114
PUT	0.385±0.138	0.512±0.082	0.493±0.110	0.573±0.055	0.556±0.097	0.624±0.053	0.616±0.097	0.667±0.058	0.661±0.096	0.703±0.056
PAL	0.247±0.127	0.375±0.086	0.332±0.172	0.433±0.080	0.361±0.179	0.476±0.098	0.400±0.201	0.512±0.103	0.516±0.101	0.556±0.094
THA	0.220±0.215	0.468±0.067	0.262±0.250	0.521±0.085	0.348±0.256	0.583±0.090	0.499±0.108	0.620±0.088	0.555±0.087	0.660±0.097
HES	0.311±0.160	0.498±0.101	0.376±0.180	0.540±0.110	0.433±0.202	0.592±0.121	0.489±0.235	0.630±0.112	0.540±0.254	0.671±0.096
STG	0.517±0.105	0.609±0.058	0.585±0.094	0.667±0.059	0.644±0.074	0.711±0.061	0.699±0.072	0.744±0.061	0.740±0.062	0.783±0.059
TPOsup	0.441±0.149	0.409±0.238	0.532±0.104	0.508±0.165	0.594±0.107	0.555±0.167	0.642±0.110	0.623±0.107	0.683±0.112	0.669±0.105
MTG	0.610±0.061	0.642±0.061	0.674±0.041	0.690±0.060	0.726±0.039	0.737±0.055	0.762±0.041	0.779±0.046	0.803±0.041	0.814±0.042
TPOmid	0.383±0.100	0.254±0.241	0.442±0.115	0.333±0.232	0.491±0.122	0.360±0.250	0.527±0.127	0.387±0.270	0.578±0.118	0.424±0.292
ITG	0.577±0.069	0.579±0.110	0.642±0.065	0.635±0.091	0.692±0.057	0.683±0.098	0.746±0.045	0.724±0.098	0.781±0.045	0.767±0.098

Table A.1: Global efficiency mean values of each node in both lesioned and non lesioned hemispheres whose networks were thresholded at a range of proportional threshold from 20% to 40% with increments of 5%. Region names are omitted but referred in Table 3.2 in Methods. Data are presented as mean±standard deviation.

	Proportional threshold									
	20%		25%		30%		35%		40%	
Regions	**Lesioned**	**Non lesioned**	**Lesioned**	**Non lesioned**	**Lesioned**	**Non lesioned**	**Lesioned**	**Non lesioned**	**Lesioned**	**Non lesioned**
PreCG	0.541	0.541	0.634	0.609	0.683	0.633	0.708	0.709	0.748	0.732
SFGdor	0.501	0.552	0.550	0.613	0.571	0.660	0.626	0.713	0.679	0.732
ORBsup	0.475	0.361	0.546	0.378	0.586	0.456	0.602	0.497	0.623	0.536
MFG	0.406	0.533	0.497	0.600	0.553	0.642	0.585	0.687	0.626	0.719
ORBmid	0.336	0.371	0.389	0.404	0.430	0.464	0.491	0.525	0.553	0.581
IFGoperc	0.418	0.518	0.514	0.578	0.580	0.603	0.653	0.648	0.679	0.686
IFGtriang	0.502	0.450	0.604	0.495	0.648	0.553	0.682	0.621	0.730	0.689
ORBinf	0.510	0.480	0.535	0.542	0.616	0.586	0.645	0.628	0.679	0.675
ROL	0.482	0.540	0.527	0.601	0.569	0.664	0.585	0.697	0.676	0.732
SMA	0.484	0.490	0.538	0.551	0.553	0.601	0.623	0.626	0.676	0.667
OLF	0.358	0.393	0.401	0.439	0.426	0.495	0.560	0.553	0.651	0.585
SFGmed	0.493	0.510	0.527	0.538	0.552	0.598	0.568	0.601	0.591	0.628
ORBsupmed	0.395	0.472	0.473	0.494	0.550	0.551	0.586	0.579	0.642	0.607
REC	0.354	0.403	0.419	0.443	0.450	0.484	0.500	0.551	0.541	0.577
INS	0.492	0.585	0.571	0.638	0.621	0.658	0.667	0.713	0.730	0.735
ACG	0.506	0.504	0.605	0.533	0.634	0.571	0.646	0.635	0.673	0.670
DCG	0.528	0.609	0.619	0.664	0.668	0.694	0.730	0.745	0.792	0.779
PCG	0.463	0.538	0.502	0.616	0.549	0.664	0.597	0.697	0.654	0.713
HIP	0.392	0.494	0.452	0.566	0.505	0.613	0.552	0.650	0.615	0.691
PHG	0.354	0.489	0.391	0.541	0.483	0.585	0.524	0.649	0.597	0.689
AMYG	0.312	0.409	0.375	0.454	0.450	0.501	0.533	0.534	0.604	0.556
CAL	0.607	0.634	0.675	0.677	0.709	0.710	0.748	0.738	0.770	0.794
CUN	0.594	0.546	0.638	0.622	0.692	0.658	0.747	0.719	0.786	0.754
LING	0.574	0.647	0.619	0.712	0.686	0.742	0.734	0.766	0.805	0.800
SOG	0.585	0.556	0.627	0.592	0.671	0.664	0.739	0.694	0.755	0.724
MOG	0.555	0.536	0.605	0.600	0.676	0.653	0.736	0.686	0.780	0.705
IOG	0.549	0.589	0.619	0.654	0.638	0.680	0.698	0.689	0.726	0.708
FFG	0.616	0.595	0.657	0.639	0.703	0.692	0.753	0.736	0.799	0.806
PoCG	0.550	0.559	0.626	0.608	0.660	0.661	0.686	0.680	0.717	0.694
SPG	0.566	0.559	0.597	0.606	0.651	0.638	0.704	0.684	0.723	0.702
IPL	0.507	0.530	0.603	0.583	0.647	0.631	0.690	0.669	0.730	0.694
SMG	0.484	0.570	0.593	0.638	0.638	0.683	0.667	0.713	0.711	0.751
ANG	0.421	0.590	0.494	0.619	0.560	0.671	0.564	0.714	0.638	0.743
PCUN	0.549	0.605	0.638	0.658	0.692	0.705	0.744	0.740	0.778	0.770
PCL	0.453	0.447	0.500	0.495	0.524	0.549	0.575	0.604	0.645	0.642
CAU	0.377	0.455	0.511	0.508	0.594	0.570	0.609	0.622	0.623	0.656
PUT	0.354	0.518	0.418	0.574	0.524	0.636	0.572	0.667	0.610	0.726
PAL	0.261	0.355	0.336	0.406	0.375	0.435	0.421	0.485	0.495	0.548
THA	0.330	0.485	0.404	0.537	0.457	0.601	0.508	0.649	0.544	0.713
HES	0.342	0.456	0.431	0.508	0.456	0.561	0.495	0.586	0.558	0.648
STG	0.517	0.630	0.588	0.693	0.660	0.723	0.724	0.751	0.750	0.795
TPOsup	0.471	0.493	0.525	0.555	0.648	0.633	0.675	0.657	0.733	0.721
MTG	0.634	0.650	0.679	0.714	0.726	0.753	0.774	0.801	0.814	0.820
TPOmid	0.364	0.363	0.431	0.411	0.448	0.464	0.481	0.495	0.531	0.557
ITG	0.549	0.634	0.634	0.665	0.682	0.705	0.733	0.740	0.758	0.787

Table A.2: Global efficiency median values of each node in both lesioned and non lesioned hemispheres whose networks were thresholded at a range of proportional threshold from 20% to 40% with increments of 5%. Region names are omitted but referred in Table 3.2 in Methods.

(a) **Lesioned** (b) **Non lesioned**

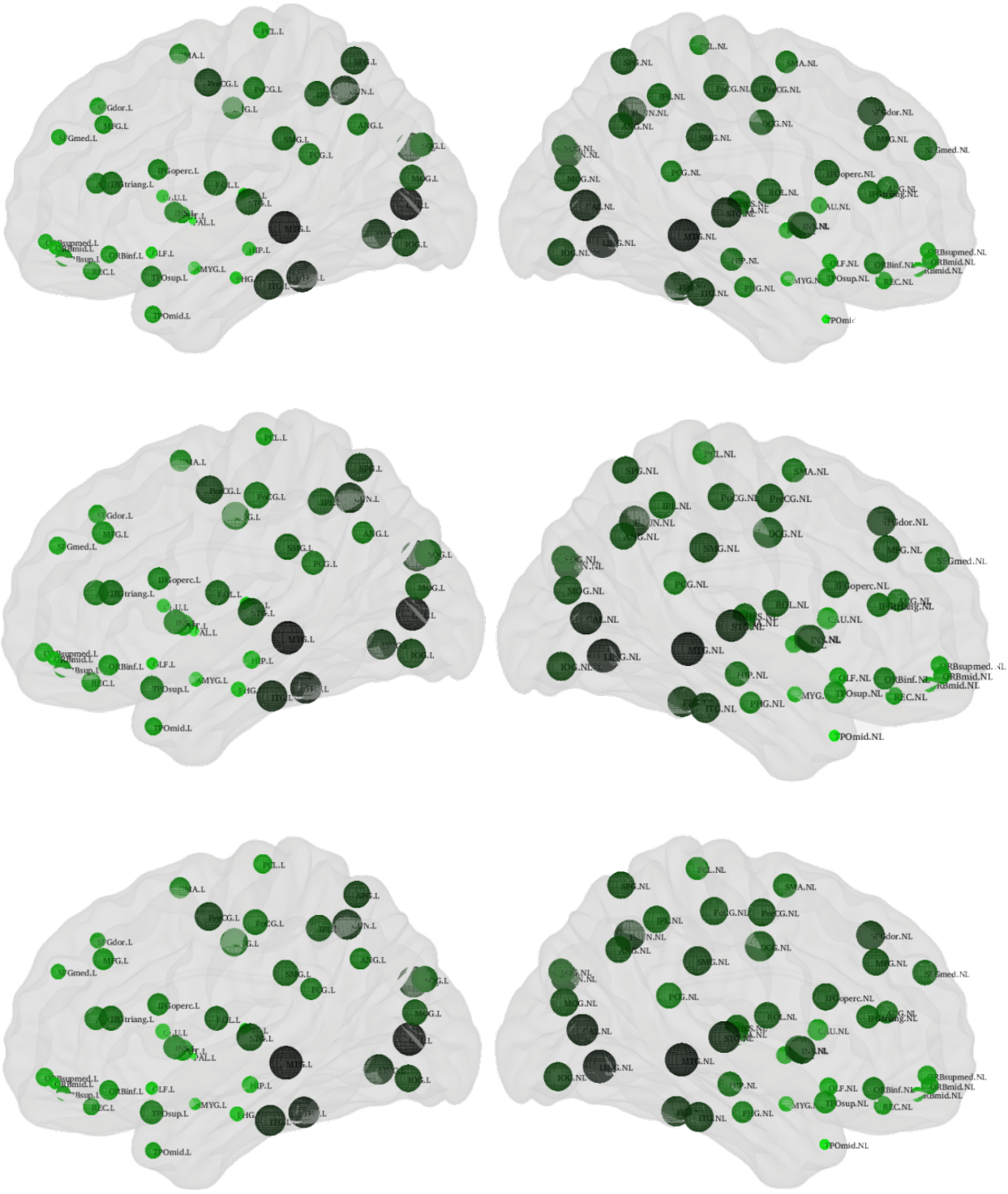

Figure A.1: Nodal global efficiency mean values obtained for lesioned (left) and non lesioned (right) networks when thresholding them at densities of 20% (top), 25% (middle) and 30% (bottom). The results are visualized in a sagittal hemispheric-brain view. Each one of the 45 hemispheric regions is displayed as a sphere along with the corresponding label of its name. Higher/lower values are represented by larger/smaller and darker/clearer spheres, respectively. Region names are omitted but referred in Table 3.2 in Methods.

(a) **Lesioned** (b) **Non lesioned**

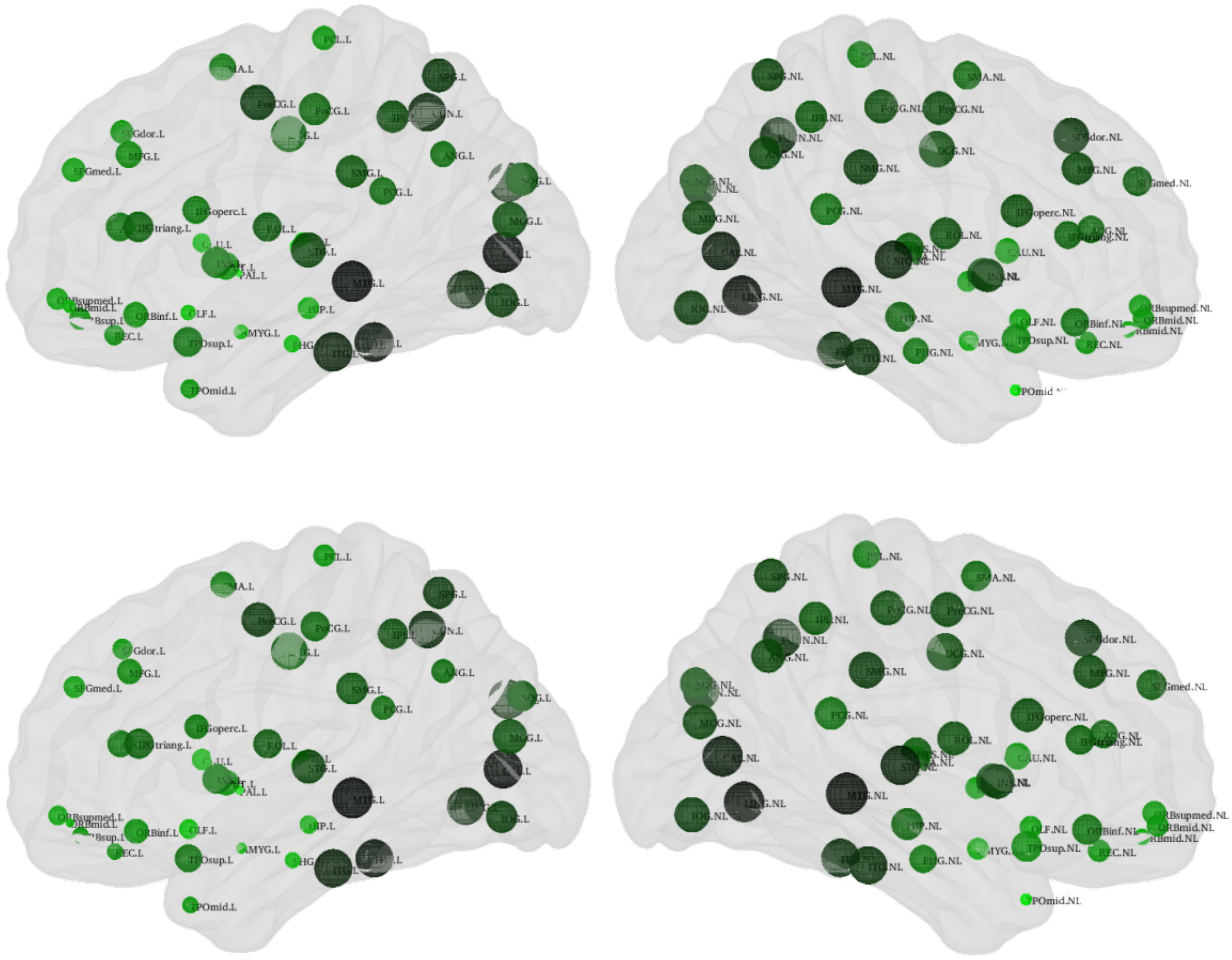

Figure A.2: Nodal global efficiency mean values obtained for lesioned (left) and non lesioned (right) networks when thresholding them at densities of 35% (top) and 40% (bottom). The results are visualized in a sagittal hemispheric-brain view. Each one of the 45 hemispheric regions is displayed as a sphere along with the corresponding label of its name. Higher/lower values are represented by larger/smaller and darker/clearer spheres, respectively. Region names are omitted but referred in Table 3.2 in Methods.

	Proportional threshold									
	20%		25%		30%		35%		40%	
Regions	**Lesioned**	**Non lesioned**	**Lesioned**	**Non lesioned**	**Lesioned**	**Non lesioned**	**Lesioned**	**Non lesioned**	**Lesioned**	**Non lesioned**
PreCG	0.619±0.216	0.522±0.114	0.651±0.204	0.577±0.120	0.641±0.165	0.644±0.137	0.656±0.111	0.686±0.116	0.705±0.091	0.697±0.117
SFGdor	0.530±0.280	0.605±0.094	0.554±0.289	0.656±0.111	0.560±0.287	0.704±0.119	0.717±0.183	0.679±0.092	0.749±0.139	0.702±0.096
ORBsup	0.440±0.342	0.594±0.310	0.649±0.313	0.561±0.271	0.656±0.314	0.593±0.274	0.740±0.161	0.656±0.298	0.788±0.131	0.671±0.311
MFG	0.499±0.274	0.517±0.164	0.489±0.248	0.565±0.067	0.517±0.276	0.639±0.069	0.694±0.202	0.644±0.106	0.600±0.205	0.678±0.108
ORBmid	0.295±0.375	0.633±0.348	0.407±0.350	0.753±0.196	0.522±0.332	0.712±0.160	0.497±0.271	0.712±0.157	0.579±0.283	0.782±0.101
IFGoperc	0.381±0.289	0.641±0.131	0.613±0.091	0.683±0.116	0.630±0.162	0.704±0.075	0.659±0.152	0.713±0.069	0.681±0.136	0.738±0.076
IFGtriang	0.614±0.224	0.744±0.216	0.633±0.208	0.776±0.186	0.718±0.148	0.789±0.156	0.723±0.106	0.813±0.154	0.762±0.102	0.790±0.110
ORBinf	0.434±0.302	0.455±0.220	0.442±0.303	0.517±0.105	0.468±0.325	0.544±0.093	0.728±0.157	0.572±0.076	0.652±0.166	0.602±0.060
ROL	0.711±0.182	0.609±0.099	0.681±0.214	0.655±0.083	0.685±0.161	0.709±0.055	0.732±0.144	0.718±0.096	0.769±0.122	0.727±0.072
SMA	0.692±0.331	0.532±0.265	0.803±0.235	0.577±0.140	0.746±0.157	0.693±0.108	0.759±0.131	0.687±0.120	0.781±0.054	0.712±0.085
OLF	0.446±0.422	0.615±0.367	0.460±0.435	0.663±0.370	0.634±0.439	0.715±0.340	0.608±0.419	0.829±0.116	0.685±0.338	0.845±0.089
SFGmed	0.493±0.319	0.586±0.181	0.558±0.310	0.615±0.162	0.575±0.281	0.651±0.133	0.617±0.172	0.710±0.117	0.647±0.186	0.735±0.132
ORBsupmed	0.478±0.393	0.655±0.359	0.595±0.281	0.677±0.344	0.659±0.223	0.661±0.318	0.652±0.187	0.739±0.203	0.704±0.157	0.793±0.111
REC	0.736±0.289	0.813±0.250	0.765±0.205	0.728±0.284	0.842±0.167	0.759±0.234	0.828±0.126	0.793±0.191	0.843±0.134	0.818±0.151
INS	0.440±0.323	0.538±0.099	0.601±0.137	0.623±0.114	0.624±0.222	0.659±0.097	0.695±0.127	0.664±0.072	0.705±0.134	0.693±0.057
ACG	0.587±0.326	0.733±0.179	0.609±0.309	0.760±0.198	0.664±0.258	0.762±0.171	0.757±0.132	0.745±0.157	0.765±0.108	0.742±0.167
DCG	0.591±0.323	0.516±0.267	0.601±0.185	0.612±0.139	0.700±0.099	0.624±0.118	0.701±0.103	0.668±0.125	0.698±0.091	0.716±0.139
PCG	0.686±0.343	0.592±0.312	0.611±0.309	0.615±0.309	0.801±0.124	0.624±0.304	0.766±0.134	0.639±0.299	0.792±0.155	0.787±0.103
HIP	0.297±0.224	0.606±0.153	0.362±0.257	0.632±0.167	0.550±0.150	0.667±0.151	0.634±0.118	0.698±0.142	0.664±0.078	0.705±0.129
PHG	0.573±0.455	0.638±0.314	0.583±0.462	0.647±0.319	0.565±0.315	0.657±0.324	0.662±0.313	0.644±0.315	0.668±0.181	0.701±0.121
AMYG	0.485±0.463	0.473±0.374	0.579±0.412	0.589±0.336	0.727±0.341	0.634±0.353	0.708±0.320	0.643±0.357	0.678±0.322	0.852±0.132
CAL	0.609±0.136	0.606±0.089	0.621±0.158	0.649±0.081	0.670±0.165	0.675±0.056	0.693±0.152	0.684±0.070	0.721±0.140	0.684±0.047
CUN	0.694±0.146	0.630±0.090	0.695±0.108	0.658±0.102	0.714±0.109	0.686±0.116	0.712±0.092	0.692±0.118	0.720±0.083	0.694±0.106
LING	0.670±0.224	0.533±0.085	0.716±0.220	0.575±0.096	0.721±0.168	0.602±0.089	0.723±0.136	0.638±0.069	0.722±0.118	0.672±0.049
SOG	0.641±0.317	0.527±0.263	0.587±0.221	0.584±0.207	0.654±0.186	0.598±0.198	0.675±0.125	0.656±0.106	0.698±0.141	0.661±0.125
MOG	0.525±0.289	0.691±0.138	0.561±0.287	0.678±0.097	0.550±0.277	0.715±0.093	0.614±0.162	0.717±0.127	0.630±0.138	0.720±0.115
IOG	0.757±0.137	0.677±0.095	0.746±0.128	0.701±0.099	0.797±0.106	0.723±0.074	0.812±0.102	0.751±0.068	0.815±0.108	0.765±0.054
FFG	0.621±0.122	0.556±0.123	0.641±0.157	0.594±0.116	0.664±0.151	0.603±0.098	0.692±0.138	0.625±0.101	0.708±0.129	0.645±0.073
PoCG	0.628±0.314	0.588±0.242	0.653±0.328	0.651±0.118	0.726±0.138	0.632±0.105	0.712±0.169	0.678±0.116	0.769±0.132	0.715±0.104
SPG	0.666±0.118	0.637±0.098	0.731±0.124	0.665±0.106	0.775±0.121	0.699±0.079	0.764±0.114	0.721±0.075	0.778±0.131	0.729±0.099
IPL	0.632±0.162	0.724±0.226	0.647±0.131	0.722±0.165	0.659±0.125	0.705±0.124	0.705±0.117	0.753±0.088	0.728±0.114	0.755±0.084
SMG	0.745±0.127	0.674±0.081	0.743±0.127	0.683±0.082	0.757±0.134	0.718±0.100	0.796±0.111	0.737±0.100	0.791±0.102	0.768±0.096
ANG	0.877±0.121	0.624±0.165	0.778±0.102	0.711±0.085	0.786±0.109	0.743±0.077	0.801±0.076	0.719±0.092	0.784±0.067	0.731±0.100
PCUN	0.634±0.204	0.575±0.101	0.621±0.118	0.595±0.085	0.615±0.119	0.625±0.076	0.651±0.094	0.637±0.078	0.671±0.083	0.663±0.096
PCL	0.664±0.363	0.403±0.300	0.729±0.329	0.613±0.309	0.737±0.331	0.780±0.128	0.901±0.065	0.811±0.112	0.860±0.075	0.839±0.130
CAU	0.461±0.459	0.549±0.395	0.557±0.396	0.692±0.321	0.531±0.378	0.821±0.103	0.673±0.325	0.804±0.144	0.675±0.339	0.835±0.118
PUT	0.413±0.397	0.544±0.133	0.443±0.346	0.636±0.073	0.595±0.207	0.684±0.092	0.652±0.153	0.669±0.107	0.705±0.090	0.705±0.095
PAL	0.414±0.518	0.460±0.463	0.356±0.401	0.855±0.184	0.447±0.430	0.874±0.166	0.492±0.465	0.906±0.131	0.869±0.135	0.866±0.107
THA	0.210±0.360	0.619±0.308	0.277±0.353	0.751±0.176	0.402±0.389	0.699±0.135	0.485±0.380	0.736±0.118	0.688±0.218	0.759±0.123
HES	0.775±0.369	0.651±0.270	0.736±0.342	0.721±0.150	0.757±0.344	0.724±0.135	0.700±0.321	0.759±0.133	0.703±0.319	0.779±0.139
STG	0.582±0.128	0.540±0.063	0.603±0.134	0.571±0.060	0.632±0.155	0.603±0.072	0.655±0.140	0.649±0.084	0.698±0.145	0.646±0.105
TPOsup	0.660±0.228	0.361±0.260	0.596±0.103	0.382±0.268	0.637±0.109	0.639±0.173	0.680±0.076	0.574±0.111	0.703±0.088	0.641±0.091
MTG	0.540±0.139	0.483±0.036	0.589±0.126	0.524±0.052	0.624±0.114	0.558±0.073	0.660±0.129	0.577±0.079	0.674±0.119	0.605±0.056
TPOmid	0.406±0.465	0.236±0.370	0.466±0.437	0.326±0.343	0.619±0.396	0.472±0.409	0.671±0.357	0.506±0.401	0.731±0.158	0.491±0.353
ITG	0.589±0.132	0.528±0.067	0.627±0.112	0.558±0.118	0.665±0.115	0.598±0.087	0.673±0.142	0.607±0.081	0.696±0.128	0.620±0.064

Table A.3: Clustering coefficient mean values of each node in both lesioned and non lesioned hemispheres whose networks were thresholded at a range of proportional threshold from 20% to 40% with increments of 5%. Region names are omitted but referred in Table 3.2 in Methods. Data are presented as mean±standard deviation.

	Proportional threshold									
	20%		25%		30%		35%		40%	
Regions	**Lesioned**	**Non lesioned**	**Lesioned**	**Non lesioned**	**Lesioned**	**Non lesioned**	**Lesioned**	**Non lesioned**	**Lesioned**	**Non lesioned**
PreCG	0.641	0.510	0.615	0.550	0.632	0.643	0.632	0.713	0.677	0.754
SFGdor	0.528	0.616	0.667	0.697	0.545	0.744	0.752	0.711	0.710	0.744
ORBsup	0.475	0.621	0.758	0.638	0.754	0.667	0.781	0.762	0.808	0.736
MFG	0.550	0.523	0.571	0.549	0.587	0.613	0.628	0.628	0.636	0.664
ORBmid	0.000	0.667	0.333	0.727	0.527	0.676	0.500	0.691	0.657	0.736
IFGoperc	0.472	0.643	0.600	0.722	0.668	0.686	0.650	0.720	0.692	0.723
IFGtriang	0.636	0.606	0.700	0.762	0.702	0.765	0.733	0.795	0.787	0.775
ORBinf	0.600	0.500	0.608	0.527	0.658	0.515	0.698	0.528	0.717	0.589
ROL	0.778	0.603	0.694	0.667	0.682	0.688	0.758	0.706	0.745	0.722
SMA	0.762	0.524	0.861	0.607	0.761	0.721	0.743	0.742	0.778	0.750
OLF	0.667	0.636	0.689	0.736	0.867	0.800	0.810	0.810	0.824	0.833
SFGmed	0.429	0.649	0.600	0.625	0.644	0.671	0.628	0.703	0.683	0.744
ORBsupmed	0.467	0.756	0.600	0.818	0.758	0.721	0.725	0.779	0.712	0.800
REC	0.842	0.934	0.786	0.860	0.840	0.857	0.872	0.905	0.877	0.870
INS	0.527	0.567	0.622	0.610	0.649	0.654	0.695	0.648	0.708	0.706
ACG	0.667	0.814	0.623	0.844	0.649	0.818	0.713	0.797	0.778	0.768
DCG	0.622	0.586	0.569	0.667	0.738	0.624	0.665	0.662	0.704	0.706
PCG	0.788	0.600	0.667	0.680	0.810	0.724	0.736	0.776	0.794	0.818
HIP	0.381	0.667	0.464	0.709	0.556	0.684	0.603	0.738	0.658	0.788
PHG	0.733	0.697	0.773	0.752	0.600	0.752	0.791	0.714	0.750	0.741
AMYG	0.708	0.600	0.714	0.578	0.867	0.750	0.818	0.760	0.782	0.877
CAL	0.681	0.645	0.655	0.653	0.674	0.694	0.698	0.692	0.760	0.690
CUN	0.708	0.641	0.661	0.628	0.697	0.640	0.664	0.683	0.710	0.684
LING	0.663	0.508	0.775	0.570	0.754	0.602	0.768	0.656	0.764	0.658
SOG	0.643	0.603	0.553	0.631	0.655	0.627	0.667	0.639	0.669	0.665
MOG	0.621	0.619	0.593	0.684	0.612	0.714	0.589	0.688	0.589	0.695
IOG	0.803	0.667	0.801	0.697	0.801	0.726	0.773	0.755	0.755	0.778
FFG	0.667	0.570	0.721	0.659	0.682	0.567	0.661	0.573	0.678	0.642
PoCG	0.674	0.624	0.772	0.678	0.711	0.626	0.679	0.688	0.714	0.715
SPG	0.626	0.649	0.714	0.636	0.745	0.692	0.735	0.697	0.764	0.708
IPL	0.603	0.818	0.610	0.775	0.629	0.712	0.680	0.758	0.725	0.710
SMG	0.708	0.691	0.742	0.684	0.709	0.722	0.800	0.751	0.806	0.764
ANG	0.855	0.619	0.756	0.739	0.743	0.786	0.805	0.710	0.794	0.737
PCUN	0.589	0.581	0.627	0.602	0.634	0.643	0.653	0.639	0.640	0.691
PCL	0.800	0.564	0.810	0.644	0.850	0.783	0.909	0.792	0.843	0.800
CAU	0.511	0.649	0.683	0.783	0.667	0.800	0.707	0.830	0.752	0.834
PUT	0.600	0.524	0.564	0.626	0.576	0.731	0.654	0.648	0.719	0.699
PAL	0.000	0.500	0.167	1.000	0.600	1.000	0.800	1.000	0.909	0.857
THA	0.000	0.694	0.000	0.731	0.509	0.667	0.636	0.674	0.643	0.778
HES	1.000	0.614	0.806	0.667	0.833	0.701	0.800	0.744	0.779	0.727
STG	0.610	0.571	0.616	0.571	0.667	0.612	0.683	0.621	0.713	0.653
TPOsup	0.681	0.458	0.600	0.468	0.667	0.571	0.672	0.577	0.661	0.635
MTG	0.514	0.471	0.609	0.529	0.595	0.561	0.613	0.592	0.664	0.591
TPOmid	0.167	0.000	0.333	0.321	0.673	0.500	0.735	0.611	0.700	0.564
ITG	0.634	0.520	0.581	0.569	0.662	0.571	0.654	0.578	0.702	0.607

Table A.4: Clustering coefficient median values of each node in both lesioned and non lesioned hemispheres whose networks were thresholded at a range of proportional threshold from 20% to 40% with increments of 5%. Region names are omitted but referred in Table 3.2 in Methods.

(a) **Lesioned** (b) **Non lesioned**

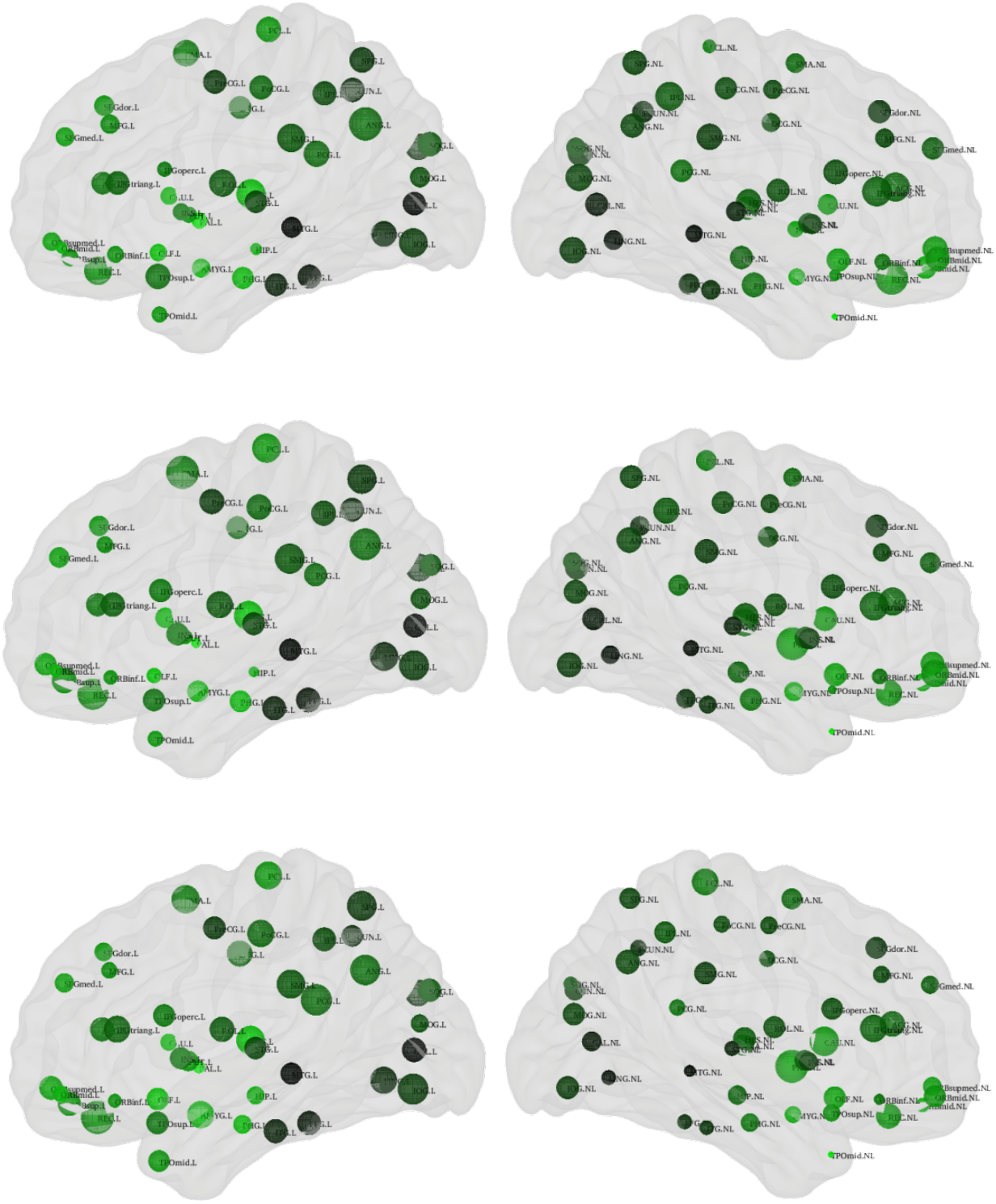

Figure A.3: Nodal clustering coefficient mean values obtained for lesioned (left) and non lesioned (right) networks when thresholding them at densities of 20% (top), 25% (middle) and 30% (bottom). The results are visualized in a sagittal hemispheric-brain view. Each one of the 45 hemispheric regions is displayed as a sphere along with the corresponding label of its name. Higher/lower values are represented by larger/smaller and darker/clearer spheres, respectively. Region names are omitted but referred in Table 3.2 in Methods.

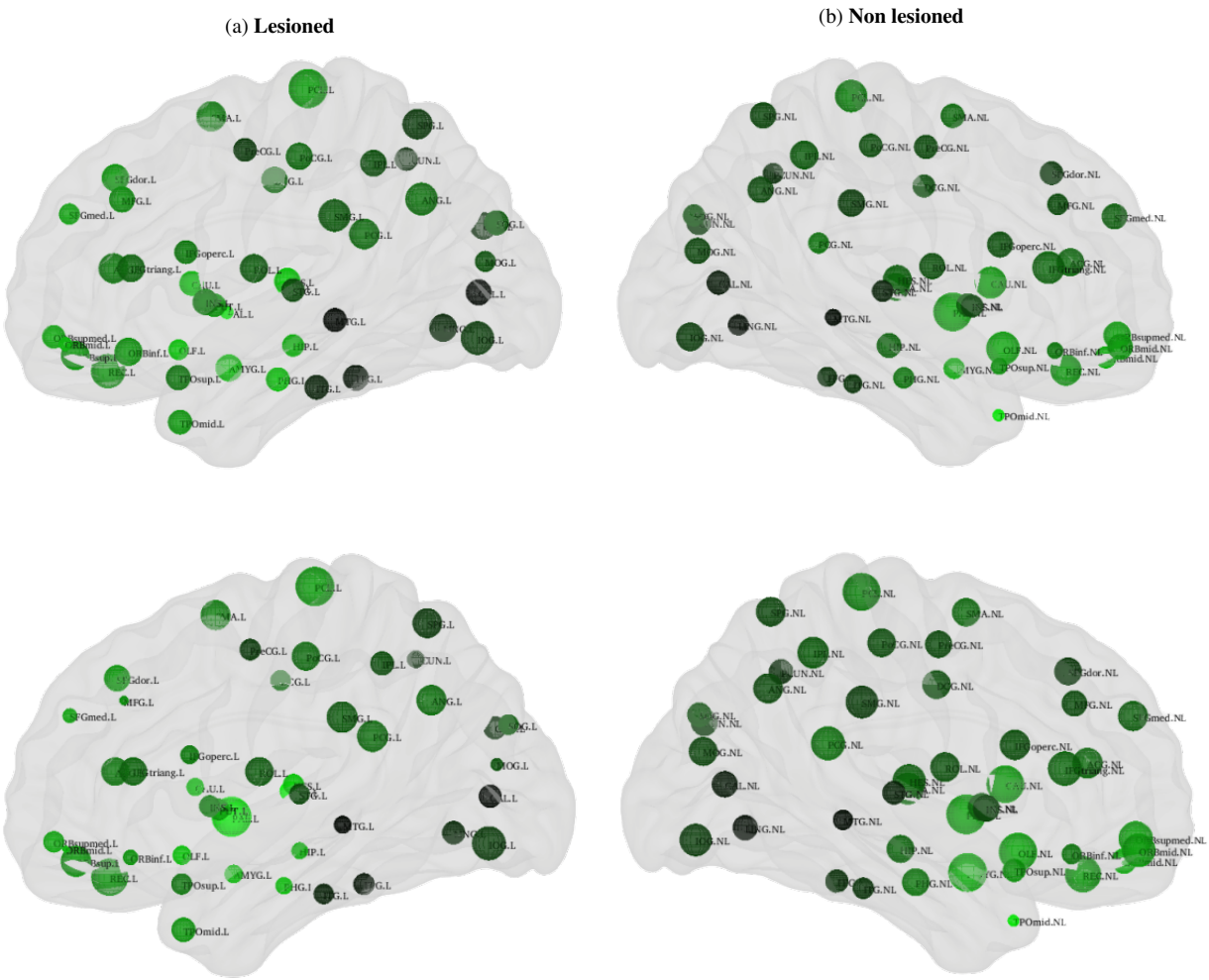

Figure A.4: Nodal clustering coefficient mean values obtained for lesioned (left) and non lesioned (right) networks when thresholding them at densities of 35% (top) and 40% (bottom). The results are visualized in a sagittal hemispheric-brain view. Each one of the 45 hemispheric regions is displayed as a sphere along with the corresponding label of its name. Higher/lower values are represented by larger/smaller and darker/clearer spheres, respectively. Region names are omitted but referred in Table 3.2 in Methods.

A.2 Statistical Analysis

This section intends to present the results obtained when the nodal graph measures were statistically analysed, as described in Section 3.4 of Methods. For the between-threshold comparison, the statistical results are presented in Subsection A.2.1, while the results from the between-hemispheres comparison are displayed in Subsection A.2.2.

A.2.1 Comparison of graph metrics between proportional thresholds, for each hemisphere

The normality nodal results obtained in respect to this between-threshold comparison of global efficiency are displayed in Tables A.5 and A.6, respectively for lesioned and non lesioned hemispheres. The suitable selection of the comparison test can vary between the two-sample paired t test and the Wilcoxon matched pairs test. Resorting to these test, between-threshold comparisons could be performed. These results are shown in Tables A.7 and A.8, respectively for the lesioned and non lesioned hemispheres,

including the selected test.

Analogously, the results from the normality testing for the nodal clustering coefficient are indicated in Tables A.9 (lesioned hemisphere) and A.10 (non lesioned hemisphere). Moreover, the results from the comparison between densities as well as the information involving the test that was selected to performed it are displayed in Tables A.11 and A.12, respectively for lesioned and non lesioned hemispheres.

	Proportional threshold			
Regions	**20%-25%**	**25%-30%**	**30%-35%**	**35%-40%**
PreCG	0.549	0.019*	0.487	0.695
SFGdor	0.019*	0.433	2.125E-04*	0.211
ORBsup	0.008*	0.836	0.001*	0.075
MFG	0.399	0.983	0.178	0.030*
ORBmid	0.420	0.171	0.814	0.294
IFGoperc	0.386	0.722	0.341	0.289
IFGtriang	0.114	0.426	0.986	0.005*
ORBinf	0.002*	0.253	0.002*	0.018*
ROL	0.004*	0.526	0.471	0.406
SMA	0.347	0.952	0.628	0.534
OLF	0.467	1.819E-04*	0.149	0.004*
SFGmed	0.076	0.631	4.331E-05*	0.246
ORBsupmed	0.001*	0.596	0.614	0.464
REC	0.841	0.788	0.975	0.928
INS	3.732E-05*	0.566	0.060	0.053
ACG	0.003*	0.105	0.010*	0.586
DCG	0.003*	0.786	0.724	0.818
PCG	0.733	0.831	0.018*	0.092
HIP	0.327	0.122	0.402	0.293
PHG	0.025*	0.866	0.082	0.855
AMYG	0.059	0.244	0.476	0.738
CAL	0.347	0.185	0.536	0.332
CUN	0.078	0.556	0.718	0.370
LING	0.346	0.967	0.860	0.819
SOG	0.085	0.300	0.706	0.659
MOG	0.396	0.499	1.964E-04*	0.235
IOG	0.827	0.276	0.173	0.542
FFG	0.953	0.428	0.942	0.881
PoCG	0.003*	0.125	0.544	0.938
SPG	0.759	0.177	0.786	0.159
IPL	0.552	0.422	0.840	0.221
SMG	0.841	0.213	0.199	0.669
ANG	0.312	0.455	0.992	0.014*
PCUN	0.407	0.237	0.214	0.448
PCL	0.960	0.003*	0.485	0.947
CAU	0.039*	0.005*	0.268	4.632E-04*
PUT	0.079	0.773	0.593	0.918
PAL	0.593	0.953	0.601	0.008*
THA	0.155	0.023*	0.004*	0.284
HES	0.774	0.963	0.458	0.897
STG	0.617	0.206	0.345	0.061
TPOsup	0.073	0.316	0.344	0.958
MTG	0.015*	0.207	0.212	0.941
TPOmid	0.021*	0.415	0.104	0.130
ITG	0.550	0.168	0.330	0.253

Table A.5: Results from the normality test for the between-threshold comparison of the nodal global efficiency, for the lesioned hemisphere. The values refer to the *P* value obtained from the application of Shapiro-Wilk's test. * indicates *P* value < 0.05 which represents statistical significance. Regions names are omitted but referred in Table 3.2 in Methods.

	Proportional threshold			
Regions	**20%-25%**	**25%-30%**	**30%-35%**	**35%-40%**
PreCG	0.340	0.042*	0.755	0.046*
SFGdor	0.997	0.907	0.592	0.265
ORBsup	0.354	0.563	0.841	0.788
MFG	0.728	0.741	0.091	0.456
ORBmid	0.772	0.369	0.473	0.043*
IFGoperc	0.192	0.575	0.717	0.663
IFGtriang	0.592	0.662	0.184	0.640
ORBinf	0.332	0.929	0.004*	0.721
ROL	0.298	0.837	0.202	0.604
SMA	0.364	0.815	0.424	0.340
OLF	7.470E-05*	0.552	0.165	0.002*
SFGmed	0.591	0.341	0.853	0.400
ORBsupmed	0.004*	0.279	0.028*	0.021*
REC	0.314	0.076	0.796	0.028*
INS	0.059	0.423	0.580	0.650
ACG	0.266	0.174	0.277	0.170
DCG	1.679E-04*	0.289	0.999	0.222
PCG	0.569	2.744E-04*	0.427	0.182
HIP	0.114	0.285	0.485	0.157
PHG	0.289	0.032*	0.861	0.909
AMYG	0.988	0.952	8.473E-05*	0.629
CAL	0.208	0.440	0.077	0.290
CUN	0.452	0.282	0.347	0.608
LING	0.843	0.158	4.466E-04*	0.870
SOG	0.666	0.240	0.555	0.355
MOG	0.151	0.163	0.161	0.855
IOG	0.534	0.618	0.762	0.930
FFG	0.307	0.159	0.280	0.637
PoCG	0.195	0.579	0.687	0.501
SPG	0.605	0.741	0.306	0.445
IPL	0.417	0.141	0.770	0.533
SMG	0.893	0.555	0.158	0.735
ANG	0.611	0.970	0.291	0.775
PCUN	0.205	0.140	0.634	0.810
PCL	0.193	0.314	0.085	0.795
CAU	2.052E-04*	0.181	0.318	0.260
PUT	0.073	0.545	0.651	0.052
PAL	0.462	0.356	0.483	0.202
THA	0.399	0.914	0.581	0.097
HES	0.420	0.975	0.186	0.666
STG	0.356	0.973	0.540	0.324
TPOsup	3.118E-05*	0.279	0.002*	0.227
MTG	0.565	0.135	0.558	0.538
TPOmid	1.301E-04*	0.296	0.129	0.442
ITG	0.976	0.966	0.926	0.784

Table A.6: Results from the normality test for the between-threshold comparison of the nodal global efficiency, for the non lesioned hemisphere. The values refer to the *P* value obtained from the application of Shapiro-Wilk's test. * indicates *P* value < 0.05 which represents statistical significance. Regions names are omitted but referred in Table 3.2 in Methods.

	Proportional threshold							
	20%-25%		25%-30%		30%-35%		35%-40%	
Regions	**Test**	***p***	**Test**	***p***	**Test**	***p***	**Test**	***p***
PreCG	*t*	9.900E-04*	*W*	0.002*	*t*	0.002*	*t*	0.002*
SFGdor	*W*	9.800E-04*	*t*	9.800E-04*	*W*	5.900E-05*	*t*	2.500E-04*
ORBsup	*W*	9.800E-04*	*t*	9.800E-04*	*W*	5.900E-05*	*t*	2.500E-04*
MFG	*t*	3.700E-04*	*t*	3.800E-05*	*t*	7.000E-05*	*W*	7.000E-05*
ORBmid	*t*	0.013*	*t*	0.013*	*t*	0.013*	*t*	0.013*
IFGoperc	*t*	0.004*	*t*	9.900E-04*	*t*	5.600E-04*	*t*	2.000E-04*
IFGtriang	*t*	0.004*	*t*	0.004*	*t*	0.003*	*W*	0.026*
ORBinf	*W*	0.038*	*t*	0.007*	*W*	0.020*	*W*	0.031*
ROL	*W*	0.009*	*t*	0.002*	*t*	0.003*	*t*	0.004*
SMA	*t*	0.007*	*t*	0.003*	*t*	0.001*	*t*	0.002*
OLF	*t*	0.014*	*W*	0.003*	*t*	0.005*	*W*	2.000E-04*
SFGmed	*t*	9.800E-04*	*t*	9.800E-04*	*W*	5.900E-05*	*t*	2.500E-04*
ORBsupmed	*W*	4.500E-05*	*t*	4.500E-05*	*t*	4.500E-05*	*t*	4.500E-05*
REC	*t*	4.500E-05*	*t*	4.500E-05*	*t*	4.500E-05*	*t*	4.500E-05*
INS	*W*	4.500E-05*	*t*	4.500E-05*	*t*	4.500E-05*	*t*	4.500E-05*
ACG	*W*	4.500E-05*	*t*	4.500E-05*	*W*	4.500E-05*	*t*	4.500E-05*
DCG	*W*	4.500E-05*	*t*	4.500E-05*	*t*	4.500E-05*	*t*	4.500E-05*
PCG	*t*	0.002*	*t*	0.002*	*W*	0.001*	*t*	0.010*
HIP	*t*	0.007*	*t*	0.018*	*t*	9.000E-04*	*t*	0.002*
PHG	*W*	0.055	*t*	0.007*	*t*	0.001*	*t*	0.001*
AMYG	*t*	0.013*	*t*	0.013*	*t*	0.013*	*t*	0.013*
CAL	*t*	0.002*	*t*	1.300E-04*	*t*	2.400E-04*	*t*	0.001*
CUN	*t*	0.009*	*t*	0.005*	*t*	2.000E-04*	*t*	2.000E-04*
LING	*t*	0.009*	*t*	0.009*	*t*	0.008*	*t*	0.004*
SOG	*t*	4.000E-05*	*t*	4.000E-05*	*t*	4.000E-05*	*t*	4.000E-05*
MOG	*t*	4.000E-05*	*t*	4.000E-05*	*W*	4.000E-05*	*t*	4.000E-05*
IOG	*t*	0.005*	*t*	0.014*	*t*	0.011*	*t*	4.670E-04*
FFG	*t*	0.005*	*t*	0.003*	*t*	5.400E-04*	*t*	0.001*
PoCG	*W*	4.000E-05*	*t*	4.000E-05*	*t*	4.000E-05*	*t*	4.000E-05*
SPG	*t*	0.004*	*t*	6.400E-04*	*t*	0.003*	*t*	0.003*
IPL	*t*	0.009*	*t*	0.002*	*t*	0.008*	*t*	0.005*
SMG	*t*	0.001*	*t*	6.700E-05*	*t*	0.001*	*t*	5.400E-04*
ANG	*t*	0.003*	*t*	0.003*	*t*	0.009*	*W*	0.002*
PCUN	*t*	0.003*	*t*	5.800E-04*	*t*	4.500E-04*	*t*	0.003*
PCL	*t*	3.700E-04*	*W*	3.800E-05*	*t*	7.000E-05*	*t*	7.000E-05*
CAU	*W*	0.014*	*W*	0.003*	*t*	0.005*	*W*	2.100E-04*
PUT	*t*	0.003*	*t*	0.002*	*t*	7.000E-04*	*t*	0.003*
PAL	*t*	0.004*	*t*	0.004*	*t*	0.004*	*W*	1.800E-04*
THA	*t*	0.030*	*W*	0.004*	*W*	3.500E-05*	*t*	5.800E-04*
HES	*t*	0.013*	*t*	0.013*	*t*	0.013*	*t*	0.013*
STG	*t*	0.009*	*t*	0.010*	*t*	1.200E-04*	*t*	0.001*
TPOsup	*t*	4.000E-05*	*t*	4.000E-05*	*t*	4.000E-05*	*t*	4.000E-05*
MTG	*W*	0.006*	*t*	0.001*	*t*	0.003*	*t*	0.001*
TPOmid	*W*	0.001*	*t*	0.010*	*t*	0.006*	*t*	0.003*
ITG	*t*	3.000E-04*	*t*	0.001*	*t*	0.001*	*t*	0.003*

Table A.7: Results from the comparison of nodal global efficiency between the proportional thresholds of 20%-25%, 25%-30%, 30%-35% and 35%-40%, for the lesioned hemisphere. *p* refers to the *P* value obtained from the application of two-sample paired *t* test and Wilcoxon matched pairs test, respectively represented as *t* and *W*. * indicates *P* value < 0.05 which represents statistical significance. Regions names are omitted but referred in Table 3.2 in Methods.

	Proportional threshold							
	20%-25%		25%-30%		30%-35%		35%-40%	
Regions	**Test**	***p***	**Test**	***p***	**Test**	***p***	**Test**	***p***
PreCG	*t*	2.200E-05*	*W*	0.001*	*t*	0.005*	*W*	0.001*
SFGdor	*t*	3.700E-04*	*t*	2.300E-04*	*t*	0.001*	*t*	2.300E-04*
ORBsup	*t*	0.013*	*t*	0.013*	*t*	0.013*	*t*	0.013*
MFG	*t*	4.000E-04*	*t*	0.001*	*t*	0.004*	*t*	3.400E-05*
ORBmid	*t*	0.002*	*t*	0.006*	*t*	0.006*	*W*	0.006*
IFGoperc	*t*	0.002*	*t*	0.003*	*t*	9.000E-05*	*t*	0.002*
IFGtriang	*t*	0.001*	*t*	6.300E-04*	*t*	0.004*	*t*	0.001*
ORBinf	*t*	0.003*	*t*	0.003*	*W*	0.038*	*t*	4.000E-04*
ROL	*t*	1.500E-04*	*t*	0.005*	*t*	4.200E-04*	*t*	2.700E-04*
SMA	*t*	6.300E-04*	*t*	4.100E-04*	*t*	0.004*	*t*	1.700E-04*
OLF	*W*	4.000E-05*	*t*	4.000E-05*	*t*	4.000E-05*	*W*	4.000E-05*
SFGmed	*t*	0.004*	*t*	0.003*	*t*	0.003*	*t*	7.200E-04*
ORBsupmed	*W*	4.000E-05*	*t*	4.000E-05*	*W*	4.000E-05*	*W*	4.000E-05*
REC	*t*	0.005*	*t*	0.004*	*t*	0.005*	*W*	0.005*
INS	*t*	3.600E-04*	*t*	0.003*	*t*	0.015*	*t*	0.002*
ACG	*t*	0.004*	*t*	0.002*	*t*	0.008*	*t*	0.004*
DCG	*W*	4.000E-05*	*t*	4.000E-05*	*t*	4.000E-05*	*t*	4.000E-05*
PCG	*t*	3.700E-04*	*W*	3.800E-05*	*t*	7.000E-05*	*t*	7.000E-05*
HIP	*t*	3.400E-05*	*t*	0.003*	*t*	0.002*	*t*	3.000E-04*
PHG	*t*	0.002*	*W*	0.008*	*t*	0.005*	*t*	0.006*
AMYG	*t*	9.800E-04*	*t*	9.800E-04*	*W*	5.900E-05*	*t*	2.500E-04*
CAL	*t*	1.900E-04*	*t*	6.400E-04*	*t*	6.400E-04*	*t*	6.400E-04*
CUN	*t*	0.003*	*t*	3.400E-04*	*t*	3.400E-04*	*t*	0.002*
LING	*t*	1.500E-05*	*t*	1.900E-04*	*W*	0.011*	*t*	0.003*
SOG	*t*	0.002*	*t*	0.003*	*t*	2.200E-04*	*t*	0.002*
MOG	*t*	1.700E-04*	*t*	0.001*	*t*	0.014**	*t*	1.700E-04*
IOG	*t*	6.200E-05*	*t*	8.500E-04*	*t*	0.009*	*t*	4.600E-04*
FFG	*t*	7.000E-04*	*t*	7.000E-04*	*t*	7.000E-04*	*t*	0.004*
PoCG	*t*	0.002*	*t*	4.500E-04*	*t*	1.100E-04*	*t*	0.002*
SPG	*t*	2.200E-04*	*t*	5.000E-04*	*t*	0.002*	*t*	0.004*
IPL	*t*	0.002*	*t*	6.700E-05*	*t*	2.300E-04*	*t*	0.001*
SMG	*t*	2.500E-04*	*t*	0.003*	*t*	0.003*	*t*	0.004*
ANG	*t*	7.900E-04*	*t*	0.003*	*t*	9.100E-04*	*t*	0.001*
PCUN	*t*	0.002*	*t*	8.700E-04*	*t*	2.400E-04*	*t*	0.011*
PCL	*t*	0.001*	*t*	3.000E-04*	*t*	0.004*	*t*	6.800E-05*
CAU	*W*	4.000E-05*	*t*	4.000E-05*	*t*	4.000E-05*	*t*	4.000E-05*
PUT	*t*	0.004*	*t*	3.100E-04*	*t*	0.002*	*t*	0.002*
PAL	*t*	0.004*	*t*	0.007*	*t*	0.003*	*t*	0.003*
THA	*t*	6.500E-04*	*t*	3.200E-04*	*t*	0.004*	*t*	0.004*
HES	*t*	0.004*	*t*	0.004*	*t*	0.002*	*t*	0.003*
STG	*t*	0.002*	*t*	0.001*	*t*	0.005*	*t*	0.001*
TPOsup	*W*	4.500E-05*	*t*	4.500E-05*	*W*	4.500E-05*	*t*	4.500E-05*
MTG	*t*	0.006*	*t*	0.001*	*t*	0.004*	*t*	0.003*
TPOmid	*W*	0.070	*t*	0.070	*t*	0.070	*t*	0.070
ITG	*t*	8.800E-04*	*t*	0.002*	*t*	1.700E-04*	*t*	3.100E-04*

Table A.8: Results from the comparison of nodal global efficiency between the proportional thresholds of 20%-25%, 25%-30%, 30%-35% and 35%-40%, for the non lesioned hemisphere. *p* refers to the *P* value obtained from the application of two-sample paired *t* test and Wilcoxon matched pairs test, respectively represented as *t* and *W*. * indicates *P* value < 0.05 which represents statistical significance. Regions names are omitted but referred in Table 3.2 in Methods.

	Proportional threshold			
Regions	**20%-25%**	**25%-30%**	**30%-35%**	**35%-40%**
PreCG	0.183	0.028*	0.763	0.726
SFGdor	0.099	0.292	4.624E-05*	0.567
ORBsup	0.003*	0.351	0.012*	0.039*
MFG	0.281	0.696	1.217E-04*	5.471E-04*
ORBmid	0.158	3.070E-04*	0.003*	0.081
IFGoperc	0.722	0.048*	0.770	0.405
IFGtriang	0.934	0.769	0.213	0.699
ORBinf	0.636	0.667	0.007*	9.354E-05*
ROL	0.006*	0.541	0.381	0.070
SMA	0.761	0.235	0.054	0.975
OLF	0.353	4.568E-05*	0.001*	5.546E-05*
SFGmed	0.003*	0.200	0.020*	0.352
ORBsupmed	0.041*	0.361	0.549	0.681
REC	0.468	0.105	0.036*	0.455
INS	0.259	0.501	2.725E-04*	0.878
ACG	0.579	0.355	3.087E-04*	0.323
DCG	0.046*	0.037*	0.736	0.423
PCG	0.026*	0.001*	0.227	0.250
HIP	0.133	0.227	0.179	0.592
PHG	6.487E-04*	0.952	0.032*	0.001*
AMYG	2.520E-04*	0.004*	0.191	0.045*
CAL	0.409	0.425	0.012*	0.809
CUN	0.161	0.968	0.438	0.765
LING	0.415	0.715	0.360	0.608
SOG	0.091	5.352E-04*	0.882	0.597
MOG	0.151	0.049*	0.016*	0.111
IOG	0.272	0.945	0.994	0.102
FFG	0.499	0.534	0.079	0.338
PoCG	0.387	0.002*	0.049*	0.004*
SPG	0.255	0.096	0.507	0.631
IPL	0.521	0.562	0.029*	0.571
SMG	0.708	0.610	0.991	0.625
ANG	0.217	0.580	0.655	0.445
PCUN	1.938E-04*	0.476	0.541	0.502
PCL	0.021*	0.852	9.092E-05*	0.031*
CAU	0.008*	0.012*	1.039E-04*	0.164
PUT	0.225	0.081	0.191	0.293
PAL	0.592	0.008*	0.015*	0.051
THA	0.005*	0.019*	0.041*	0.121
HES	0.269	0.009*	0.002*	0.692
STG	0.014*	0.848	0.644	0.223
TPOsup	0.620	0.134	0.169	0.721
MTG	0.676	0.369	0.737	0.253
TPOmid	8.280E-05*	3.327E-04*	0.030*	0.037*
ITG	0.723	0.204	0.661	0.736

Table A.9: Results from the normality test for the between-threshold comparison of the nodal clustering coefficient, for the lesioned hemisphere. The values refer to the *P* value obtained from the application of Shapiro-Wilk's test. * indicates *P* value < 0.05 which represents statistical significance. Regions names are omitted but referred in Table 3.2 in Methods.

	Proportional threshold			
Regions	**20%-25%**	**25%-30%**	**30%-35%**	**35%-40%**
PreCG	0.161	0.025*	0.017*	0.683
SFGdor	0.164	0.031*	0.735	0.099
ORBsup	3.534E-04*	0.679	0.049*	0.367
MFG	0.597	0.878	0.509	0.947
ORBmid	0.001*	0.418	0.588	0.588
IFGoperc	0.517	0.701	0.099	0.601
IFGtriang	0.648	0.407	0.218	0.210
ORBinf	0.002*	0.658	0.002*	0.617
ROL	0.075	0.340	0.067	0.642
SMA	0.345	0.028*	0.177	0.259
OLF	0.006*	0.013*	9.668E-04*	0.045*
SFGmed	0.397	0.126	0.774	0.454
ORBsupmed	0.765	0.431	0.017*	5.508E-04*
REC	0.287	0.525	0.057	0.289
INS	0.476	0.943	0.307	0.181
ACG	0.281	0.010*	0.020*	0.096
DCG	0.008*	0.898	0.464	0.137
PCG	0.143	0.542	0.085	6.077E-05*
HIP	0.742	0.536	0.315	0.492
PHG	0.440	0.370	0.932	0.054
AMYG	0.270	0.263	0.135	0.004*
CAL	0.088	0.324	0.126	0.304
CUN	0.904	0.932	0.293	0.587
LING	0.629	0.262	3.151E-04*	0.407
SOG	0.643	0.211	2.815E-05*	0.016*
MOG	0.743	0.083	0.072	0.433
IOG	0.120	0.080	0.051	0.276
FFG	0.393	0.016*	0.219	0.463
PoCG	0.601	0.382	0.214	0.548
SPG	0.048*	0.023*	0.139	0.064
IPL	0.046*	0.001*	0.088	0.015*
SMG	0.673	0.796	0.962	0.985
ANG	0.319	0.302	0.028*	0.290
PCUN	0.427	0.860	0.999	0.984
PCL	0.001*	0.002*	0.551	7.322E-04*
CAU	5.985E-04*	0.003*	0.919	0.548
PUT	0.032*	0.419	0.415	0.199
PAL	0.043*	0.054	0.026*	0.097
THA	4.448E-04*	0.002*	0.234	0.147
HES	0.890	0.524	0.765	0.230
STG	0.236	0.395	0.017*	0.760
TPOsup	0.317	0.005*	1.203E-04*	0.424
MTG	0.124	0.331	0.858	0.108
TPOmid	0.052	1.511E-04*	0.236	0.577
ITG	0.004*	0.077	0.450	0.793

Table A.10: Results from the normality test for the between-threshold comparison of the nodal clustering coefficient, for the non lesioned hemisphere. The values refer to the *P* value obtained from the application of Shapiro-Wilk's test. * indicates *P* value < 0.05 which represents statistical significance. Regions names are omitted but referred in Table 3.2 in Methods.

	Proportional threshold							
	20%-25%		25%-30%		30%-35%		35%-40%	
Regions	**Test**	***p***	**Test**	***p***	**Test**	***p***	**Test**	***p***
PreCG	*t*	0.667	*W*	0.729	*t*	0.729	*t*	0.066
SFGdor	*t*	0.840	*t*	0.840	*W*	0.540	*t*	0.840
ORBsup	*W*	0.127	*t*	0.339	*W*	0.519	*W*	0.127
MFG	*t*	0.720	*t*	0.440	*W*	0.410	*W*	0.460
ORBmid	*t*	0.366	*W*	0.902	*W*	0.366	*t*	0.188
IFGoperc	*t*	0.172	*W*	0.565	*t*	0.474	*t*	0.825
IFGtriang	*t*	0.422	*t*	0.343	*t*	0.845	*t*	0.217
ORBinf	*t*	1.000	*t*	0.320	*W*	9.600E-06*	*W*	0.780
ROL	*W*	0.900	*t*	0.900	*t*	0.650	*t*	0.650
SMA	*t*	0.380	*t*	0.180	*t*	0.740	*t*	0.920
OLF	*t*	0.642	*W*	0.026*	*W*	0.780	*W*	0.191
SFGmed	*W*	0.620	*t*	0.770	*W*	0.690	*t*	0.620
ORBsupmed	*W*	0.646	*t*	0.149	*t*	0.665	*t*	0.555
REC	*t*	1.000	*t*	0.103	*W*	0.797	*t*	0.588
INS	*t*	0.260	*t*	0.346	*W*	0.071	*t*	0.610
ACG	*t*	0.750	*t*	0.210	*W*	0.670	*t*	0.920
DCG	*W*	0.740	*W*	0.740	*t*	0.740	*t*	0.850
PCG	*W*	0.620	*W*	0.620	*t*	0.860	*t*	0.620
HIP	*t*	0.244	*t*	1.200E-04*	*t*	0.138	*t*	0.138
PHG	*W*	0.590	*t*	0.590	*W*	0.290	*W*	0.290
AMYG	*W*	0.920	*W*	0.920	*t*	0.920	*W*	0.920
CAL	*t*	0.502	*t*	0.009*	*W*	0.028*	*t*	0.028*
CUN	*t*	0.990	*t*	0.960	*t*	0.990	*t*	0.960
LING	*t*	0.610	*t*	0.960	*t*	0.960	*t*	0.960
SOG	*t*	0.741	*W*	0.230	*t*	0.648	*t*	0.230
MOG	*t*	1.000	*W*	1.000	*W*	1.000	*t*	1.000
IOG	*t*	0.710	*t*	0.120	*t*	0.530	*t*	0.690
FFG	*t*	0.460	*t*	0.360	*t*	0.360	*t*	0.380
PoCG	*t*	0.149	*W*	0.416	*W*	0.573	*W*	0.149
SPG	*t*	0.009*	*t*	0.271	*t*	0.675	*t*	0.636
IPL	*t*	0.749	*t*	1.000	*W*	0.425	*t*	0.298
SMG	*t*	0.940	*t*	1.000	*t*	0.490	*t*	0.940
ANG	*t*	0.670	*t*	0.950	*t*	0.830	*t*	0.830
PCUN	*W*	0.880	*t*	0.880	*t*	0.360	*t*	0.500
PCL	*W*	0.920	*t*	0.920	*W*	0.320	*W*	0.640
CAU	*W*	0.920	*W*	0.920	*W*	0.920	*t*	0.920
PUT	*t*	0.502	*t*	0.186	*t*	0.502	*t*	0.518
PAL	*t*	0.373	*W*	0.691	*W*	0.468	*t*	0.111
THA	*W*	0.691	*W*	1.000	*W*	0.095	*t*	0.558
HES	*t*	0.904	*W*	0.572	*W*	0.145	*t*	0.699
STG	*W*	0.175	*t*	0.390	*t*	0.116	*t*	0.025*
TPOsup	*t*	0.544	*t*	0.038*	*t*	0.098	*t*	0.483
MTG	*t*	0.065	*t*	0.075	*t*	0.065	*t*	0.277
TPOmid	*W*	0.700	*W*	1.000	*W*	0.830	*W*	0.920
ITG	*t*	0.280	*t*	0.200	*t*	0.640	*t*	0.190

Table A.11: Results from the comparison of nodal clustering coefficient between the proportional thresholds of 20%-25%, 25%-30%, 30%-35% and 35%-40%, for the lesioned hemisphere. *p* refers to the *P* value obtained from the application of two-sample paired *t* test and Wilcoxon matched pairs test, respectively represented as *t* and *W*. * indicates *P* value < 0.05 which represents statistical significance. Regions names are omitted but referred in Table 3.2 in Methods.

	Proportional threshold							
	20%-25%		25%-30%		30%-35%		35%-40%	
Regions	**Test**	***p***	**Test**	***p***	**Test**	***p***	**Test**	***p***
PreCG	*t*	0.002*	*W*	0.145	*W*	0.066	*t*	0.311
SFGdor	*t*	0.056	*W*	0.113	*t*	0.361	*t*	0.056
ORBsup	*W*	0.788	*t*	0.810	*W*	0.077	*t*	0.788
MFG	*t*	0.379	*t*	0.006*	*t*	0.807	*t*	0.006*
ORBmid	*W*	1.000	*t*	0.940	*t*	0.940	*t*	0.940
IFGoperc	*t*	0.210	*t*	0.410	*t*	0.540	*t*	0.210
IFGtriang	*t*	0.680	*t*	0.760	*t*	0.460	*t*	0.630
ORBinf	*W*	0.750	*t*	1.000	*W*	0.260	*t*	0.750
ROL	*t*	0.101	*t*	0.097	*t*	0.644	*t*	0.509
SMA	*t*	0.821	*W*	0.107	*t*	0.624	*t*	0.724
OLF	*W*	0.191	*W*	0.918	*W*	0.918	*W*	0.191
SFGmed	*t*	0.119	*t*	0.783	*t*	0.059	*t*	0.078
ORBsupmed	*t*	0.480	*t*	0.307	*W*	0.307	*W*	0.368
REC	*t*	0.850	*t*	0.920	*t*	0.850	*t*	0.850
INS	*t*	0.128	*t*	0.266	*t*	0.875	*t*	0.151
ACG	*t*	0.530	*W*	0.920	*W*	0.920	*t*	0.920
DCG	*W*	0.897	*t*	0.341	*t*	0.146	*t*	0.079
PCG	*t*	0.747	*t*	0.747	*t*	0.747	*W*	0.236
HIP	*t*	0.202	*t*	0.384	*t*	0.150	*t*	1.000
PHG	*t*	0.840	*t*	0.840	*t*	0.840	*t*	0.840
AMYG	*t*	0.062	*t*	0.900	*t*	0.565	*W*	0.124
CAL	*t*	0.081	*t*	0.189	*t*	0.486	*t*	0.986
CUN	*t*	0.128	*t*	0.104	*t*	0.836	*t*	0.892
LING	*t*	0.012*	*t*	0.064	*W*	0.074	*t*	0.053
SOG	*t*	0.181	*t*	0.511	*W*	0.181	*W*	0.426
MOG	*t*	0.910	*t*	0.380	*t*	0.960	*t*	0.960
IOG	*t*	0.640	*t*	0.460	*t*	0.320	*t*	0.320
FFG	*t*	0.360	*W*	0.710	*t*	0.360	*t*	0.410
PoCG	*t*	1.000	*t*	0.668	*t*	0.010*	*t*	0.109
SPG	*W*	0.370	*W*	0.190	*t*	0.340	*t*	0.690
IPL	*W*	0.950	*W*	0.900	*t*	0.450	*W*	0.950
SMG	*t*	0.769	*t*	0.117	*t*	0.292	*t*	0.031*
ANG	*t*	0.256	*t*	0.589	*W*	1.000	*t*	0.577
PCUN	*t*	0.520	*t*	0.210	*t*	0.430	*t*	0.180
PCL	*W*	0.027*	*W*	0.101	*t*	0.263	*W*	0.455
CAU	*W*	0.580	*W*	0.680	*t*	0.600	*t*	0.580
PUT	*W*	0.127	*t*	0.101	*t*	0.537	*t*	0.051
PAL	*W*	0.500	*t*	0.810	*W*	0.600	*t*	0.820
THA	*W*	0.700	*W*	0.700	*t*	0.700	*t*	0.700
HES	*t*	0.243	*t*	0.535	*t*	0.295	*t*	0.570
STG	*t*	0.211	*t*	0.064	*W*	0.061	*t*	0.848
TPOsup	*t*	0.230	*W*	1.100E-04*	*W*	0.855	*t*	0.045*
MTG	*t*	0.168	*t*	0.156	*t*	0.168	*t*	0.108
TPOmid	*t*	0.900	*W*	0.600	*t*	0.240	*t*	0.600
ITG	*W*	0.394	*t*	0.230	*t*	0.394	*t*	0.520

Table A.12: Results from the comparison of nodal clustering coefficient between the proportional thresholds of 20%-25%, 25%-30%, 30%-35% and 35%-40%, for the non lesioned hemisphere. *p* refers to the *P* value obtained from the application of two-sample paired *t* test and Wilcoxon matched pairs test, respectively represented as *t* and *W*. * indicates *P* value < 0.05 which represents statistical significance. Regions names are omitted but referred in Table 3.2 in Methods.

A.2.2 Comparison of graph metrics between lesioned and non lesioned hemispheres, for each proportional threshold

This subsection intends to present the statistical results for the between-hemispheres comparison of both global efficiency and clustering coefficient nodal metrics. The results from the normality testing are shown in Tables A.13 (nodal global efficiency) and A.15 (nodal clustering coefficient). The tests for the further comparison between both hemispheres also involved the two-sample t test or the Wilcoxon matched pairs test. These results are presented in Tables A.14 and A.16, respectively for nodal global efficiency and clustering coefficient graph metrics. Besides, they included the suitable test that was selected to perform these comparisons.

	Proportional threshold				
Regions	**20%**	**25%**	**30%**	**35%**	**40%**
PreCG	0.224	0.350	0.568	0.540	0.765
SFGdor	0.546	0.246	0.326	0.668	0.540
ORBsup	0.319	0.317	0.432	0.999	0.992
MFG	0.214	0.132	0.175	0.264	0.278
ORBmid	0.548	0.978	0.994	0.993	0.907
IFGoperc	0.184	0.505	0.291	0.926	0.604
IFGtriang	0.382	0.870	0.754	0.622	0.163
ORBinf	0.715	0.716	0.669	0.205	0.463
ROL	0.187	0.237	0.623	0.721	0.642
SMA	0.272	0.790	0.957	0.866	0.849
OLF	0.249	0.436	0.860	0.511	0.121
SFGmed	0.150	0.007*	0.018*	0.059	0.159
ORBsupmed	0.308	0.727	0.841	0.735	0.983
REC	0.267	0.271	0.133	0.058	0.206
INS	0.456	0.917	0.660	0.159	0.280
ACG	0.024*	0.020*	0.007*	0.078	0.400
DCG	0.571	0.496	0.962	0.747	0.645
PCG	0.358	0.124	0.345	0.156	0.972
HIP	0.984	0.961	0.582	0.825	0.533
PHG	0.962	0.196	0.344	0.503	0.417
AMYG	0.243	0.825	0.131	0.183	0.174
CAL	0.624	0.476	0.100	0.346	0.135
CUN	0.830	0.494	0.315	0.034*	0.027*
LING	0.615	0.989	0.540	0.707	0.376
SOG	0.344	0.325	0.635	0.771	0.775
MOG	0.704	0.887	0.879	0.938	0.924
IOG	0.298	0.357	0.440	0.505	0.366
FFG	0.008*	0.493	0.117	0.037*	0.003*
PoCG	0.226	0.733	0.620	0.470	0.837
SPG	0.862	0.182	0.044*	0.727	0.209
IPL	0.852	0.987	0.684	0.971	0.847
SMG	0.825	0.371	0.526	0.021*	0.472
ANG	0.205	0.769	0.893	0.847	0.989
PCUN	0.326	0.315	0.977	0.696	0.600
PCL	0.441	0.350	0.956	0.992	0.998
CAU	0.950	0.539	0.664	0.923	0.785
PUT	0.715	0.240	0.099	0.061	0.100
PAL	0.767	0.253	0.218	0.112	0.332
THA	0.291	0.161	0.321	0.140	0.951
HES	0.128	0.061	0.093	0.385	0.074
STG	0.001*	0.395	0.222	0.329	0.978
TPOsup	0.174	0.015*	0.076	0.943	0.782
MTG	0.755	0.248	0.595	0.802	0.865
TPOmid	0.220	0.297	0.209	0.308	0.095
ITG	0.294	0.949	0.222	0.710	0.344

Table A.13: Results from the normality test for the between-hemispheres comparison of the nodal global efficiency for the proportional thresholds of 20%, 25%, 30%, 35% and 40%. The values refer to the P value obtained from the application of Shapiro-Wilk's test. * indicates P value < 0.05 which represents statistical significance. Regions names are omitted but referred in Table 3.2 in Methods.

	Proportional threshold									
	20%		25%		30%		35%		40%	
Regions	**Test**	***p***	**Test**	***p***	**Test**	***p***	**Test**	***p***	**Test**	***p***
PreCG	*t*	0.992	*t*	0.903	*t*	0.749	*t*	0.579	*t*	0.614
SFGdor	*t*	0.109	*t*	0.109	*t*	0.109	*t*	0.061	*t*	0.084
ORBsup	*t*	0.772	*t*	0.762	*t*	0.746	*t*	0.419	*t*	0.446
MFG	*t*	0.297	*t*	0.184	*t*	0.180	*t*	0.203	*t*	0.244
ORBmid	*t*	0.521	*t*	0.550	*t*	0.688	*t*	0.688	*t*	0.688
IFGoperc	*t*	0.154	*t*	0.170	*t*	0.136	*t*	0.126	*t*	0.171
IFGtriang	*t*	0.596	*t*	0.490	*t*	0.192	*t*	0.202	*t*	0.265
ORBinf	*t*	0.578	*t*	0.807	*t*	0.854	*t*	0.783	*t*	0.871
ROL	*t*	0.423	*t*	0.411	*t*	0.489	*t*	0.345	*t*	0.600
SMA	*t*	0.516	*t*	0.616	*t*	0.668	*t*	0.948	*t*	0.994
OLF	*t*	0.813	*t*	0.469	*t*	0.813	*t*	0.688	*t*	0.551
SFGmed	*t*	0.156	*W*	0.016*	*W*	0.047*	*t*	0.100	*t*	0.121
ORBsupmed	*t*	0.664	*t*	0.762	*t*	0.938	*t*	0.787	*t*	0.688
REC	*t*	0.990	*t*	0.725	*t*	0.926	*t*	0.959	*t*	0.895
INS	*t*	0.219	*t*	0.208	*t*	0.290	*t*	0.270	*t*	0.422
ACG	*W*	1.000	*W*	0.537	*W*	0.569	*t*	0.630	*t*	0.497
DCG	*t*	0.208	*t*	0.194	*t*	0.375	*t*	0.813	*t*	0.688
PCG	*t*	0.813	*t*	0.813	*t*	0.341	*t*	0.231	*t*	0.138
HIP	*t*	0.109	*t*	0.102	*t*	0.078	*t*	0.156	*t*	0.109
PHG	*t*	0.219	*t*	0.211	*t*	0.303	*t*	0.219	*t*	0.331
AMYG	*t*	0.617	*t*	1.000	*t*	0.834	*t*	0.938	*t*	1.000
CAL	*t*	0.596	*t*	0.669	*t*	0.690	*t*	0.938	*t*	0.662
CUN	*t*	0.902	*t*	0.385	*t*	0.260	*W*	0.174	*W*	0.106
LING	*t*	0.212	*t*	0.177	*t*	0.157	*t*	0.168	*t*	0.393
SOG	*t*	0.938	*t*	0.813	*t*	0.813	*t*	0.578	*t*	0.688
MOG	*t*	0.938	*t*	0.813	*t*	1.000	*t*	0.807	*t*	0.583
IOG	*t*	0.446	*t*	0.688	*t*	0.501	*t*	0.514	*t*	0.717
FFG	*W*	0.938	*t*	0.706	*t*	0.784	*W*	0.617	*W*	0.375
PoCG	*t*	0.375	*t*	0.938	*t*	0.463	*t*	0.600	*t*	0.586
SPG	*t*	0.878	*t*	0.805	*W*	0.578	*t*	0.852	*t*	0.792
IPL	*t*	0.964	*t*	0.875	*t*	0.869	*t*	0.972	*t*	0.934
SMG	*t*	0.013*	*t*	0.075	*t*	0.235	*W*	0.335	*t*	0.483
ANG	*t*	0.079	*t*	0.093	*t*	0.190	*t*	0.202	*t*	0.235
PCUN	*t*	0.581	*t*	0.615	*t*	0.688	*t*	0.969	*t*	0.845
PCL	*t*	0.515	*t*	0.688	*t*	0.644	*t*	0.857	*t*	0.997
CAU	*t*	0.469	*t*	0.469	*t*	0.813	*t*	0.813	*t*	0.967
PUT	*t*	0.153	*t*	0.223	*t*	0.241	*t*	0.342	*t*	0.461
PAL	*t*	0.014*	*t*	0.097	*t*	0.066	*t*	0.078	*t*	0.163
THA	*t*	0.047*	*t*	0.047*	*t*	0.078	*t*	0.037*	*t*	0.052
HES	*t*	0.040*	*t*	0.078	*t*	0.219	*t*	0.219	*t*	0.297
STG	*W*	0.096	*t*	0.094	*t*	0.040*	*t*	0.069	*t*	0.066
TPOsup	*t*	1.000	*t*	0.733	*t*	0.688	*t*	0.813	*t*	0.938
MTG	*t*	0.395	*t*	0.633	*t*	0.719	*t*	0.578	*t*	0.700
TPOmid	*t*	0.297	*t*	0.297	*t*	0.219	*t*	0.297	*t*	0.219
ITG	*t*	0.956	*t*	0.805	*t*	0.796	*t*	0.561	*t*	0.764

Table A.14: Results from the comparison of nodal global efficiency between lesioned and non lesioned hemispheres, for each proportional threshold. from 20% to 40% with increments of 5%. *p* refers to the *P* value obtained from the application of two-sample paired *t* test and Wilcoxon matched pairs test, respectively represented as *t* and *W*. * indicates *P* value < 0.05 which represents statistical significance. Regions names are omitted but referred in Table 3.2 in Methods.

	Proportional threshold				
Regions	**20%**	**25%**	**30%**	**35%**	**40%**
PreCG	0.817	0.722	0.228	0.868	0.792
SFGdor	0.165	0.508	0.503	0.932	0.269
ORBsup	0.990	0.930	0.537	0.025*	0.023*
MFG	0.158	0.590	0.815	0.511	0.018*
ORBmid	0.441	0.496	0.051	0.716	0.335
IFGoperc	0.734	0.868	0.557	0.341	0.051
IFGtriang	0.432	0.165	0.474	0.662	0.930
ORBinf	0.852	0.045*	0.201	0.382	0.300
ROL	0.975	0.872	0.288	0.295	0.587
SMA	0.654	0.240	0.111	0.383	0.048*
OLF	0.284	0.372	0.001*	0.108	0.044*
SFGmed	0.910	0.536	0.029*	0.547	0.139
ORBsupmed	0.068	0.333	0.079	0.592	0.033*
REC	0.768	0.390	0.994	0.791	0.994
INS	0.139	0.713	0.101	0.574	0.593
ACG	0.810	0.301	0.570	0.906	0.891
DCG	0.866	0.288	0.005*	0.495	0.835
PCG	0.461	0.155	0.011*	1.898E-04*	0.781
HIP	0.811	0.885	0.035*	0.819	0.972
PHG	0.754	0.680	0.924	0.265	0.591
AMYG	0.119	0.377	0.281	0.480	0.053
CAL	0.498	0.528	0.284	0.438	0.704
CUN	0.222	0.166	0.333	0.572	0.809
LING	0.955	0.545	0.439	0.554	0.688
SOG	0.801	0.285	0.653	0.933	0.474
MOG	0.094	0.025*	0.053	0.028*	0.952
IOG	0.045*	0.987	0.714	0.539	0.720
FFG	0.495	0.313	0.368	0.257	0.580
PoCG	0.583	0.063	0.936	0.961	0.429
SPG	0.499	0.306	0.545	0.153	0.427
IPL	0.957	0.247	0.287	0.139	0.500
SMG	0.227	0.359	0.212	0.135	0.566
ANG	0.296	0.791	0.516	0.287	0.761
PCUN	0.445	0.295	0.182	0.882	0.276
PCL	0.566	0.576	0.142	0.808	0.586
CAU	0.446	0.556	0.004*	0.036*	0.103
PUT	0.496	0.590	0.417	0.178	0.459
PAL	0.070	0.265	0.222	0.062	0.629
THA	0.289	0.102	0.606	0.757	0.723
HES	0.163	0.183	0.028*	0.049*	0.152
STG	0.389	0.121	0.063	0.486	0.670
TPOsup	0.536	0.336	0.146	0.450	0.187
MTG	0.977	0.522	0.711	0.031*	0.069
TPOmid	0.572	0.696	0.683	0.707	0.057
ITG	0.539	0.883	0.149	0.923	0.574

Table A.15: Results from the normality test for the between-hemispheres comparison of the nodal clustering coefficient for the proportional thresholds of 20%, 25%, 30%, 35% and 40%. The values refer to the *P* value obtained from the application of Shapiro-Wilk's test. * indicates *P* value < 0.05 which represents statistical significance. Regions names are omitted but referred in Table 3.2 in Methods.

	Proportional threshold									
	20%		25%		30%		35%		40%	
Regions	**Test**	***p***	**Test**	***p***	**Test**	***p***	**Test**	***p***	**Test**	***p***
PreCG	*t*	0.403	*t*	0.493	*t*	0.973	*t*	0.574	*t*	0.878
SFGdor	*t*	0.813	*t*	0.813	*t*	0.375	*t*	0.576	*t*	0.467
ORBsup	*t*	0.495	*t*	0.688	*t*	0.469	*W*	0.938	*W*	0.578
MFG	*t*	0.829	*t*	0.578	*t*	0.375	*t*	0.623	*W*	0.287
ORBmid	*t*	0.156	*t*	0.040*	*t*	0.123	*t*	0.135	*t*	0.156
IFGoperc	*t*	0.109	*t*	0.193	*t*	0.167	*t*	0.243	*t*	0.273
IFGtriang	*t*	0.419	*t*	0.302	*t*	0.469	*t*	0.340	*t*	0.719
ORBinf	*t*	0.938	*W*	0.938	*t*	0.938	*t*	0.047*	*t*	0.516
ROL	*t*	0.192	*t*	0.785	*t*	0.731	*t*	0.829	*t*	0.459
SMA	*t*	0.156	*t*	0.058	*t*	0.568	*t*	0.449	*W*	0.196
OLF	*t*	0.675	*t*	0.529	*W*	0.529	*t*	0.469	*W*	0.219
SFGmed	*t*	0.436	*t*	0.614	*W*	1.000	*t*	0.093	*t*	0.194
ORBsupmed	*t*	0.164	*t*	0.557	*t*	0.987	*t*	0.414	*W*	0.178
REC	*t*	0.675	*t*	0.705	*t*	0.188	*t*	0.641	*t*	0.676
INS	*t*	1.000	*t*	0.784	*t*	0.938	*t*	0.567	*t*	0.840
ACG	*t*	0.129	*t*	0.219	*t*	0.290	*t*	0.803	*t*	0.720
DCG	*t*	0.391	*t*	0.904	*W*	0.169	*t*	0.553	*t*	0.744
PCG	*t*	0.142	*t*	0.834	*W*	0.469	*W*	0.813	*t*	0.863
HIP	*t*	0.012*	*t*	0.005*	*W*	0.063	*t*	0.215	*t*	0.344
PHG	*t*	0.938	*t*	1.000	*t*	0.678	*t*	0.688	*t*	0.743
AMYG	*t*	0.590	*t*	0.916	*t*	0.418	*t*	0.295	*t*	0.297
CAL	*t*	0.945	*t*	0.666	*t*	0.929	*t*	0.861	*t*	0.455
CUN	*t*	0.272	*t*	0.544	*t*	0.684	*t*	0.759	*t*	0.663
LING	*t*	0.166	*t*	0.158	*t*	0.146	*t*	0.126	*t*	0.302
SOG	*t*	0.469	*t*	0.979	*t*	0.578	*t*	0.668	*t*	0.569
MOG	*t*	0.194	*W*	0.219	*t*	0.219	*W*	0.263	*t*	0.228
IOG	*W*	0.127	*t*	0.482	*t*	0.155	*t*	0.208	*t*	0.297
FFG	*t*	0.376	*t*	0.589	*t*	0.298	*t*	0.133	*t*	0.083
PoCG	*t*	0.688	*t*	0.578	*t*	0.120	*t*	0.671	*t*	0.319
SPG	*t*	0.632	*t*	0.316	*t*	0.072	*t*	0.260	*t*	0.266
IPL	*t*	0.373	*t*	0.367	*t*	0.481	*t*	0.309	*t*	0.650
SMG	*t*	0.188	*t*	0.376	*t*	0.611	*t*	0.362	*t*	0.692
ANG	*t*	0.026*	*t*	0.250	*t*	0.190	*t*	0.005*	*t*	0.156
PCUN	*t*	0.478	*t*	0.659	*t*	0.868	*t*	0.736	*t*	0.837
PCL	*t*	0.280	*t*	0.469	*t*	0.938	*t*	0.128	*t*	0.685
CAU	*t*	0.866	*t*	0.469	*W*	0.016*	*W*	0.375	*t*	0.156
PUT	*t*	0.445	*t*	0.219	*t*	0.297	*t*	0.822	*t*	1.000
PAL	*t*	0.789	*t*	0.058	*t*	0.150	*t*	0.141	*t*	0.966
THA	*t*	0.036*	*t*	0.016*	*t*	0.156	*t*	0.297	*t*	0.583
HES	*t*	0.590	*t*	0.688	*W*	0.469	*W*	0.938	*t*	0.938
STG	*t*	0.522	*t*	0.630	*t*	0.721	*t*	0.941	*t*	0.521
TPOsup	*t*	0.095	*t*	0.156	*t*	0.979	*t*	0.131	*t*	0.300
MTG	*t*	0.297	*t*	0.242	*t*	0.148	*W*	0.110	*t*	0.109
TPOmid	*t*	0.684	*t*	0.578	*t*	0.469	*t*	0.297	*t*	0.109
ITG	*t*	0.333	*t*	0.386	*t*	0.289	*t*	0.375	*t*	0.297

Table A.16: Results from the comparison of nodal clustering coefficient between lesioned and non lesioned hemispheres, for each proportional threshold, from 20% to 40% with increments of 5%. *p* refers to the *P* value obtained from the application of two-sample paired *t* test and Wilcoxon matched pairs test, respectively represented as *t* and *W*. * indicates *P* value < 0.05 which represents statistical significance. Regions names are omitted but referred in Table 3.2 in Methods.

Appendix B

Statistical analysis - R code

```
install.packages('dplyr');
install.packages('ggpubr');
library('dplyr');
library('ggpubr');

install.packages("MASS")
library("MASS")

#GLOBAL DATA
data=read.delim(file.choose(),header=FALSE, sep="");
data
column=ncol(data)
column
lines=nrow(data);
lines;
data_densities=read.delim(file.choose(),header=FALSE, sep="");
data_densities;
column_densities=length(data_densities);
column_densities;
lines_densities=nrow(data_densities);
lines_densities;

#mean, standard deviation and median

mean_sd_median_global=matrix(1,nrow=6,ncol=column-1)
rownames(mean_sd_median_global)=c('mean_L','sd_L','median_L','mean_NL','
   sd_NL','median_NL');
colnames(mean_sd_median_global)=c('20','25','30','35','40');

for (i in 2:column-1){
        mean_sd_median_global[1,i]=mean(data[(1:7),i])
        mean_sd_median_global[2,i]=sd(data[(1:7),i])
        mean_sd_median_global[3,i]=median(data[(1:7),i])
        mean_sd_median_global[4,i]=mean(data[(8:14),i])
        mean_sd_median_global[5,i]=sd(data[(8:14),i])
        mean_sd_median_global[6,i]=median(data[(8:14),i])
}
```

```
mean_sd_median_global;
write.matrix(mean_sd_median_global,file='mean_sd_median_global',sep=' ')
    ;

#plot of mean global values

jpeg('plot_mean_SW.jpg')
x=c(20,25,30,35,40);

plot(x,mean_sd_median_global[1,],ylim=c(0.95,1.7),pch=19,xlab='
    PROPORTIONAL THRESHOLD',ylab='SMALL-WORLDNESS',col="green");
arrows(x, mean_sd_median_global[1,]-mean_sd_median_global[2,], x, mean_
    sd_median_global[1,]+mean_sd_median_global[2,],length=0.13,angle=90,
    code=3, lwd=1.5, col="green")
lines(x,mean_sd_median_global[1,],lwd=2,col="green")
par(new=TRUE);
par(ann=FALSE);
plot(x,mean_sd_median_global[4,],ylim=c(0.95,1.7),pch=19,axes=FALSE,col=
    "red");
arrows(x, mean_sd_median_global[4,]-mean_sd_median_global[5,], x, mean_
    sd_median_global[4,]+mean_sd_median_global[5,],length=0.13,angle=90,
    code=3, lwd=1.5, col="red")
lines(x,mean_sd_median_global[4,],lwd=2,col="red");

legend('topright',legend=c('Lesioned','Non lesioned'),lty=c(1,1),col=c('
    green','red'))
dev.off()

#NODAL DATA
data_nodal=read.delim(file.choose(),header=FALSE, sep="");
data_nodal;
column_nodal=ncol(data_nodal)
column_nodal;
lines_nodal=nrow(data_nodal);
lines_nodal;
sequence_nodal=seq(1,lines_nodal,14);
sequence_nodal;
regions=seq(1,lines_nodal/14);
regions;
data_densities_nodal=read.delim(file.choose(),header=FALSE, sep="");
data_densities_nodal;
column_densities_nodal=ncol(data_densities_nodal)
column_densities_nodal;
lines_densities_nodal=nrow(data_densities_nodal);
lines_densities_nodal;
sequence_densities_nodal=seq(1,lines_densities_nodal,35);
sequence_densities_nodal;

#mean, standard deviation and median

mean_sd_median_nodal=matrix(1,nrow=lines_nodal/14,ncol=30)
```

```
mean_sd_median_nodal;
colnames(mean_sd_median_nodal)=c('mean_20L','sd_20L','median_20L','mean_
   20NL','sd_20NL','median_20NL','mean_25L','sd_25L','median_25L','mean_
   25NL','sd_25NL','median_25NL','mean_30L','sd_30L','median_30L','mean_
   30NL','sd_30NL','median_30NL','mean_35L','sd_35L','median_35L','mean_
   35NL','sd_35NL','median_35NL','mean_40L','sd_40L','median_40L','mean_
   40NL','sd_40NL','median_40NL');

sequence_matrix=seq(1,30,6);
sequence_matrix;

for (j in 1:column_nodal){
        for (i in regions){
                position=sequence_nodal[i]
                p=sequence_matrix[j]
                mean_sd_median_nodal[i,p]=mean(data_nodal[position:(
                   position+6),j]);
                mean_sd_median_nodal[i,(p+1)]=sd(data_nodal[position:(
                   position+6),j]);
                mean_sd_median_nodal[i,(p+2)]=median(data_nodal[position
                   :(position+6),j]);
                mean_sd_median_nodal[i,(p+3)]=mean(data_nodal[(position
                   +7):(position+13),j]);
                mean_sd_median_nodal[i,(p+4)]=sd(data_nodal[(position+7)
                   :(position+13),j]);
                mean_sd_median_nodal[i,(p+5)]=median(data_nodal[(
                   position+7):(position+13),j]);
                }
}

mean_sd_median_nodal;
write.matrix(mean_sd_median_nodal,file='mean_sd_median_nodal',sep='␣');

#BETWEEN-THRESHOLD COMPARISON
#between-threshold comparison, for lesioned and non lesioned hemispheres

#GLOBAL DATA
##normality testing

sequence=seq(1,lines_densities,7);
sequence=sequence[-5];
sequence;

matrix_pv_bt_global=matrix(1,nrow=column_densities-1,ncol=4);
matrix_pv_bt_global;

for (j in 1:(column_densities-1)){
        for (i in sequence){
                norm=with(data_densities,data_densities[i:(i+6),j]-data_
                   densities[(i+7):(i+13),j]);
                test_norm=shapiro.test(norm);
```

```
                index_matrix=which(sequence==i);
                matrix_pv_bt[j,index_matrix]=print(test_norm$p.value);

        }
}
matrix_pv_bt_global;
write.matrix(matrix_pv_bt_global,file='matrix_pv_global_BT.txt',sep='␣')
    ;

result=matrix(1,nrow=2,ncol=4);
result;

#for the between-threshold comparison, the paired t test is applied if
    the corresponding P value obtained from the normality testing is
    higher than 0.05 (significance level of 5%). Otherwise, the Wilcoxon
    matched pairs test is applied.

#comparison between densities of 20% and 25%
##Lesioned hemisphere
if(matrix_pv_bt_global[1,1]>0.05){
        test_lesioned=t.test(data$V1[(1:7)],data$V2[(1:7)],paired=TRUE);
        result[1,1]=test_lesioned$p.value;
}
if(matrix_pv_bt_global[1,1]<=0.05){
        test_lesioned=wilcox.test(data$V1[(1:7)],data$V2[(1:7)],paired=
            TRUE);
        result[1,1]=test_lesioned$p.value;
}
##Non lesioned hemisphere
if(matrix_pv_bt_global[2,1]>0.05){
        test_NONlesioned=t.test(data$V1[(8:14)],data$V2[(8:14)],paired=
            TRUE);
        result[2,1]=test_NONlesioned$p.value;
}
if(matrix_pv_bt_global[2,1]<=0.05){
        test_NONlesioned=wilcox.test(data$V1[(8:14)],data$V2[(8:14)],
            paired=TRUE);
        result[2,1]=test_NONlesioned$p.value;
}

#comparison between densities of 25% and 30%
##Lesioned hemisphere
if(matrix_pv_bt_global[1,2]>0.05){
        test_lesioned=t.test(data$V2[(1:7)],data$V3[(1:7)],paired=TRUE);
        result[1,2]=test_lesioned$p.value;
}
if(matrix_pv_bt_global[1,2]<=0.05){
        test_lesioned=wilcox.test(data$V2[(1:7)],data$V3[(1:7)],paired=
            TRUE);
        result[1,2]=test_lesioned$p.value;
}
```

```
##Non lesioned hemisphere
if(matrix_pv_bt_global[2,2]>0.05){
        test_NONlesioned=t.test(data$V2[(8:14)],data$V3[(8:14)],paired=
           TRUE);
        result[2,2]=test_NONlesioned$p.value;
}
if(matrix_pv_bt_global[2,2]<=0.05){
        test_NONlesioned=wilcox.test(data$V2[(8:14)],data$V3[(8:14)],
           paired=TRUE);
        result[2,2]=test_NONlesioned$p.value;
}

#comparison between densities of 30% and 35%
##Lesioned hemisphere
if(matrix_pv_bt_global[1,3]>0.05){
        test_lesioned=t.test(data$V3[(1:7)],data$V4[(1:7)],paired=TRUE);
        result[1,3]=test_lesioned$p.value;
}
if(matrix_pv_bt_global[1,3]<=0.05){
        test_lesioned=wilcox.test(data$V3[(1:7)],data$V4[(1:7)],paired=
           TRUE);
        result[1,3]=test_lesioned$p.value;
}
##Non lesioned hemisphere
if(matrix_pv_bt_global[2,3]>0.05){
        test_NONlesioned=t.test(data$V3[(8:14)],data$V4[(8:14)],paired=
           TRUE);
        result[2,3]=test_NONlesioned$p.value;
}
if(matrix_pv_bt_global[2,3]<=0.05){
        test_NONlesioned=wilcox.test(data$V3[(8:14)],data$V4[(8:14)],
           paired=TRUE);
        result[2,3]=test_NONlesioned$p.value;
}

#comparison between densities of 35% and 40%
##Lesioned hemisphere
if(matrix_pv_bt_global[1,4]>0.05){
        test_lesioned=t.test(data$V4[(1:7)],data$V5[(1:7)],paired=TRUE);
        result[1,4]=test_lesioned$p.value;
}
if(matrix_pv_bt_global[1,4]<=0.05){
        test_lesioned=wilcox.test(data$V4[(1:7)],data$V5[(1:7)],paired=
           TRUE);
        result[1,4]=test_lesioned$p.value;
}
##Non lesioned hemisphere
if(matrix_pv_bt_global[2,4]>0.05){
        test_NONlesioned=t.test(data$V4[(8:14)],data$V5[(8:14)],paired=
           TRUE);
        result[2,4]=test_NONlesioned$p.value;
```

```
}
if(matrix_pv_bt_global[2,4]<=0.05){
        test_NONlesioned=wilcox.test(data$V4[(8:14)],data$V5[(8:14)],
           paired=TRUE);
        result[2,4]=test_NONlesioned$p.value;
}
result;
write.matrix(result,file='global_BTcomparison.txt',sep='␣');

#NODAL DATA
##normality testing

###Lesioned hemisphere
matrix_pv_bt_nodal_lesioned=matrix(1,nrow=lines_nodal/14,ncol=4);
matrix_pv_bt_nodal_lesioned;

for (k in sequence_densities_nodal){
        for (i in seq(k,(k+27),7)){
                norm=with(data_densities_nodal,data_densities_nodal[i:(i
                   +6),1]-data_densities_nodal[(i+7):(i+13),1]);
                test_norm=shapiro.test(norm);
                index_matrix=which(seq(k,(k+27),7)==i);
                index_regions=which(sequence_densities_nodal==k);
                matrix_pv_bt_nodal_lesioned[index_regions,index_matrix]=
                   test_norm$p.value;
        }
}

#Non lesioned hemisphere
matrix_pv_bt_nodal_NONlesioned=matrix(1,nrow=lines_nodal/14,ncol=4);
matrix_pv_bt_nodal_NONlesioned;

for (k in sequence_densities_nodal){
        for (i in seq(k,(k+27),7)){
                norm=with(data_densities_nodal,data_densities_nodal[i:(i
                   +6),2]-data_densities_nodal[(i+7):(i+13),2]);
                test_norm=shapiro.test(norm);
                index_matrix=which(seq(k,(k+27),7)==i);
                index_regions=which(sequence_densities_nodal==k);
                matrix_pv_bt_nodal_NONlesioned[index_regions,index_
                   matrix]=test_norm$p.value;
        }
}
matrix_pv_bt_nodal_lesioned;
matrix_pv_bt_nodal_NONlesioned;
write.matrix(matrix_pv_bt_nodal_lesioned,file='matrix_pv_nodal_BT_
   lesioned.txt',sep='␣');
write.matrix(matrix_pv_bt_nodal_NONlesioned,file='matrix_pv_nodal_BT_
   NONlesioned.txt',sep='␣');
```

```
#for the between-threshold comparison, the paired t test is applied if
   the corresponding P value obtained from the normality testing is
   higher than 0.05 (significance level of 5%). Otherwise, the Wilcoxon
   matched pairs test is applied.

#Lesioned hemisphere

result_nodal_lesioned=matrix(1,nrow=lines_nodal/14,ncol=4);
result_nodal_lesioned;

#comparison between densities of 20% and 25%
for (i in sequence_nodal){
        index=which(sequence_nodal==i);
        if (matrix_pv_bt_nodal_lesioned[index,1]>0.05){
                test_lesioned=t.test(data_nodal$V1[i:(i+6)],data_nodal$
                   V2[i:(i+6)],paired=TRUE);
                result_nodal[index,1]=test_lesioned$p.value;
        }
        if (matrix_pv_bt_nodal_lesioned[index,1]<=0.05){
                test_lesioned=wilcox.test(data_nodal$V1[i:(i+6)],data_
                   nodal$V2[i:(i+6)],paired=TRUE);
                result_nodal[index,1]=test_lesioned$p.value;
        }

}

#comparison between densities of 25% and 30%
for (i in sequence_nodal){
        index=which(sequence_nodal==i);
        if (matrix_pv_bt_nodal_lesioned[index,2]>0.05){
                test_lesioned=t.test(data_nodal$V2[i:(i+6)],data_nodal$
                   V3[i:(i+6)],paired=TRUE);
                result_nodal[index,2]=test_lesioned$p.value;
        }
        if (matrix_pv_bt_nodal_lesioned[index,2]<=0.05){
                test_lesioned=wilcox.test(data_nodal$V2[i:(i+6)],data_
                   nodal$V3[i:(i+6)],paired=TRUE);
                result_nodal[index,2]=test_lesioned$p.value;
        }

}

#comparison between densities of 30% and 35%
for (i in sequence_nodal){
        index=which(sequence_nodal==i);
        if (matrix_pv_bt_nodal_lesioned[index,3]>0.05){
                test_lesioned=t.test(data_nodal$V3[i:(i+6)],data_nodal$
                   V4[i:(i+6)],paired=TRUE);
                result_nodal[index,3]=test_lesioned$p.value;
        }
        if (matrix_pv_bt_nodal_lesioned[index,3]<=0.05){
```

```
                test_lesioned=wilcox.test(data_nodal$V3[i:(i+6)],data_
                    nodal$V4[i:(i+6)],paired=TRUE);
                result_nodal[index,3]=test_lesioned$p.value;
        }

}

#comparison between densities of 35% and 40%
for (i in sequence_nodal){
        index=which(sequence_nodal==i);
        if (matrix_pv_bt_nodal_lesioned[index,4]>0.05){
                test_lesioned=t.test(data_nodal$V4[i:(i+6)],data_nodal$
                    V5[i:(i+6)],paired=TRUE);
                result_nodal[index,3]=test_lesioned$p.value;
        }
        if (matrix_pv_bt_nodal_lesioned[index,4]<=0.05){
                test_lesioned=wilcox.test(data_nodal$V4[i:(i+6)],data_
                    nodal$V5[i:(i+6)],paired=TRUE);
                result_nodal[index,3]=test_lesioned$p.value;
        }

}

#Non lesioned hemisphere

result_nodal_NONlesioned=matrix(1,nrow=lines_nodal/14,ncol=4);
result_nodal_NONlesioned;

#comparison between densities of 20% and 25%
for (i in sequence_nodal){
        index=which(sequence_nodal==i);
        if (matrix_pv_bt_nodal_NONlesioned[index,1]>0.05){
                test_NONlesioned=t.test(data_nodal$V1[(i+7):(i+13)],data
                    _nodal$V2[(i+7):(i+13)],paired=TRUE);
                result_nodal[index,1]=test_NONlesioned$p.value;
        }
        if (matrix_pv_bt_nodal_NONlesioned[index,1]<=0.05){
                test_NONlesioned=wilcox.test(data_nodal$V1[(i+7):(i+13)
                    ],data_nodal$V2[(i+7):(i+13)],paired=TRUE);
                result_nodal[index,1]=test_NONlesioned$p.value;
        }

}

#comparison between densities of 25% and 30%
for (i in sequence_nodal){
        index=which(sequence_nodal==i);
        if (matrix_pv_bt_nodal_NONlesioned[index,2]>0.05){
                test_NONlesioned=t.test(data_nodal$V2[(i+7):(i+13)],data
                    _nodal$V3[(i+7):(i+13)],paired=TRUE);
                result_nodal[index,2]=test_NONlesioned$p.value;
```

```
        }
        if (matrix_pv_bt_nodal_NONlesioned[index,2]<=0.05){
                test_NONlesioned=wilcox.test(data_nodal$V2[(i+7):(i+13)
                   ],data_nodal$V3[(i+7):(i+13)],paired=TRUE);
                result_nodal[index,2]=test_NONlesioned$p.value;
        }

}

#comparison between densities of 30% and 35%
for (i in sequence_nodal){
        index=which(sequence_nodal==i);
        if (matrix_pv_bt_nodal_NONlesioned[index,3]>0.05){
                test_NONlesioned=t.test(data_nodal$V3[(i+7):(i+13)],data
                   _nodal$V4[(i+7):(i+13)],paired=TRUE);
                result_nodal[index,3]=test_NONlesioned$p.value;
        }
        if (matrix_pv_bt_nodal_NONlesioned[index,3]<=0.05){
                test_NONlesioned=wilcox.test(data_nodal$V3[(i+7):(i+13)
                   ],data_nodal$V4[(i+7):(i+13)],paired=TRUE);
                result_nodal[index,3]=test_NONlesioned$p.value;
        }

}

#comparison between densities of 35% and 40%
for (i in sequence_nodal){
        index=which(sequence_nodal==i);
        if (matrix_pv_bt_nodal_NONlesioned[index,4]>0.05){
                test_NONlesioned=t.test(data_nodal$V4[(i+7):(i+13)],data
                   _nodal$V5[(i+7):(i+13)],paired=TRUE);
                result_nodal[index,3]=test_NONlesioned$p.value;
        }
        if (matrix_pv_bt_nodal_NONlesioned[index,4]<=0.05){
                test_NONlesioned=wilcox.test(data_nodal$V4[(i+7):(i+13)
                   ],data_nodal$V5[(i+7):(i+13)],paired=TRUE);
                result_nodal[index,3]=test_NONlesioned$p.value;
        }

}

#BETWEEN-HEMISPHERES COMPARISON
#between-hemispheres comparison, for each proportional threshold

#GLOBAL DATA
##normality testing

matrix_pv_bh_global=matrix(1,nrow=1,ncol=column-1);
matrix_pv_bh_global;

for (i in 1:(column-1)){
```

```
                norm=with(data,data[1:7,i]-data[8:14,i]);
                test_norm=shapiro.test(norm);
                matrix_pv_bh_global[1,i]=test_norm$p.value;

}
matrix_pv_bh_global
write.matrix(matrix_pv_bh,_global,file='matrix_pv_global_BH.txt',sep='␣'
    );

#for the between-threshold comparison, the paired t test is applied if
    the corresponding P value obtained from the normality testing is
    higher than 0.05 (significance level of 5%). Otherwise, the Wilcoxon
    matched pairs test is applied.

for (i in 1:(column-1)){
        if(matrix_pv_bh_global[1,i]>0.05){
                test=t.test(data[(1:7),i],data[(8:14),i],paired=TRUE);
                result=test$p.value;
        }

        if(matrix_pv_bh_global[1,i]<=0.05){
                test=wilcox.test(data[(1:7),i],data[(8:14),i], paired=
                    TRUE);
                result=test$p.value;
        }
}

#NODAL DATA
##normality testing

matrix_pv_bh_nodal=matrix(1,nrow=lines_nodal/14,ncol=5);
matrix_pv_bh_nodal;

for (i in 1:column_nodal){
        for (k in sequence_nodal){
                norm=with(data_nodal,data_nodal[k:(k+6),i]-data_nodal[(k
                    +7):(k+13),i]);
                test_norm=shapiro.test(norm);
                index_regions=which(sequence_nodal==k);
                matrix_pv_bh_nodal[index_regions,i]=test_norm$p.value;

        }
}

matrix_pv_bh_nodal;
write.matrix(matrix_pv_bh_nodal,file='matrix_pv_nodal_BH.txt',sep='␣');

#for the between-hemispheres comparison, the paired t test is applied if
     the corresponding P value obtained from the normality testing is
    higher than 0.05 (significance level of 5%). Otherwise, the Wilcoxon
    matched pairs test is applied.
```

```
result_nodal=matrix(1,length(matrix_pv_bh_nodal[,1]),5);
colnames(result_nodal)=c('20','25','30','35','40');
result_nodal;

#comparison between hemispheres at proportional threshold 20%
for (k in regions){
        position=sequence_nodal[k]
        if(matrix_pv_bh_nodal[k,1]>0.05){
                test=t.test(data_nodal[position:(position+6),1],data_
                    nodal[(position+7):(position+13),1],paired=TRUE);
                result_nodal[k,1]=test$p.value;
        }
        if(matrix_pv_bh_nodal[k,1]<=0.05){
                test=wilcox.test(data_nodal[position:(position+6),1],
                    data_nodal[(position+7):(position+13),1], paired=TRUE
                    );
                result_nodal[k,1]=test$p.value;
        }
}
#comparison between hemispheres at proportional threshold 25%
for (k in regions){
        position=sequence_nodal[k]
        if(matrix_pv_bh_nodal[k,2]>0.05){
                test=t.test(data_nodal[position:(position+6),2],data_
                    nodal[(position+7):(position+13),2],paired=TRUE);
                result_nodal[k,2]=test$p.value;
        }
        if(matrix_pv_bh_nodal[k,2]<=0.05){
                test=wilcox.test(data_nodal[position:(position+6),2],
                    data_nodal[(position+7):(position+13),2], paired=TRUE
                    );
                result_nodal[k,2]=test$p.value;
        }
}

#comparison between hemispheres at proportional threshold 30%
for (k in regions){
        position=sequence_nodal[k]
        if(matrix_pv_bh_nodal[k,3]>0.05){
                test=t.test(data_nodal[position:(position+6),3],data_
                    nodal[(position+7):(position+13),3],paired=TRUE);
                result_nodal[k,3]=test$p.value;
        }
        if(matrix_pv_bh_nodal[k,3]<=0.05){
                test=wilcox.test(data_nodal[position:(position+6),3],
                    data_nodal[(position+7):(position+13),3], paired=TRUE
                    );
                result_nodal[k,3]=test$p.value;
        }
}
```

```
#comparison between hemispheres at proportional threshold 35%
for (k in regions){
        position=sequence_nodal[k]
        if(matrix_pv_bh_nodal[k,4]>0.05){
                test=t.test(data_nodal[position:(position+6),4],data_
                   nodal[(position+7):(position+13),4],paired=TRUE);
                result_nodal[k,4]=test$p.value;
        }
        if(matrix_pv_bh_nodal[k,4]<=0.05){
                test=wilcox.test(data_nodal[position:(position+6),4],
                   data_nodal[(position+7):(position+13),4], paired=TRUE
                   );
                result_nodal[k,4]=test$p.value;
        }
}

#comparison between hemispheres at proportional threshold 40%
for (k in regions){
        position=sequence_nodal[k]
        if(matrix_pv_bh_nodal[k,5]>0.05){
                test=t.test(data_nodal[position:(position+6),5],data_
                   nodal[(position+7):(position+13),5],paired=TRUE);
                result_nodal[k,5]=test$p.value;
        }
        if(matrix_pv_bh_nodal[k,5]<=0.05){
                test=wilcox.test(data_nodal[position:(position+6),5],
                   data_nodal[(position+7):(position+13),5], paired=TRUE
                   );
                result_nodal[k,5]=test$p.value;
        }
}

result_nodal
write.matrix(result_nodal,file='result_nodal_BH.txt',sep='␣');
```